Observation of the fully hadronic decay of $t\bar{t}$ pairs in $p\bar{p}$ collisions at $\sqrt{s} = 1.8$ TeV.

by

Wasiq M. Bokhari

B.S. Mathematics, B.S. Physics
Massachusetts Institute of Technology

Submitted to the Department of Physics
in partial fulfillment of the requirements for the degree of

Doctor of Philosophy

at the

MASSACHUSETTS INSTITUTE OF TECHNOLOGY

June 1997

Author .....
Department of Physics
April 30, 1997

Certified by .....
Paraskevas A. Sphicas
Professor
Thesis Supervisor

Accepted by .....
Prof. George F. Koster
Chairman of the Physics Department Committee on Graduate Students

Observation of the fully hadronic decay of $t\bar{t}$ pairs in $p\bar{p}$ collisions at $\sqrt{s} = 1.8$ TeV.

by

Wasiq M. Bokhari

Submitted to the Department of Physics
on April 30, 1997, in partial fulfillment of the
requirements for the degree of
Doctor of Philosophy

Abstract

The fully hadronic decay of $t\bar{t}$ pairs has been observed in $p\bar{p}$ collisions at the Collider Detector at Fermilab. Using 109.4 ± 7.1 pb^{-1} of data collected at $\sqrt{s} = 1.8$ TeV, 37.5 ± 16.9 signal events are observed over a background of 119.5 ± 17.9. The $t\bar{t}$ production cross-section is measured to be 11.5 ± 5.0 (statistical) $^{+5.9}_{-5.0}$ (systematic) pb for a top quark of mass $M = 175$ GeV/c^2.

Thesis Supervisor: Paraskevas A. Sphicas
Title: Professor

Acknowledgements

Now that I have to acknowledge the influence of different people on me, I realize that this is not an easy task. I will undoubtedly neglect to thank many people who I know have influenced me positively in the past. Nevertheless, here it goes, in words.

I have been associated with the MIT group for a long time, and in a way, the members of the group mean more to me than just "people that I work with". Over the years, I have been molded into an individual embodying many of our shared principles and I find myself undoubtedly richer after this experience. I am indebted to my advisor Paris Sphicas for giving me ample opportunity and support to work in High Energy Physics. I hope, as I move on past my student days, I can maintain the high standards of integrity and resolution reflected in him. I owe a lot to Larry Rosenson, for his constant guidance and interest in my work over the years. I have learnt, and continue to learn, from his deep understanding of physics and life in general. My deepest thanks also to Jerry Friedman, for his interest in my well-being over the years and for sharing his uniquely thorough appreciation of a wide range of issues with me. I would also like to thank Gerry Bauer, Sham Sumorok, Steve Pavlon and Steve Tether for their delightful company over the years and for taking a keen interest in my well-being.

My thanks to people with whom I have worked closely: Andrea Castro, Patrizia Azzi, Rob Roser and Liz Buckley. And to people who took interest in my work, in particular, Bill Carithers, Nigel Lockyer and Tony Liss. And also to all the people I worked with during the data-taking shifts at CDF, and during the many hours spent working on Gas-gain or the hadronic calorimeters.

I have been associated with some wonderful people during my graduate school years. They include my former house-mates at the "MIT house", Tushar, Troy and Petar, with whom I have shared a lot. I have also had a rewarding friendship with Owen, Farrukh and Rick. I would like to thank some of my old friends, Baber, Kamal and Sarmad, for their priceless company over the years. My thanks also to Megumi, for friendship, wisdom and a fantastic taste in literature. And to Ken, Brendan, Benn, Dejan, Paul, Mark, Dave and others whom I am grateful to but have not mentioned by name.

I would like to thank Carol Picciolo for taking care of things at Fermilab, and Peggy Berkowitz for taking care of things at MIT.

I would like to thank my aunt, Dr. Tanveer, for often worrying about me. And finally, most importantly, I would like to thank my family -my parents, my sisters and my brothers, who have patiently stood by every decision of mine, and have been a constant source of support and pride for me. This work would not have been possible without them. This thesis is dedicated to both of my parents.

هان مشو نومید چون غافل نه از سر غیب
باشد آندر پرده بازیهای پنهان غم مخور
ـ حافظ شیرازی

Contents

List of Figures

List of Tables

Chapter 1

Outline

The top quark is a fundamental particle required by the Standard Model (SM) of elementary particles and their interactions [1, 2]. It was discovered by the CDF and DØ collaborations in 1995 [3, 4] using data collected at the Fermilab Tevatron in $p\bar{p}$ collisions at a center of mass energy of 1.8 TeV. Within the context of SM, the top quark decays almost exclusively into a b quark and a W boson. The W boson can decay into a charged lepton and a neutrino, or it can decay into two quarks. At CDF and DØ, top quarks are produced mostly in pairs. The top quark was discovered in a final state where at least one of the W bosons produced in the decay of the $t\bar{t}$ pair decays into a charged lepton and a neutrino. This thesis reports the first observation of $t\bar{t}$ production in the decay channel where both W bosons decay into quarks.

1.1 Overview of the Standard Model

The basic questions of particle physics are: What are the fundamental building blocks of the universe and how do they interact with each other. The Standard Model is the most successful attempt to date to answer these questions.

There are two corner-stones of modern physics: relativity and quantum mechanics [5]. Relativity forbids the transmission of information at a velocity greater than the velocity of light. This implies that particles cannot instantaneously influence each other, and are sources of fields that mediate energy (and other physical quantities) to

other particles. Quantum mechanics requires that energy (and other physical quantities) occur in discrete packets, which themselves become identified with particles. A relativistic quantum mechanical treatment of fields leads to a quantum field theory. The Standard Model is one such theory which views the universe as being composed of two categories of particles based on their spin. Particles in the first category are called *fermions* and have spins $\frac{1}{2}, \frac{3}{2}, \frac{5}{2}, \cdots$ etc. *Quarks* and *leptons* are fermions and are the building blocks of matter. Particles in the second category are called *bosons* and have spins $0, 1, 2, \cdots$ etc. *Photons*, *gluons* and *massive vector bosons* are bosons and are the carriers of forces between quarks and leptons.

We know of four fundamental forces in the universe. They are the gravitational, electromagnetic, weak and strong forces. The gauge theory of electromagnetic interactions, Quantum Electrodynamics (QED) [5], was formulated in the 1940's, and has enjoyed a spectacular experimental confirmation. In 1970's the gauge theories of electromagnetic and weak interactions were unified into the Electroweak Theory (EWK) [1]. The gauge theory of strong interactions is Quantum Chromodynamics (QCD) [2]. Gravitation is described by the classical General theory of relativity [7]. Gauge theories are a special class of quantum field theories where the existence of interactions between particles is necessitated by the presence of certain underlying symmetries or invariance principles of nature. Specifically, the Lagrangian of a gauge theory is invariant under certain local transformations. Forces in gauge theories not only respect certain underlying symmetries but are also proportional to a coupling constant or a "charge" of some kind. A familiar example is the electromagnetic force where the fine structure constant $\alpha(\equiv \frac{e^2}{4\pi} \approx \frac{1}{137})$ not only characterizes the strength of the interaction, but also the amount of charge carried by the particles. The "charge" in the electromagnetic interactions is the familiar Coulomb charge while the "charge" in strong interactions is called *color*. The underlying symmetries of the theories are handled by the mathematical tools of group theory. The groups under which the Lagrangian is invariant are referred to as the gauge groups of the theory.

The existence of quarks was inferred from the underlying symmetries in the rich spectrum of observed particles and proven dramatically by deep inelastic scattering of

electrons and protons [9]. They carry the color charge which is traditionally assigned values red, green or blue. All observed hadrons (i.e. particles that experience the strong interactions) are colorless, i.e they are either color-anticolor states of two quarks (mesons) or have three quarks, one of each color (baryons). Six types of quarks are known. They are *up* (u), *down* (d), *charm* (c), *strange* (s), *top* (t) and *bottom* (b). For example, the proton is a (uud) state, while a neutron is a (udd).

Leptons are fermions that do not carry the color charge. Like the quarks, there are six leptons: The leptons are the electron (e), the muon (μ), the tau (τ) and their three corresponding neutrinos (ν_e,ν_μ and ν_τ). Quarks and leptons are grouped into families or doublets by the Electroweak theory according to a quantum number called the "weak isospin". The quark doublets are:

$$\begin{pmatrix} u \\ d \end{pmatrix} \begin{pmatrix} c \\ s \end{pmatrix} \begin{pmatrix} t \\ b \end{pmatrix}$$

The top row has a weak isospin (charge) $+\frac{1}{2}$ $(+\frac{2}{3}e)$ and the bottom row $-\frac{1}{2}$ $(-\frac{1}{3}e)$ where e is the magnitude of the electron charge. The lepton doublets are:

$$\begin{pmatrix} \nu_e \\ e \end{pmatrix} \begin{pmatrix} \nu_\mu \\ \mu \end{pmatrix} \begin{pmatrix} \nu_\tau \\ \tau \end{pmatrix}$$

The neutrinos have no charge while the e, μ and the τ have a charge of $-e$. Photons and massive vector bosons (W,Z) are the carriers of the electroweak force. Gluons are the carriers of the strong force.

Once the Lagrangian of a theory is specified, it can be used to calculate all the physical implications of the theory like kinematic spectra, cross-sections and reaction rates etc. If $V(x)$ is the interaction term of the Lagrangian, the transition amplitude, A_{fi}, from an initial state ϕ_i to a final state ϕ_f is given by:

$$A_{fi} \;=\; -i \int d^4x \phi_f^*(x) V(x) \phi_i(x)$$

Particle interactions are represented pictorially by Feynman diagrams as shown in figure 1-1. Feynman diagrams represent particular terms in the perturbation series expansion of the transition amplitude in terms of the interaction coupling constant.

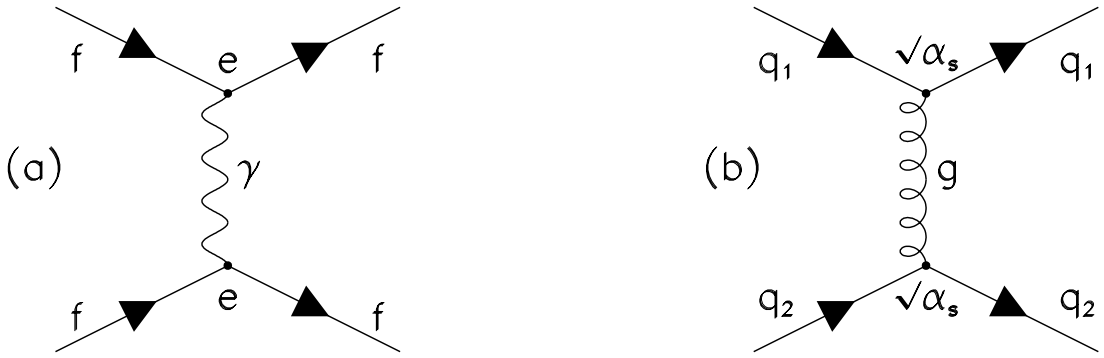

Figure 1-1: *Two examples of Feynman diagrams. Electromagnetic scattering of electrons through the exchange of a virtual photon (a) and the strong scattering of two quarks through the exchange of a gluon (b).*

In accordance with Fermi's Golden Rule the transition rate, R_{fi}, from an initial state ϕ_i to a final state ϕ_f is given by:

$$R_{fi} \;=\; 2\pi \int dE_f \rho(E_f) |V_{fi}|^2 \delta(E_f - E_i)$$

Here, E_i and E_f are the energies of the initial and final states, $\rho(E_f)$ is the density of the final states. For time-independent potentials, if $V(x)$ is the interaction term of the Lagrangian, then V_{fi} is defined as $V_{fi} = \int d^3x \phi_f^*(x) V(x) \phi_i(x)$. Once the transition rates are known, production cross-sections and decay rates of particles can be calculated.

When the coupling constants are small, a perturbative expansion in the coupling constant is valid. However, when the coupling constant becomes large, it is not possible to use a (divergent) perturbation series to calculate the transition rates. The predictions of the Electroweak theory and Quantum Chromodynamics in the perturbative regime have enjoyed a remarkable success.

Quantum Chromodynamics (QCD) and the Electroweak Theory (EWK) comprise the Standard Model of particle interactions. The gauge group of the SM is $SU(3) \otimes$

$SU(2) \otimes U(1)$. $SU(3)$ describes the local gauge symmetry of QCD and $SU(2) \otimes U(1)$ describes the Electroweak theory.

1.1.1 Quantum Chromodynamics

The apparent violation of the Pauli principle in the existence of the Δ^{++} baryon (a uuu state), led to the hypothesis of the color quantum number. The color hypothesis was confirmed in e^+e^- experiments by the measurement of the ratio R ($\equiv \frac{\sigma(e^+e^- \to hadrons)}{\sigma(e^+e^- \to \mu^+\mu^-)}$) [5]. Quarks come in three colors and gluons in their eight colored combinations. The QCD Lagrangian is invariant under local color transformations of the quarks and gluons and hence the gauge group of QCD is SU(3). The QCD Lagrangian is given by:

$$L_{\rm QCD} \;=\; i\sum_q \bar{\psi}_q^\alpha \gamma^\mu (D_\mu)_{\alpha\beta} \psi_q^\beta - \sum_q m_q \bar{\psi}_q^\alpha \psi_q^\alpha - \frac{1}{4} F_{\mu\nu}^{(a)} F^{(a)\mu\nu}$$

The field tensor is defined $F_{\mu\nu}^{(a)} = \partial_\mu A_\nu^a - \partial_\nu A_\mu^a + g_s f_{abc} A_\mu^b A_\nu^c$, and the covariant derivative is defined $(D_\mu)_{\alpha\beta} = \delta_{\alpha\beta}\partial_\mu - i g_s \Sigma_a \frac{\lambda^a_{\alpha,\beta}}{2} A_\mu^a$. Here, g_s is the QCD coupling constant, f_{abc} are the SU(3) structure constants, $\lambda^a_{\alpha,\beta}$ are the generators of the SU(3) Lie algebra, $\psi_q^\alpha(x)$ are the 4 component Dirac spinors corresponding to each quark field of color α and flavor q, and the $A_\mu^a(x)$ are the Yang-Mills gluon fields. "Asymptotic freedom" of color interactions implies that the *renormalized* QCD coupling is small, or accessible to perturbative analysis, in the regime of high momentum transfer. In high energy collisions, therefore, the implications of QCD can be tested to high accuracy. The dependence of the coupling constant on momentum transfer, and the concept of renormalization are briefly discussed later in this chapter. A considerable progress has also been made in the non-perturbative regime where the coupling constant is large [10].

Isolated quarks have never been observed in nature. There is no rigorous proof based on QCD why isolated quarks should never be observed. However, a hypothesis of quark "confinement" is proposed, which is supported by a number of simplified phenomenological models. According to confinement, colored objects (quarks or gluon)

promptly form colorless hadrons. Only colorless final states are observed experimentally.

1.1.2 The Electroweak Theory

The Electroweak theory starts with massless particles W^i_μ, $i = 1, 2, 3$ and B_μ. The W^i_μ form a triplet under weak isospin (T), while B_μ is an isosinglet under this symmetry. Consequently, the gauge group of the W^i_μ is SU(2). The isosinglet B_μ is invaraint under local gauge (U(1)) transformations of the "weak hypercharge" (Y). In terms of the the charge of a particle (Q), and the third component of its weak isospin (T_3), the weak hypercharge is given by $Y \equiv 2(Q - T_3)$. Therefore the EWK gauge group is $SU(2) \otimes U(1)$. The corresponding coupling constants are g and g'. The physical fields ($W^\pm$, Z^0 and γ) are given by linear combinations of the W^i_μ and B_μ fields. The left handed fermion fields of the i^{th} fermion family, $\psi_i = (\nu_i \quad l_i^-)^T$ and $(u_i \quad d_i')^T$ transform as doublets under SU(2). Here, $d_i' \equiv \Sigma_j V_{ij} d_j$ and V_{ij} are the elements of the Cabibbo-Kobayashi-Maskawa (CKM) matrix [15]. The CKM matrix describes the weak eigenstates of down-type quarks, d_i', in terms of their mass eigenstates d_i. The right handed fields transfrom as $SU(2)$ singlets. At this point all the particles in the theory are massless. In the Minimal Standard Model, in order to give masses to the physical fields, a scalar Higgs field is postulated that transforms as a doublet $\phi = (\phi^+ \quad \phi^0)^T$ under SU(2) transformations, carries a non-zero hypercharge and is colorless. The potential energy of the EWK Lagrangian has a minimum for non-zero expectation values of the Higgs field. The minimum of the theory possesses a global $O(4)$ (rotational) symmetry in ϕ which is necessarily broken in the choice of a particular ground state ϕ_0. This "Spontaneous Symmetry Breaking" [5] gives rise to massless scalar bosons called *Goldstone bosons*. Three of the Goldstone bosons become the longitudinal polarization states of the $W^\pm$ and Z^0 bosons, thus making the bosons massive. In addition, a neutral scalar particle, the "Higgs boson" (H) is introduced into the theory, whose mass is not predicted. The masses of the fermions in the theory are also generated through their interaction with the Higgs field. The

Lagrangian is then given by:

$$\begin{aligned} L_{\text{EWK}} &= \sum_i \bar{\psi}_i \left(i\gamma^\mu \partial_\mu - m_i - \frac{g m_i H}{2M_W} \right) \psi_i - e \sum_i q_i \bar{\psi}_i \gamma^\mu \psi_i A_\mu \\ &- \frac{g}{2\sqrt{2}} \sum_i \bar{\psi}_i \gamma^\mu (1-\gamma^5)(T^+ W_\mu^+ + T^- W_\mu^-) \psi_i \\ &- \frac{g}{2\cos\theta_W} \sum_i \bar{\psi}_i \gamma^\mu (g_V^i - g_A^i \gamma^5) \psi_i Z_\mu \end{aligned}$$

Here, $\theta_W \equiv \tan^{-1}(\frac{g'}{g})$ is the weak angle, $e = g \sin\theta_W$ is the positron electric charge, $A \equiv B\cos\theta_W + W^3 \sin\theta_W$ is the massless photon field, $W^\pm \equiv \frac{W^1 \mp i W^2}{\sqrt{2}}$ are the massive charged weak boson fields, $Z \equiv -B\sin\theta_W + W^3 \cos\theta_W$ is the massive neutral weak boson field, $T^\pm$ are the weak isospin raising and lowering operators, $g_V^i \equiv t_{3L}(i) - 2q_i \sin^2\theta_W$ is the vector coupling, $g_A^i \equiv t_{3L}(i)$ is the axial or pseudo-vector coupling, $t_{3L}(i)$ is the weak isospin of the i^{th} fermion ($+1/2$ for u_i and ν_i; $-1/2$ for d_i and e_i) and q_i is the charge of the ψ_i in terms of e.

The violation of CP symmetry[8], so far only observed in the K^0 and $\overline{K^0}$ mesons, is accommodated in the SM by a single observable phase in the CKM matrix. The discovery of the Higgs boson is one of the foremost goals of the present and future generation of collider experiments.

1.2 The running of coupling constants

As mentioned earlier, the forces in gauge theories are proportional to certain characteristic coupling constants or charges. In the case of QED, the charge is the familiar electron charge. The electron charge (e) measured in experiments, say by the interaction of an electron and a photon, can be represented by the electron-photon couplings shown in figure 1-1. However, what the experiments measure is a sum of processes shown in figures 1-2(a)-(c), in terms of the "bare" electron charge (e_0). Here the term "bare" refers to the fact that the electron-photon interaction vertex has been stripped of higher order terms. This definition of the measured electron charge recognizes the fact that the diagram 1-2(a) in terms of the "bare" electron charge is modified as a result of the higher order interactions, and depends on the particular value of the

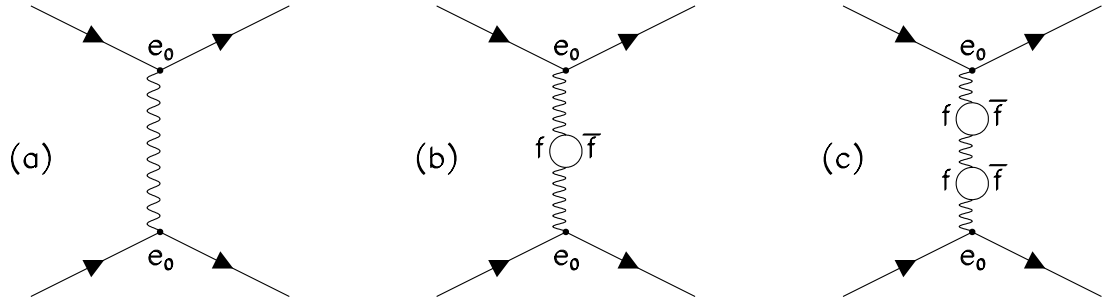

Figure 1-2: *Higher order corrections in Electromagnetic scattering. The $f\bar{f}$ loop diagrams modify the "bare" charge e_0 of the photon-fermion vertex into a value that is measured experimentally.*

virtual photon's momentum $(-Q^2)$. The total amplitude of the scattering process is given by a sum of all the diagrams in the perturbation series. If each of the higher order diagrams are individually calculated in terms of e_0, their amplitudes are found to be infinite. However, these infinities can be absorbed into a new *renormalized* electron charge, $e_R \equiv e$, in terms of which the amplitudes are finite. Renormalization, or the handling of infinities, requires that by a suitable redefinition of physical quantities, a theory is made finite to all orders in perturbation theory. Since the coupling constant $(\alpha \equiv \frac{e^2}{4\pi\hbar c})$ explicitly depends on Q^2, its value is given relative to a renormalization or reference momentum scale μ after summing over all orders in the perturbation expansion.

$$\alpha(Q^2) \;=\; \frac{\alpha(\mu^2)}{1 - \frac{\alpha(\mu^2)}{3\pi}\log\left(\frac{Q^2}{\mu^2}\right)}$$

This is the Q^2 evolution or *running* of the coupling constant which describes how the separation of two particles determines the effective charge seen by them. For QED, α increases very slowly from $\frac{1}{137}$ as Q^2 increases. The formation of new fermion-antifermion loops, as mass thresholds for fermions f are reached, also contributes to the variation.

In QCD, the strong coupling constant α_s evolves due to the presence of higher order diagrams as shown in figure 1-3. The behavior of α_s is very different from α

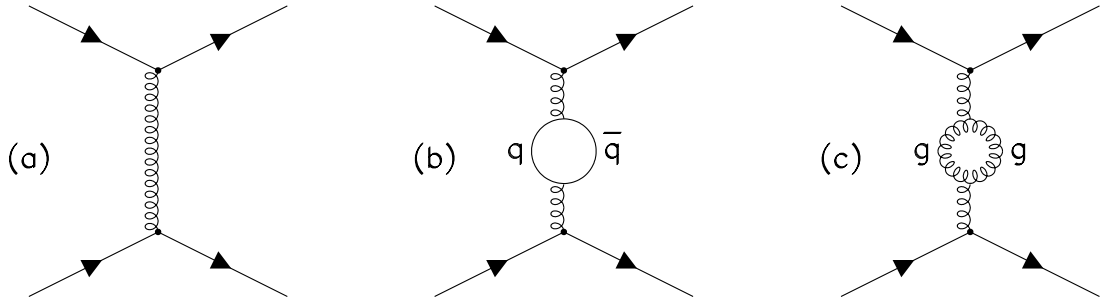

Figure 1-3: *Higher order corrections in strong scattering. Since QCD is a non-Abelian theory, the higher order diagrams include contributions from both quark and gluon loops.*

because QCD is a non-Abelian theory, and therefore, there are extra diagrams coming from the self coupling of gluons. For n_f quark flavors, the Q^2 evolution of α_s is given by:

$$\alpha_s(Q^2) = \frac{\alpha_s(\mu^2)}{1 + \frac{\alpha_s(\mu^2)}{12\pi}(33 - 2n_f)\log\left(\frac{Q^2}{\mu^2}\right)}$$

Since the number of (known) quark flavors is six, α_s decreases with larger Q^2 (shorter distance), leading to *asymptotic freedom*. This allows the application of a perturbative approach to calculate amplitudes in the regime of high momentum transfer. It is customary to denote the Q^2 scale at which the coupling constant becomes large by Λ^2:

$$\Lambda^2 = \mu^2 \exp\frac{-12\pi}{(33 - 2n_f)\,\alpha_s(\mu^2)}$$

In terms of Λ^2, the running of α_s is given by:

$$\alpha_s(Q^2) = \frac{12\pi}{(33 - 2n_f)\log\left(\frac{Q^2}{\Lambda^2}\right)}$$

$\Lambda \sim 200-250$ MeV[6] marks the point of transition between perturbative and non-perturbative QCD. For $t\bar{t}$ production, the momentum transfer is high, and therefore, perturbation theory can be used to calculate the production cross-sections.

1.3 Fragmentation and Jets

Individual partons (quarks and gluons) carry the color charge, and though they can initially considered to be free during a hard collision (or in the decay $t \rightarrow bW \rightarrow bq_iq_j$), they will undergo *fragmentation* or *hadronization* that organizes them into colorless hadrons. Typically it involves the creation of additional quark-antiquark pairs from the vacuum by the color force field, one of which is picked up by the energetic initial quark. When a quark and an antiquark separate, their color interaction becomes stronger. Due to the interaction of gluons with one another, the color force field lines between the quark-antiquark pair are squeezed into a tube-like region. If this *color tube* has a constant energy density per unit length, then the potential energy between the quark and the antiquark will increase linearly with distance with the important consequence of total *confinement* of quarks to colorless hadrons. The separating quark-antiquark pair stretches the color tube until the increasing potential energy makes the creation of additional quark-antiquark pairs energetically favorable. This process continues until the energetic initial individual partons have been converted into clusters of quarks and gluons with zero net color and low internal momentum, and therefore very strong colored couplings. In this way initial partons are converted into showers of hadrons, or *jets* that travel more or less in the direction of the initial partons. Experimentally they manifest themselves as large deposition of energy in localized groups of calorimeter cells in a particle detector.

Fragmentation is governed by soft non-perturbative processes that are dealt with using semi-empirical models, and cannot be calculated from first principles. Consider an energetic parton k with energy E_k which produces a hadron h with an energy fraction $z \equiv \frac{E_h}{E_k}$ $(0 \leq z \leq 1)$. The *Fragmentation function*, $D_k^h(z)$ gives the probability, $D_k^h(z)dz$, of finding h in the range z to $z + dz$. Fragmentation functions are often parameterized in terms of constants N and n by [5]:

$$D_k^h(z) \quad = \quad N\frac{(1-z)^n}{z}$$

1.4 Outline of the thesis

A brief outline of the thesis is as follows: The second chapter presents the experimental and theoretical arguments that necessitate the existence of the top quark. It also summarizes the discovery of the top quark by the CDF and DØ collaborations. The third chapter introduces the CDF detector and the processing of the data used in this thesis. The fourth chapter describes the expected signal from top quark decays, the data sample used in this thesis and the kinematic variables used to reduce the background to a top quark signal. The fifth chapter describes the method used for the identification of jets from b and c quarks, and its use for reducing backgrounds from light quarks and gluons. The sixth chapter details the calculation of all the Standard Model physics background processes to the top quark signal in this analysis. The seventh chapter presents the counting experiment and the $t\bar{t}$ production cross-section calculation. Finally, the eighth chapter summarizes the result and suggests some future improvements.

Chapter 2

Theory of Top Quark Production and Decay

The Standard Model provided several theoretical and experimental arguments for the existence of the top quark even before its discovery. Some of those arguments are presented in this chapter. After motivating the necessity for the top quark, its production mechanism at the Tevatron and its decay modes are discussed. The most important pieces of evidence for the existence of the top quark are the results of the CDF and DØ collaborations that led to its discovery. Their results are summarized in this chapter.

2.1 Necessity for the Top quark

As mentioned chapter 1, the top quark is a member of the third generation of quarks and leptons. By 1974, two generations of quarks and leptons were known. The tau lepton (τ) was the first member of the third generation of particles to be discovered [11]. The discovery of the Υ ($b\bar{b}$ state) at Fermilab [12] indicated the existence of the bottom quark. The charge of the bottom quark was inferred from the measurement of the leptonic width of the Υ to be $Q_b = -1/3e$ [13] where e is the magnitude of the electron charge. The leptonic width is proportional to the square of the charge of the b quark and can be calculated using phenomenological potential models of $q\bar{q}$ bound

states [14]. With the discovery of the b quark, and a detailed study of its properties over the years, evidence accumulated that indicated the existence of the top quark. It was clear then that the CKM matrix would have to be a 3×3 matrix, as anticipated earlier by Kobayashi and Maskawa [15]. They observed that if the CKM matrix had a third generation, it would allow for CP violation, so far observed in K^0 mesons, through the inclusion of a complex phase. Some of the evidence is summarized below. A detailed review can be found elsewhere [20].

2.1.1 Suppression of the FCNC decays of the b quark

Empirically it is known that the b quark decays. In the Standard Model quark decays are only possible through the mediation of W bosons. If the b quark were a left handed singlet and decayed through the mediation of electroweak bosons, then Flavor Changing Neutral Current (FCNC) decays of the b quark would be seen. The branching ratio predictions for a singlet b quark are $BR(B \rightarrow Xl^+l^-) \geq 0.12$ and $BR(B \rightarrow Xl\nu) \simeq 0.026$ [16]. If however the b quark were a member of a doublet then the FCNC decays would be suppressed by the GIM mechanism [17]. The GIM mechanism asserts that in the charged current weak interactions (i.e. mediated through the exchange of W bosons) the weak eigenstates of the down-type quarks are not their mass eigenstates d_i, but linear combinations $d_i' \equiv \Sigma_j V_{ij} d_j$, where V_{ij} are the elements of the Cabibbo-Kobayashi-Maskawa (CKM) matrix. The current limit on flavor changing neutral current decay $b \rightarrow sl^+l^-$ at 90% confidence level is 1.2×10^{-3}, set by the CLEO experiment [18].

The GIM mechanism also ensures that the decay $B^0 \rightarrow \mu^+\mu^-$ is supressed. The dominant diagram for the decay is shown in figure 2-1, and is similar to the diagram for $K_L \rightarrow \mu^+\mu^+$. The SM predictions for the branching ratios are $\sim 10^{-11}$ and $\sim 10^{-9}$ for the B_d^0 and B_s^0 mesons respectively. The current limits, set by CDF, are $\mathrm{Br}(B_d^0 \rightarrow \mu^+\mu^-) < 1.6 \times 10^{-6}$ and $\mathrm{Br}(B_s^0 \rightarrow \mu^+\mu^-) < 8.4 \times 10^{-6}$ at 90% confidence level [19]. If the b quark were a singlet then there would be no GIM suppression and the branching ratios would be significantly higher.

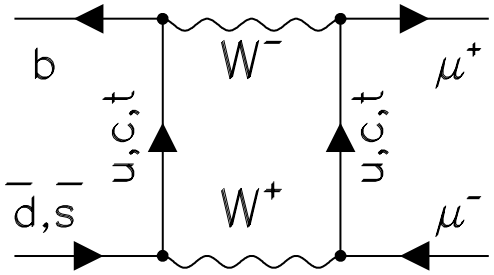

Figure 2-1: *Standard Model diagram for the decay* $B_d^0/B_s^0 \to \mu^+\mu^-$.

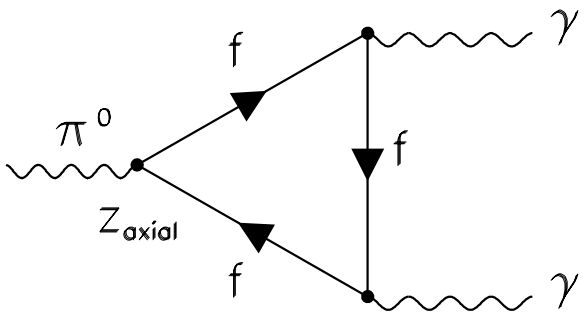

Figure 2-2: *The triangle anomaly diagram responsible for the decay* $\pi^0 \to \gamma\gamma$.

2.1.2 Cancellation of anomaly diagrams

A classical Lagrangian in a field theory may have certain continuous symmetries. By Noether's theorem [5], there are conserved currents associated with these symmetries. These currents are still expected to be conserved once the theory is quantized. This is not true in general for gauge invariant theories like EWK and QCD. This reduction of symmetries upon quantization is termed an *anomaly* and is present in both Abelian and non-Abelian gauge theories. The presence of anomalies in a theory is an important issue. An axial current with an anomaly cannot be treated like a vector current because it makes the theory non-renormalizable, unless some other fields in the theory cancel the anomaly diagrams. The existence of three generations of quarks and leptons is required for the cancellation of such anomaly diagrams. The anomaly diagram responsible for the decay $\pi^0 \rightarrow \gamma\gamma$ is shown in figure 2-2. For the Electroweak theory to be renormalizable, the sum of anomaly diagrams for all fermions must vanish. The contribution for each fermion is proportional to $N_c g_A^f Q_f^2$ where N_c is the number of colors each fermion can have ($N_c = 1$ for leptons and $N_c = 3$ for quarks), g_A^f is the axial coupling to the Z of each fermion and Q_f is the charge of the fermion. The contribution of each quark doublet exactly cancels the contribution of its corresponding lepton doublet. Therefore, with the presence of three lepton doublets, three quark doublets are required.

2.1.3 Measurement of the weak isospin of the b quark

Understanding the $Z \rightarrow b\bar{b}$ vertex in e^+e^- collisions permits us to measure the weak isospin of the b quark. Figure 2-3 shows the leading order Feynman diagram for the process. Consider a generalized $SU(2) \otimes U(1)$ interaction where the b quarks have both left and right-handed couplings, L_b and R_b respectively, which can be written as:

$$L_b = I^b_{L_3} - e_b sin^2\theta_W \quad (2.1)$$

$$R_b = I^b_{R_3} - e_b sin^2\theta_W \quad (2.2)$$

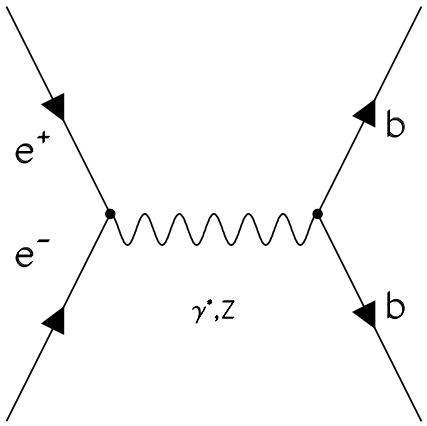

Figure 2-3: *Diagram for* $Z \rightarrow b\bar{b}$ *decay in* e^+e^- *collisions.*

Here $I^b_{L_3}$ ($I^b_{R_3}$) is the third component of the weak isospin of left-handed (right-handed) b quarks, e_b is the charge of the b quark and θ_W is the Weinberg angle ($sin^2\theta_W = 0.2321$[6]). The SM coupling includes the left-handed term only. Knowing the couplings, $I^b_{L_3}$ and $I^b_{R_3}$ can be measured directly from experiment. The partial width , $(Z \rightarrow b\bar{b})$ is proportional to $L_b^2 + R_b^2$. The forward-backward asymmetry for the process $e^+e^- \rightarrow \gamma^*/Z^0 \rightarrow b\bar{b}$, $A_{FB} \equiv \frac{N(forward)-N(backward)}{N(forward)+N(backward)}$, can be measured below and at the Z^0 pole. $N(forward)$ ($N(backward)$) is the number of number of b quarks produced with $\theta > 90°$ ($\theta < 90°$), where θ is the polar angle of the b quark in the e^+e^- center of mass frame, measured from the direction of flight of e^-. Below the Z^0 resonance, with $\gamma - Z^0$ interference, A_{FB} varies as $(L_b - R_b)$ and at the Z^0 resonance, the asymmetry measures $\frac{L_b^2 - R_b^2}{L_b^2 + R_b^2}$. Recent measurements of A_{FB} ($A_{FB} = 0.107 \pm 0.013$) [6] are consistent with the Standard Model prediction of $0.0995 \pm 0.002 \pm 0.003$ for $I^b_{L_3} = -\frac{1}{2}$ and $I^b_{R_3} = 0$ [6]. This implies that the left-handed b quark is a part of a doublet and the right-handed b quark is a singlet. Therefore, the weak isospin partner of the left-handed b quark should have $I_{L_3} = \frac{1}{2}$ and charge $q = +\frac{2}{3}e$.

2.1.4 Other results from precision Electroweak measurements

Large data samples of Z events at the LEP and SLD experiments enable us to measure several electroweak quantities precisely. The level of precision of these measurements requires the inclusion of radiative corrections to the tree level predictions for a comparison between the data and the theory. Electroweak predictions for higher order radiative processes can be used to extract the top quark and Higgs boson mass by a comparison to the results of the precision measurements.

The free parameters of the Standard Model are the electromagnetic coupling α, the weak coupling constant G_{Fermi}, the strong coupling α_s, the Weinberg angle θ_W, the mass of the Higgs boson, the masses of the six quarks, the masses of the six leptons and the four quark mixing parameters that determine the CKM matrix. The most precisely measured Standard Model parameters are α, G_{Fermi} and M_Z. Using these, different quantities can be predicted at the tree level. However, once radiative corrections are taken into account, a dependence on the masses of the fermions and the Higgs boson is also included. For M_Z, the mass of the top quark enters as a quadratic term M_{top}^2/M_Z^2 while the mass of the Higgs has a logarithmic dependence of the form $(\ln(M_{Higgs}/M_Z))$. Figure 2-4 shows the diagrams responsible for radiative corrections to M_Z from the top and the Higgs.

Some of the electroweak quantities surveyed at LEP and SLD include the forward-backward assymetry for the $Z \to \ell^+\ell^-$, $Z \to b\bar{b}$ and $Z \to c\bar{c}$ decays at the Z pole, the left-right assymetry ($A_{LR} \equiv \frac{(\sigma_L - \sigma_R)}{(\sigma_L + \sigma_R)}$, where σ_L and σ_R are the Z boson production cross-sections at the Z pole with left and right handed electrons respectively) and the ratio of the $b\bar{b}$ and $c\bar{c}$ widths to the hadronic widths ($R_b \equiv {}_{,}{}^{b\bar{b}}/_{Z}{}_{,}{}^{hadrons}/_{Z}$ and $R_c \equiv {}_{,}{}^{c\bar{c}}/_{Z}{}_{,}{}^{hadrons}/_{Z}$ respectively) [6].

The decay $Z \to b\bar{b}$ is sensitive to the top quark mass through electroweak vertex corrections. The dependence of the partial widths on the mass of the Higgs arises mostly due to the corrections to the Z propagator. In the ratio, R_b, most of the Higgs mass and α_s dependencies cancel allowing an indirect determination of the mass of the top quark independent of the mass of the Higgs boson. The $Zb\bar{b}$ vertex is also

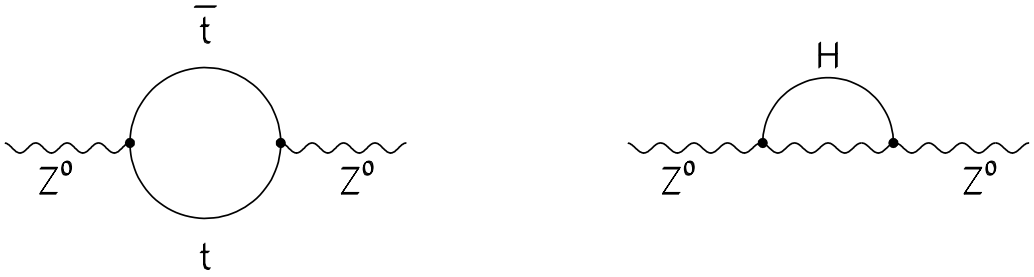

Figure 2-4: *Diagrams for radiative corrections to the Z boson mass involving the top and the Higgs.*

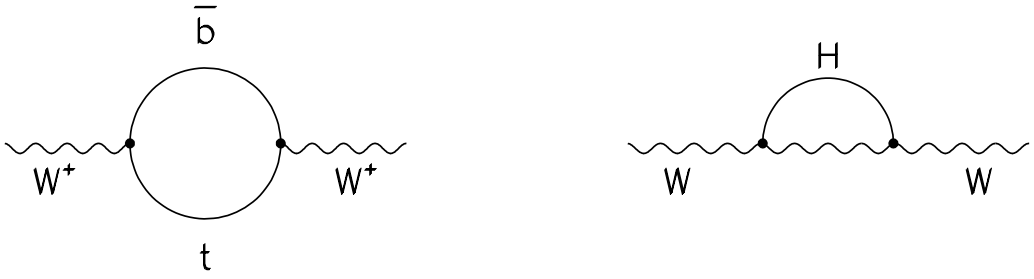

Figure 2-5: *Diagrams for radiative corrections to the W boson mass involving the top, the bottom and the Higgs.*

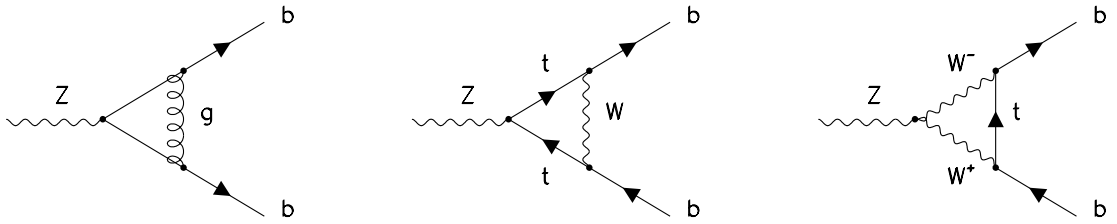

Figure 2-6: *Some of the diagrams for QCD and top quark corrections to the $Zb\bar{b}$ vertex.*

sensitive to physics beyond the Standard Model. Some of the QCD and top quark corrections to the $Zb\bar{b}$ vertex are shown in figure 2-6.

The mass of the W boson is also dependent on the mass of the top quark and the Higgs boson. For a fixed mass of the Higgs, a precise measurement of the W mass constrains the mass of the top quark. Alternatively, a precise determination of the masses of the W boson and the top quark can be used to determine the mass of the Higgs, M_H. The dependence of the W mass on the Higgs mass is only logarithmic, therefore the current constraints on M_H are weak. Figure 2-5 shows the diagrams responsible for radiative corrections to M_W from the top, the bottom and the Higgs boson.

The data from Z decays and the W mass measurement can be combined to fit for the top quark mass. The best indirect determination of the top quark mass comes from a combination of data from LEP, SLD, Fermilab and νN scattering. The fit value is $M_{top} = 178 \pm 8^{+17}_{-20}$ GeV/c^2 [6].

2.1.5 Beyond the top quark

The measurements of the Z width at the LEP and SLC colliders have ruled out the existence of a fourth generation neutrino with a mass $m \leq M_Z/2$. Unless the fourth generation neutrino is very massive, the discovery of the top quark completes the experimentally allowed generations in the Standard Model currently.

The mass of the top quark is not predicted by the SM. As it will be described later, the mass of the top quark has been measured to be 176.8 ± 6.5 GeV/c^2 by the CDF collaboration, which is approximately 40 times more than the mass of its partner, the b quark. Though arguments based on electroweak symmetry breaking through radiative corrections exist in local supersymmetric theories [21] to explain such a high top quark mass, the Standard Model offers no reasons.

2.2 Top quark Production

Since the top quark is heavy, it can only be produced in colliders with sufficiently high center of mass energy. In e^+e^- collisions, top quark pairs are produced through a γ or a Z. Since the highest center of mass energies available today are $\sqrt{s} \approx M_Z \approx 170$ GeV (LEP), top production cannot be explored at e^+e^- colliders for $M_{top} > 86$ GeV/c^2. The ep collisions at HERA have a center of mass energy of ≈ 310 GeV, but the top production cross-section is too small for observation. Much higher energies have been obtained at hadron colliders. The $p\bar{p}$ collider at Fermilab (the Tevatron) has a center of mass energy of $\sqrt{s} = 1.8$ TeV. Therefore currently, top quark production can only be observed at the Tevatron. There are two production mechanisms for top quark production in $p\bar{p}$ collisions for top masses greater than M_W. They are pair production, $p\bar{p} \rightarrow t\bar{t}X$, and single top production, $p\bar{p} \rightarrow tX$.

2.2.1 Top quark pair production $p\bar{p} \rightarrow t\bar{t}X$

The leading order Feynman diagrams are shown in figure 2-7. The process $p\bar{p} \rightarrow t\bar{t}X$ consists of both $q\bar{q} \rightarrow t\bar{t}$ (quark annihilation) and $gg \rightarrow t\bar{t}$ (gluon fusion) diagrams. $t\bar{t}$ production is dominated by the $gg \rightarrow t\bar{t}$ process up to $M_{top} \approx 90$ GeV/c^2. For higher top masses, the $q\bar{q}$ process is the dominant one [20]. This is because the production of a heavy top quark pair requires the initial partons to carry a large fraction of the total momentum of the proton or the anti-proton. Since the gluons typically carry only a small fraction of the total momentum, the $gg \rightarrow t\bar{t}$ process is suppressed. At the Tevatron, approximately 90% of the $t\bar{t}$ production cross-section is from $q\bar{q}$

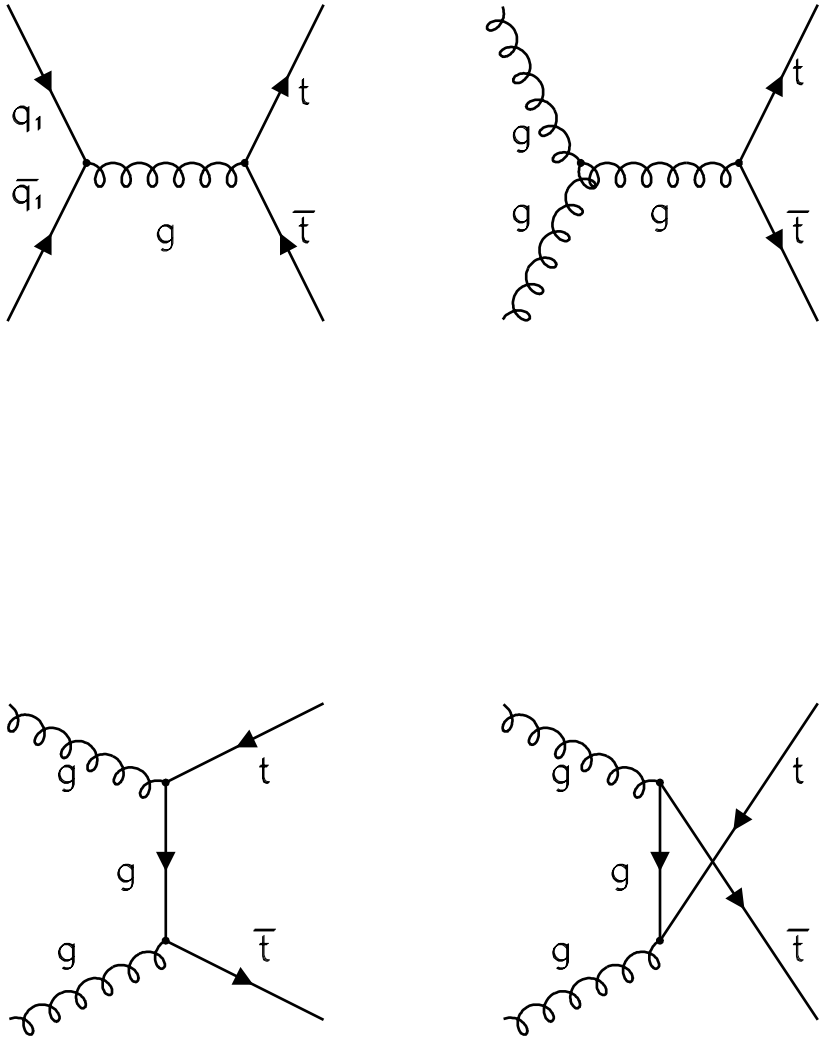

Figure 2-7: *Leading order diagrams for $t\bar{t}$ pair production at CDF.*

annihilation.

The cross-section for pair production can be calculated using perturbative QCD. It is a product of the parton distribution functions inside the protons (and the anti-protons) and the parton-parton point cross sections.

$$\sigma(p\bar{p} \rightarrow t\bar{t}) = \Sigma_{a,b} \int dx_a F_a(x_a, \mu^2) \int dx_b F_b(x_b, \mu^2) \hat{\sigma}_{ab}(\hat{s}, \mu^2, M_{top}) \qquad (2.3)$$

Here, the indices a and b refer to the components of the protons and the anti-protons respectively. F_a and F_b are the (number) densities, or parton distribution functions evaluated at a momentum scale μ. The quantity $F_a(x_a, \mu^2)dx_a$ is the probability that a parton of type a (quark, anti-quark or gluon) carries a momentum fraction between x_a and $x_a + dx_a$ of the proton (or the anti-proton). $\hat{\sigma}_{ab}$ is the point cross-section for the process $ab \rightarrow t\bar{t}$ and $\hat{s} = x_a x_b s$ is the square of the center-of-mass energy of the parton-parton interaction.

The renormalization scale, μ, is the arbitrary parameter introduced in the renormalization procedure. It has the units of energy and is taken to be of the order of the mass of the top quark. The exact result for the cross-section should be independent of the value chosen for μ. However, calculations are performed to finite order in perturbative QCD, and therefore all cross-section calculations are dependent on μ. F_a and F_b are extracted from parameterizations of fits to experimental results in deep inelastic scattering [6].

There are two main sources of uncertainty in the calculation of $t\bar{t}$ production cross-section. The first is due to the uncertainty in the renormalization scale μ used in the perturbative calculation. The size of this uncertainty is usually estimated by varying the value of μ around the top quark mass. The second source of uncertainty is in the knowledge of the parton distribution functions, F_i, and in the assumed value of the QCD parameter, Λ_{QCD}. The value of Λ_{QCD} determines the evolution of α_s and hence the parton distribution functions with μ^2. It is also important in the extraction of the gluon distribution functions from deep inelastic scattering data. The uncertainty due to the parton distribution functions is estimated by studying the variations in the calculated cross-section for different parameterizations of the parton

Calculation	$\sigma_{t\bar{t}}$
Laenen et al., [22]	$4.94^{+0.71}_{-0.45}$ pb
Berger et al., [23]	$5.52^{+0.07}_{-0.45}$ pb
Catani et al., [24]	$4.75^{+0.63}_{-0.68}$ pb

Table 2.1: A summary of $p\bar{p} \rightarrow t\bar{t}$ cross-sections at the Tevatron for a top quark of mass 175 GeV/c^2. All calculations are Next-to-leading order and use gluon resummation.

distribution functions, and for different values of Λ_{QCD}. The total theoretical uncertainty in the calculated cross-section is approximately 20%, with the two sources of uncertainty from renormalization scale and parton distribution functions contributing approximately equally.

Next-to-leading order, or $O(\alpha_s^3)$, calculations of $t\bar{t}$ production cross-section are available. In a calculation by Laenen, Smith and van Neerven [22], corrections due to initial state gluon brehmstrahlung have been resummed to all orders in perturbative QCD. These corrections are large near the $t\bar{t}$ threshold. Their calculation introduces an infrared cutoff $\mu_0 >> \Lambda_{QCD}$ where the resummation is terminated. The resummation diverges as $\mu_0 \rightarrow 0$ because of dominant non-perturbative effects. The corrections from gluon brehmstrahlung are positive at all orders of the perturbative calculation. Therefore, the lower limit on the $t\bar{t}$ cross-section is estimated by the sum of the full $O(\alpha_s^3)$ prediction and $O(\alpha_s^4)$ correction (taking $\Lambda_{QCD} = 105$ MeV). The best estimate of the cross-section includes the full effect of gluon resummation. The dominant source of uncertainty is in the choice of μ_0 which is allowed to become small.

Calculations using perturbative resummation of gluon radiative corrections use Principal Value Resummation techniques [23, 24] which are independent of μ_0. Theoretical uncertainties in the cross section calculation are estimated by varying μ. Figure 2-8 shows the different $t\bar{t}$ production cross sections as a function of the mass of the top quark. Table 2.1 gives a summary of the various theoretical calculations

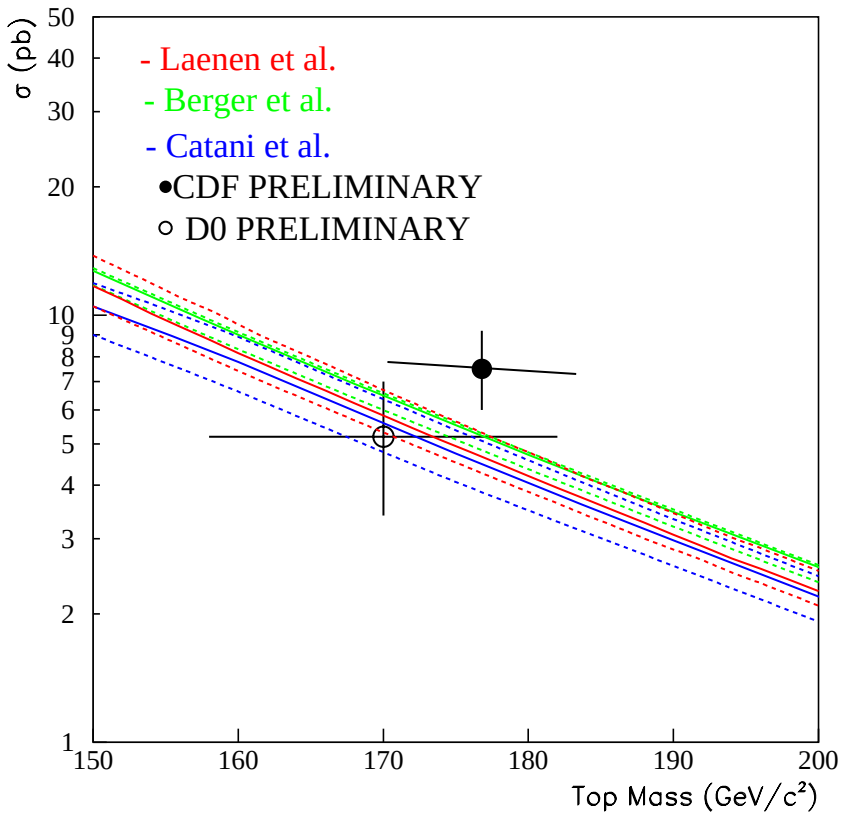

Figure 2-8: *Theoretical predictions for $t\bar{t}$ production cross-section as a function of the top quark mass. CDF and DØ measurements of the production cross-section are also shown.*

of $t\bar{t}$ production at the Tevatron for a top quark of mass 175 GeV/c^2.

The theoretical $t\bar{t}$ production cross-sections are in the range of $\sim 4-6$ pb for a top quark of mass 175 GeV/c^2. It must be noted that the total inelastic cross-section in $p\bar{p}$ collisions is about 60 mb which is approximately ten orders of magnitude higher than the $t\bar{t}$ production cross-section.

2.2.2 Single top quark production $p\bar{p} \rightarrow tX$

The leading order diagrams for the production of single top are shown in figure 2-9. There are two dominant processes for single top production, W-gluon fusion

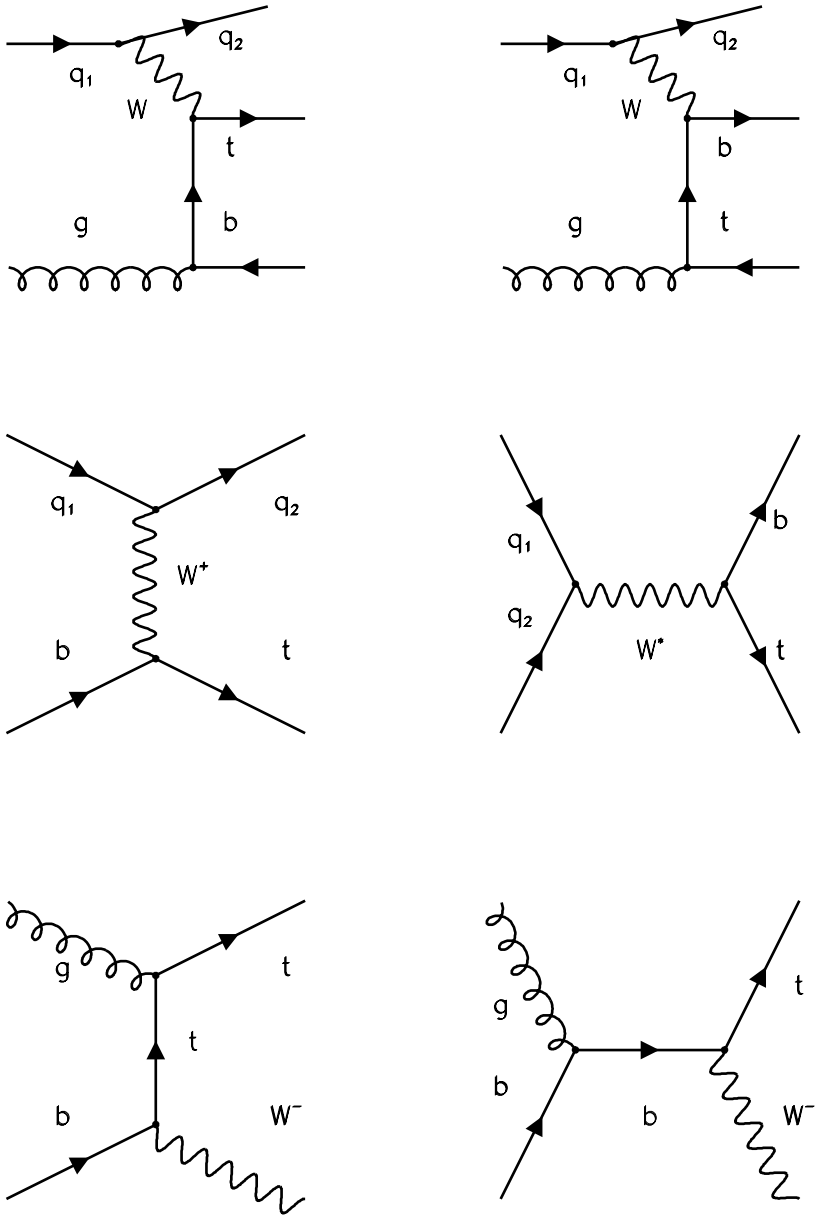

Figure 2-9: *Leading order diagrams for single top production in $p\bar{p}$ collisions.*

and W^* production. The cross-sections for these processes for a top quark mass of 175 GeV/c^2 are 1.44 ± 0.43 pb and 0.74 ± 0.04 pb respectively. Several tree level calculations of single top production are available [25]. The systematic uncertainties in the calculation can be large because the matrix element is calculated at tree level. In this thesis, we only consider the pair production of top quarks. As shown in Chapter 6, the contribution from single top quark production to our final data sample is negligible due to the kinematical requirements of our analysis.

2.3 Top quark decay

Due to QCD confinement, quarks are not observed as free particles, but form hadronic bound states. The top quark, because of its high mass, decays before it can form a hadronic state. The top quark undergoes the Standard Model decay $t \rightarrow Wb$, where the W boson is real. This decay mode is not CKM suppressed. Decays into Ws and Wd final states also occur, but are suppressed by CKM matrix factors of $|V_{ts}|^2/|V_{tb}|^2 \approx 10^{-3}$ and $|V_{td}|^2/|V_{tb}|^2 \approx 5 \times 10^{-4}$ respectively [6]. The top quark lifetime is of the order of 10^{-24} seconds for a mass of ≈ 175 GeV/c^2. Hadronization is a non-perturbative process, and is estimated to take place at a time-scale of $\Lambda_{QCD}^{-1} \approx 10^{-23}$ seconds. According to a model of top quark hadronization [26] the t and $\bar{t}$ produced in the hard scatter are linked by color strings to the remnants of the proton and the anti-proton. When the separation of the quarks and the proton remnants exceeds about 1 fm, the color strings are expected to break to produce fragmentation particles. A heavy top quark decays before it travels that distance. Even if the top quark undergoes hadronization, its effects would be very hard to observe experimentally. This is because the expected fractional energy loss of the (massive) top quark during hadronization is small. The fragmentation of the b quark produced in the top decay might be affected more, because the color string would link the b quark to a light quark produced in top fragmentation rather than a light quark from the remnants of the proton.

2.3.1 Decay modes of the Top quark

The decay mode of the $t\bar{t}$ pair is characterized by the decay modes of the W bosons produced in the $t\bar{t} \rightarrow bW\bar{b}W$ decay as shown in figure 2-10. Table 2.2 summarizes the different decay modes of the $t\bar{t}$ pair and their lowest order Standard Model branching fractions.

The $t\bar{t}$ events are classified according to the number of W bosons that decay leptonically. In approximately 5% of $t\bar{t}$ decays, each W boson decays into a $e\nu$ or $\mu\nu$ pair. This is the *dilepton* mode which is experimentally characterized by two high p_T charged leptons, substantial missing transverse energy from the two undetected neutrinos and two b quark jets. This final state is very clean, but has a low branching ratio. About 30% of the time, one W decays into leptons and the other into jets. This is the *lepton+jets* channel, which yields a single high p_T lepton, large missing transverse energy, and (usually) 4 jets in the final state including two from the b quarks. The backgrounds in this channel can be reduced by a combination of kinematic requirements and the identification of b quark jets. In the *fully hadronic* final state both W bosons decay into jets, yielding no leptons, low missing transverse energy and (nominally) six jets in the final state. Although the branching ratio for this decay mode is the largest (44%), it faces formidable QCD backgrounds making the identification of $t\bar{t}$ signal difficult[27]. In 21% of the cases, the $t\bar{t}$ pair decays into a final state containing at least one τ lepton.

2.4 The discovery of the Top quark

In 1995 the CDF and DØ collaborations reported the observation of the top quark. Each experiment had roughly a 5σ excess of $t\bar{t}$ candidate events over the background. Both experiments also reconstructed peaks in the mass distribution corresponding to the quark top mass. The results of the two collaborations are summarized below.

Decay mode	Branching ratio
$t\bar{t} \longrightarrow (q\bar{q}'b)(q\bar{q}'\bar{b})$	36/81
$t\bar{t} \longrightarrow (q\bar{q}'b)(e\nu\bar{b})$	12/81
$t\bar{t} \longrightarrow (q\bar{q}'b)(\mu\nu\bar{b})$	12/81
$t\bar{t} \longrightarrow (q\bar{q}'b)(\tau\nu\bar{b})$	12/81
$t\bar{t} \longrightarrow (e\nu b)(\mu\nu\bar{b})$	2/81
$t\bar{t} \longrightarrow (e\nu b)(\tau\nu\bar{b})$	2/81
$t\bar{t} \longrightarrow (\mu\nu b)(\tau\nu\bar{b})$	2/81
$t\bar{t} \longrightarrow (e\nu b)(e\nu\bar{b})$	1/81
$t\bar{t} \longrightarrow (\mu\nu b)(\mu\nu\bar{b})$	1/81
$t\bar{t} \longrightarrow (\tau\nu b)(\tau\nu\bar{b})$	1/81

Table 2.2: Modes for $t\bar{t}$ decay, and their lowest order Standard Model branching ratios.

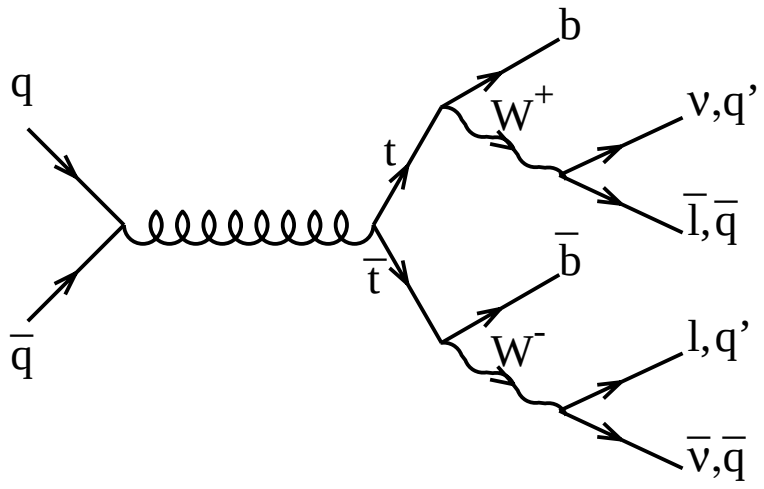

Figure 2-10: *Standard Model decay modes of the $t\bar{t}$ pair.*

2.4.1 CDF results

The CDF collaboration announced the discovery of the top quark in the dilepton and the lepton+jets mode using 67 pb^{-1} of data accumulated during Run 1A and a part of Run 1B. The latest results [28, 29], using all the data from Run 1A and Run 1B, corresponding to an integrated luminosity of ~ 110 pb^{-1}, are summarized below.

In the dilepton mode [30], nine candidate events are observed: one ee, one $\mu\mu$ and seven $e\mu$. Backgrounds in the dilepton channel arise from Drell-Yan production of lepton pairs, diboson (WW,ZZ) production, $Z \rightarrow \tau^+\tau^-$ decay, $b\bar{b}$ production and fakes. The backgrounds are estimated using a combination of data and Monte Carlo. The total background in the $ee + \mu\mu$ ($e\mu$) channel is 1.3 ± 0.4 (0.8 ± 0.2) events. Combining these numbers with the total acceptance of $(0.74 \pm 0.08)\%$ (for the CDF's measured top mass of 175 GeV/c^2 as described below) yields a cross-section of $\sigma_{t\bar{t}} = 8.5^{+4.4}_{-3.4}$ pb.

In the lepton+jets channel two different analyses are pursued. Since a large background from QCD W+jets production is present, the b quark jets in the event are identified or "tagged" to enhance the signal to background ratio. In one approach, the low momentum leptons coming from the decay $b \rightarrow l\nu X$ or $b \rightarrow c \rightarrow l\nu X$ are identified. This technique is called "Soft Lepton Tagging" (SLT). In the other approach, the secondary vertices resulting from the decay of long lived ($\tau \approx 1.5 \times 10^{-12}$s) b quark mesons are identified. This method is known as "Secondary Vertex Tagging" (SVX tagging). Chapter 5 deals with SVX tagging in detail. In the SLT analysis [31], 40 candidate events are observed over a background of 22.5 ± 2.8. Using a total acceptance of $(1.7 \pm 0.2)\%$, this corresponds to a cross-section of $\sigma_{t\bar{t}} = 9.2^{+4.3}_{-3.6}$ pb. In the SVX analysis [32], 34 candidate events are observed over a background of 9.5 ± 1.5. The total acceptance of the analysis is $(3.7 \pm 0.4)\%$. This yields a cross-section of $\sigma_{t\bar{t}} = 6.2^{+2.1}_{-1.7}$ pb. Figure 2-8 compares the CDF measured cross-section in the leptonic modes to the different theoretical predictions.

CDF has also measured the top quark mass by reconstructing the candidate events according to a $t\bar{t}$ hypothesis. A constrained fit is performed on lepton+4-jet events

arising from the process $t\bar{t} \rightarrow WbW\bar{b} \rightarrow l\nu qqb\bar{b}$. The data sample is divided into four non-overlapping subsets, in order of decreasing signal to background ratio: events with two SVX tags, events with a single SVX tag, events with SLT tags (but no SVX tags) and events with no tags. The mass resolutions for each of the subsets are determined, and then each subset is fit to a combination of background and $t\bar{t}$ for different masses of the top quark. The top quark mass that maximizes the likelihood of the fit for each subset is the mass measured in that subset. Finally, the results of the mass measurement in different subsets are combined by using a global likelihood function. The largest systematic sources of uncertainty are the effects of fragmentation and incomplete knowledge of the energy of the jets. The final measurement is $M_{top} = 176.8 \pm 4.4(stat) \pm 4.8(syst)$ GeV/c^2.

2.4.2 DØ results

The DØ collaboration has also observed $t\bar{t}$ production in the dilepton and lepton+jets channel. Their final results from Run 1A and Run 1B data, corresponding to an integrated luminosity of ~ 125 pb^{-1} are summarized below [33].

In the dilepton channel, 3 candidate $e\mu$ events are seen over a background of 0.21 ± 0.15. One ee ($\mu\mu$) event is seen over a background of 0.47 ± 0.07 (0.73 ± 0.20). DØ also searches for $t\bar{t}$ production in the $e\nu$ channel. In this channel, they require *one* isolated high transverse momentum electron, large transverse energy and two or more jets in the event. The selection requirements are made orthogonal to the dilepton channel. In the $e\nu$ channel, 4 events are observed over an expected background of 1.16 ± 0.34.

In the lepton+jets channel, the signal to background ratio is enhanced using two different methods. In the first method topological and kinematic cuts are applied and in the second, low momentum muons coming from the decay of the b quarks are identified (in a manner similar to Soft Lepton Tagging used by CDF). In the kinematic cuts approach, 19 candidate events are observed over a background of 8.7 ± 1.7. In the soft muon tagging approach, 11 events are observed over a background of 2.4 ± 0.5. A total of 39 events are observed in the dilepton, $e\nu$ and lepton+jets channels combined

over a background of 13.6 ± 2.1. Using the acceptance for the measured top quark mass of 170 GeV/c^2 at DØ (as described below) the cross-section is measured to be $\sigma_{t\bar{t}} = 5.8 \pm 1.8$ pb. Figure 2-8 compares the DØ measured cross-section in the leptonic mode to different theoretical predictions.

DØ uses a constrained fit method similar to CDF's to reconstruct $t\bar{t}$ events. A "top likelihood" cut is applied on the data to reduce the background without introducing significant bias in the mass distribution of the background. The largest systematic sources of uncertainty are the jet energies and the effect of Monte Carlo modelling of background and signal. The final measurement is $M_{top} = 173.3 \pm 5.6(stat) \pm 6.2(syst)$ GeV/c^2.

2.4.3 Search for the fully hadronic decay mode of $t\bar{t}$ pairs

At CDF, two parallel but complementary analyses were followed to search for the fully hadronic decay of $t\bar{t}$ pairs [34]. Both of the analyses start from a common data sample composed of events with at least 5 jets and passing certain kinematic requirements.

The first analysis [35] requires the presence of at least one b quark jet in an event and imposes additional strict kinematic requirements to reduce the background from QCD multijet production. In Run 1A and 1B data, 187 events passing the selection requirements of the analysis are observed over an expected background of 141.9 ± 12.2. Using a total acceptance of $(4.4 \pm 0.9)\%$, a cross-section of $9.6^{+4.4}_{-3.6}$ pb is measured.

The second analysis is the subject of this thesis. It requires the identification of at least two b quark jets in an event. The details of the analysis are found in subsequent chapters.

The mass of the top quark has been measured in the fully hadronic decay mode by fitting 6-jet events passing the selection requirements of the first analysis to a $t\bar{t}$ hypothesis. The observed mass spectrum is fit to a combination of background and $t\bar{t}$ signal using a likelihood technique for different masses of the top quark, analogous to the method followed for the mass measurement in the lepton+jets channel. The measured value is $180 \pm 10(stat) \pm 12(syst)$ GeV/c^2. The dominant sources of uncertainty are gluon radiation, fragmentation effects and an incomplete knowledge of the

jet energies.

2.5 Monte Carlo Simulation of $t\bar{t}$ Production

Top production is usually modelled using QCD parton shower Monte Carlo programs. These include ISAJET [36], HERWIG [37] and PYTHIA [38]. The initial hard parton scatter is generated from leading order matrix elements that are convoluted with the parameterizations of the parton distribution functions. The outgoing initial and final state partons are then converted into a cascade of gluons and $q\bar{q}$ pairs with energy and angular distributions according to Altarelli-Parisi kernels [5]. The cascade is terminated when the invariant mass of the parton in the cascade falls below an infrared cutoff where perturbative QCD breaks down. The remaining partons are then hadronized according to phenomenological models. The *underlying event* or the products of hadronization of the remnants of the proton and the anti-proton are also dealt with phenomenologically according to models that have been tuned to describe soft (i.e. low Q^2) $p\bar{p}$ collision data. Particles are decayed according to the their measured lifetimes and branching ratios. The final output of Monte Carlo simulation programs is a list of stable particles that are fed into the detector simulation.

The main difference between the different Monte Carlo generators is in the handling of radiation processes. HERWIG and PYTHIA take into account the color correlations between all partons in the initial and the final state. ISAJET employs an independent fragmentation model where the radiation from each parton is also independent of the rest of the event.

Since the Monte Carlos are based on leading-order matrix elements and subsequent initial and final state radiation according to different models, it is instructive to compare their predictions with the next to leading order (NLO) calculations in QCD. Different comparisons have been performed between HERWIG and the next to leading order QCD calculations [39]. It is seen that there is an excellent agreement in the shapes of distributions of quark rapidity, transverse momentum and the mass of the $t\bar{t}$ pair. NLO QCD single top quark transverse momentum and rapidity distributions

including the effect of resummation of soft gluons have also been studied and found to be in agreement with the NLO QCD calculations that agree with HERWIG [39]. Therefore, in this analysis, the HERWIG Monte Carlo is used to model $t\bar{t}$ production and decay.

Chapter 3

The Tevatron and the Collider Detector at Fermilab

The Collider Detector at Fermilab (CDF) [40] is one of two general purpose detectors built to study $p\bar{p}$ interactions at the Tevatron Collider in Fermilab. The other detector is DØ. The Tevatron is the world's most powerful collider, with a center of mass energy of $\sqrt{s} = 1.8$ TeV. CDF is an azimuthal and forward-backward symmetric detector that was first commissioned in 1987. Since then it has been upgraded several times.

3.1 The Tevatron

The protons used in the Tevatron come from Hydrogen which is ionized to form H^-. The resulting ions are accelerated to 750 KeV in a Cockroft-Walton electrostatic generator and then to 200 MeV in a linear accelerator (LINAC). The ions emerge from the LINAC through a carbon foil that strips their outer electrons leaving only protons. The protons are then injected into the Booster ring, a synchrotron accelerator, where they are accelerated to 8 GeV and formed into bunches. From the Booster, the proton bunches are collected and injected into the Main Ring, which is also a synchrotron accelerator.

The Main ring consists of 4 miles of alternating dipole (bending) and quadrupole

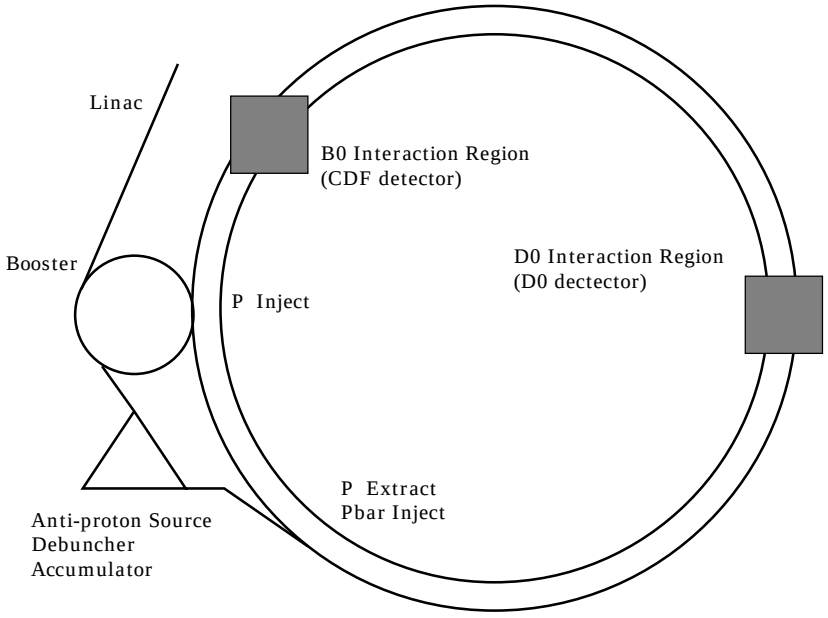

Figure 3-1: *A schematic view of the Tevatron at Fermilab. The two experiments CDF and DØ are also shown.*

(focusing) magnets. The Main ring also contains RF cavities that boost the protons to 150 GeV. The proton bunches are then coalesced into one and injected into the Tevatron or sent to the fixed target experimental facilities. Protons from the Main ring are also used for the source of anti-protons. Protons are removed from the Main ring and collide with an external Tungsten target to produce secondary particles including anti-protons. The anti-protons are then stochastically cooled [41] to a very low momentum in the Anti-proton Debuncher before being sent to the Accumulator loop which creates 8 GeV bunches of anti-protons. They are then injected into the Main ring where they are accelerated to 150 GeV, and then sent to the Tevatron.

In the Tevatron, the protons and the anti-protons are accelerated to 900 GeV, and they circulate in opposite directions in the 5.7T magnetic field of superconducting dipole magnets. There are six proton and six anti-proton bunches. The time between each bunch crossing is 3.5 μs. A schematic view of the Tevatron at Fermilab is shown in figure 3-1.

3.1.1 The 1992-1995 Collider Run

The data used in this thesis were collected in the 1992-1995 collider run (*Run 1*). A total of $\sim$ 110 pb^{-1} of data were collected in two parts, "Run 1A" and "Run 1B". Run 1A (Aug 1992 - May 1993) collected $\sim$ 19 pb^{-1} and Run 1B (Jan 1994 - July 1995) collected $\sim$ 90 pb^{-1}. The main differences between the two runs were the replacement of the Silicon Vertex Detector and the higher instantaneous luminosities of the Tevatron.

3.2 The Collider Detector at Fermilab (CDF)

The protons and the anti-protons in the Tevatron are made to collide at two interaction regions, where the two collider detectors CDF and DØ are situated respectively. At CDF, the beam is approximately circular in cross-section, with a width of $\sim$ 40 μm. The beam has an approximately Gaussian longitudinal profile with a standard deviation of $\sim$ 30 cm.

3.2.1 Overview

The CDF detector is described in detail elsewhere [40]. The detector is capable of tracking charged particles, measuring particle momentum and providing good resolution calorimetery information in $p\bar{p}$ collisions. Figure 3-2 shows a side view of a quadrant of the detector.

CDF employs a right-handed co-ordinate system in which the z-axis lies in the proton direction, the y-axis points upwards and the x-axis points radially outwards in the plane of the Tevatron. Figure 3-2 also shows the CDF co-ordinate system. The nominal interaction point is taken to be the geometric center of the detector, (0,0,0). The polar angle θ is measured relative to the positive z direction. Instead of using the angle θ, the rapidity y, or pseudo-rapidity η is used. Rapidity is defined as $y = \frac{1}{2} ln \left(\frac{E+p_z}{E-p_z} \right)$. Under a boost in the z direction to an inertial frame with a velocity β, rapidity transforms as $y \rightarrow y + tanh^{-1}\beta$. Therefore, the shape of the rapidity

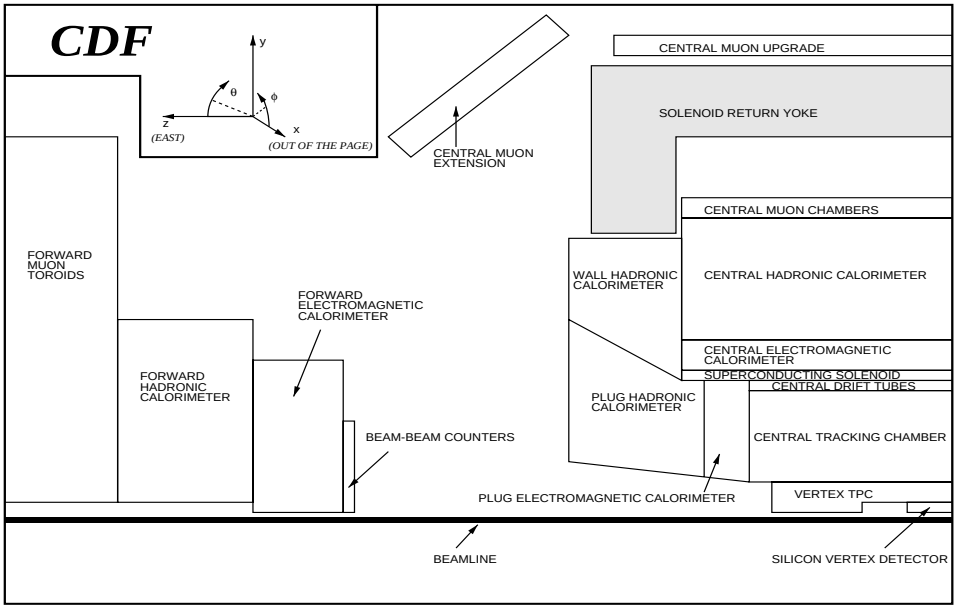

Figure 3-2: *A side view cross-section of the CDF detector. The interaction region is in the lower right corner. The detector is forward-backward symmetric about the interaction region. The CDF co-ordinate system is described in the upper left corner.*

distribution, dN/dy, is invariant under Lorentz transformations. For $p \gg m$, the rapidity of a particle is approximately equal to the pseudo-rapidity $\eta \equiv -ln\tan(\theta/2)$.

Particles produced at the interaction point encounter in succession a Beryllium beam pipe, several tracking chambers, a superconducting solenoid, calorimeters and muon chambers. The innermost tracking chamber is the Silicon Vertex detector (SVX) which surrounds the interaction point and is precise enough to provide information about displaced secondary vertices from b or c quark decays. After the SVX come the Vertex Time Projection Chambers (VTX) which reconstruct the z co-ordinates of the $p\bar{p}$ interactions. The Central Tracking Chamber (CTC) surrounds the VTX and provides particle tracking information. An axial magnetic field of 1.412 Tesla permeates the SVX, the CTC and the VTX. Electromagnetic and Hadronic calorimeters surround the CTC. Furthest from the beamline and shielded by thick steel plates are the muon chambers which detect minimum ionizing particles.

Luminosity at CDF is measured using the beam-beam counters. They consist of two planes of scintillation counters covering the angular range of 0.32° to 4.47° in both

the forward and backward directions ($3.24 < |\eta| < 5.88$). Hits in both counters that arrive coincident with the particle bunches crossing through the detector serve as both a minimum-bias trigger and the primary luminosity monitor. The rate of coincidences in these counters, divided by the effective cross section of the counters gives the instantaneous luminosity. The integrated luminosity is calculated similarly using the total number of coincidences in these counters. The instantaneous luminosity of a $p\bar{p}$ collider is given by:

$$\mathcal{L} = \frac{N_p N_{\bar{p}} N_B f}{4\pi\sigma^2} \tag{3.1}$$

Here, $N_p(\sim 2 \times 10^{11})$ and $N_{\bar{p}}(\sim 6 \times 10^{10})$ are the numbers of protons and anti-protons in each bunch. $N_B(= 6)$ is the number of bunches, f ($\sim$ 50 kHz) is the revolution frequency of each bunch and $\sigma(\sim 5 \times 10^{-5})$ cm^2 is the transverse cross-sectional area of each bunch. Typical and highest instantaneous luminosities for Run 1A were 0.54×10^{31} cm^{-2}s^{-1} and 0.92×10^{31} cm^{-2}s^{-1} respectively. Similarly for Run 1B, they were 1.6×10^{31} cm^{-2}s^{-1} and 2.8×10^{31} cm^{-2}s^{-1} respectively. Using the total $p\bar{p}$ inelastic cross section of $\sim$ 50 mb and a luminosity of $\sim 1.6 \times 10^{31}$ cm^{-2}s^{-1}, the observed interaction rate at the Tevatron is $\sim$ 1 MHz.

3.2.2 Tracking

Tracking of charged particles at CDF is done using three detector systems: the SVX, the VTX and the CTC. The Silicon Vertex Detector is used to identify displaced secondary vertices in this thesis. The SVX is a silicon microstrip vertex detector installed during Run 1A. Due to its degradation due to a cumulative exposure to radiation, the SVX was replaced by the radiation-hard SVX′ for Run 1B [42]. The two detectors are very similar. The comparison between the SVX and the SVX′ is shown in table 3.1.

The SVX consists of two barrels aligned along the $p\bar{p}$ beam direction. An isometric view of an SVX barrel is shown in figure 3-3. There's a gap of 2.15 cm between them at $z = 0$. The total active length of the SVX is 51 cm. Because $p\bar{p}$ interactions are Gaussian distributed along the beamline with $\sigma \sim 30$ cm, the geometric acceptance

Feature	SVX	SVX′
Channels	46080	46080
z coverage	51.1 cm	51.1 cm
Gap at z=0	2.15 cm	2.15 cm
Radius of layer 0	3.0049 cm	2.8612 cm
Radius of layer 1	4.2560 cm	4.2560 cm
Radius of layer 2	5.6872 cm	5.6872 cm
Radius of layer 3	7.8658 cm	7.8658 cm
Overlap of layer 0	-1.26°	0.17°
Overlap of layer 1	0.32°	0.32°
Overlap of layer 2	0.30°	0.30°
Overlap of layer 3	0.04°	0.04°
Silicon	one-sided	one-sided
Power	DC	AC, FOXFET bias
Passivation	none	polyimide
Atmosphere	Argon/Ethane+H_2O	Dry Nitrogen
Readout chip	SVX IC Rev. D	SVX IC Rev.H3
Sampling	quadruple	double
Noise	2200 electrons	1300 electrons
Gain	15 mv/fc	21 mv/fc
Reset/Integrate	3.5 μs	3.5 μs
Readout time	2.7 μs	2.1μs
Radiation Limit	15-20 KRad	$>$ 1 MRad
Bad channels	2.93%	1.73%
Typical Occupancy	7-10%	5%
Max Occupancy	12-20%	25%

Table 3.1: A comparison of the SVX and SVX′ detectors.

of the SVX is about 60%. The pseudo-rapidity coverage of the SVX is $|\eta| < 1.9$. Each barrel consists of four concentric layers of silicon strip detectors divided into twelve wedges of 30° each. Every layer in turn contains twelve *ladders*, each 25.5 cm in length. Figure 3-4 shows an SVX ladder. Each ladder contains three single sided silicon wafers, each 8.5 cm long. The readout strips of the silicon are aligned parallel to the barrel axis. The pitch of the readout strips is 60 μm for the inner three layers and 55 μm for the outer-most. They provide 2-D tracking information in the $r - \phi$ plane. Data is read out from the front end readout circuit by readout chips in a *sparse mode*, i.e. only those strips that are significantly above threshold are read out. Each chip has 128 readout channels, and there are 2, 3, 4 and 6 chips per ladder on layers 1 to 4 for a total of 46080 channels for the whole detector. The typical readout time is $\sim$ 2 ms which is one of the longest among the different detector systems at CDF. The readout circuits also enable a hardware subtraction of the leakage current, on a strip by strip basis. Individual hit position resolution of the SVX has been measured from data to be approximately 10 μm in the transverse plane. The impact parameter resolution distribution of the SVX′ detector is shown in figure 3-5 as a function of the track p_T.

The VTX is an Argon-Ethane drift chamber composed of 8 modules. Each module is octagonal, segmented into 8 wedges. The endcaps of the wedges are segmented into two sets of wires. One set is perpendicular to the beam line, and the other is perpendicular to the radial centerline of the wedges. By measuring the drift times of particles hitting the sense wires, a track can be reconstructed in the $r - z$ plane. VTX provides a pseudorapidity coverage of $|\eta| < 3.25$. The primary vertex of the event is determined by locating the convergence of all the reconstructed tracks in the event. The z resolution is 1-2 mm depending on the number of tracks in the event. The z resolution information provided by the VTX is used by the CTC for 3-dimensional reconstruction of tracks.

The CTC surrounds the VTX. It is a 3.2 m long cylindrical drift chamber and fits inside a superconducting solenoidal magnet that provides a 1.4 T magnetic field. The chamber consists of 84 layers of sense wires grouped into 9 superlayers (numbered 0

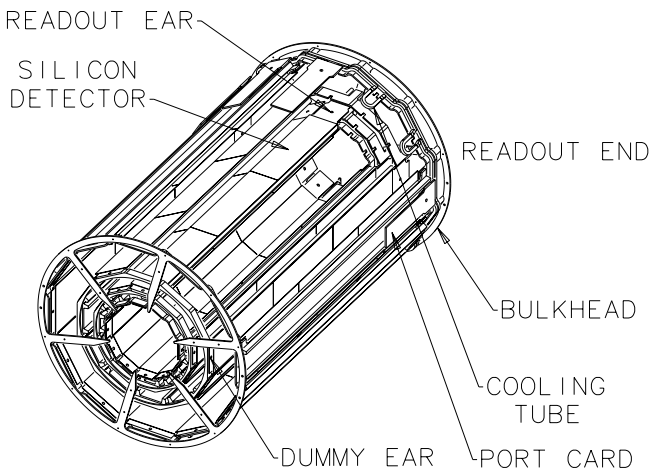

Figure 3-3: *An isometric view of a single SVX barrel. Some of the ladders of the outer layer have been removed to allow a view of the inner layers.*

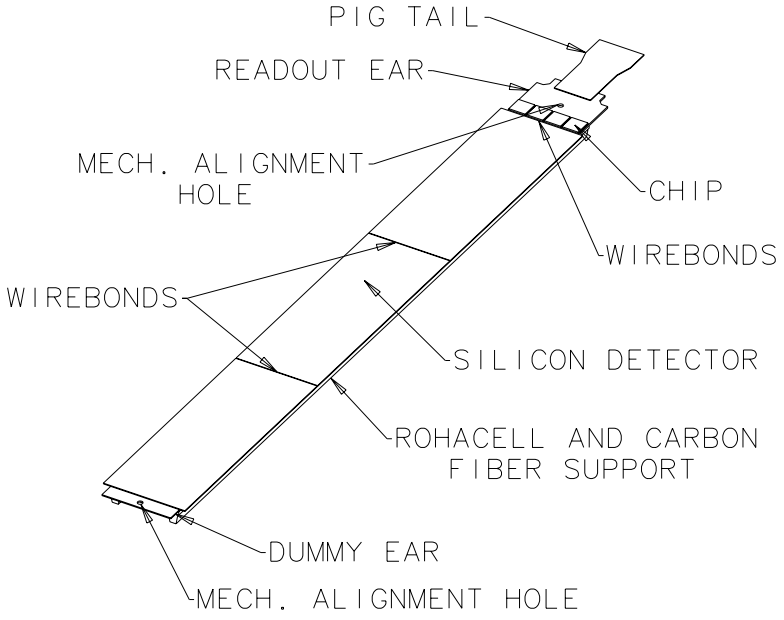

Figure 3-4: *An SVX ladder used in the construction of SVX layers.*

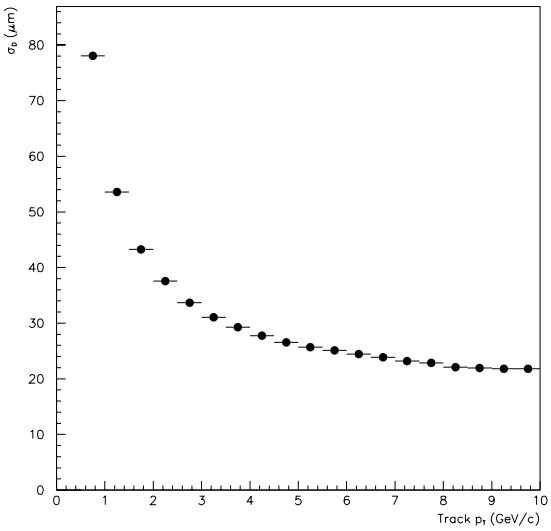

Figure 3-5: *Impact parameter resolution of the SVX (σ_D in μm) in the transverse plane as a function of track p_T.*

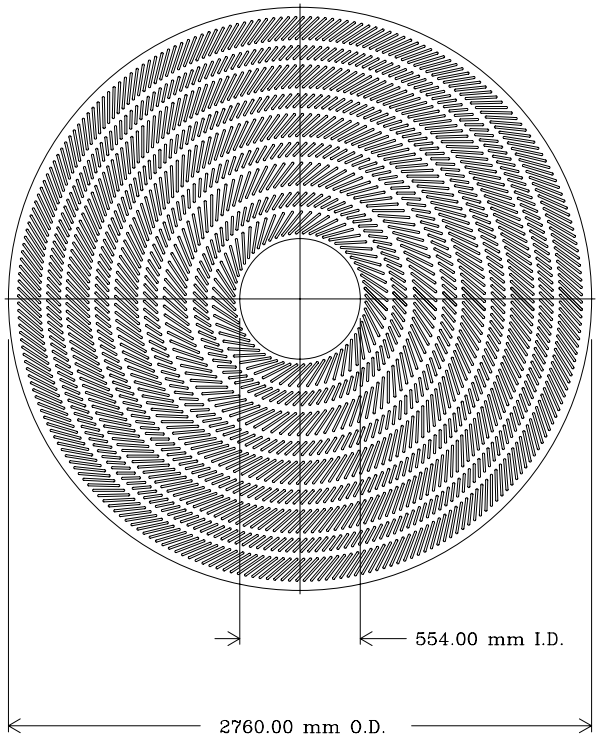

Figure 3-6: *A transverse view of the CTC endplate. The nine superlayers are shown.*

through 8), 5 axial and 4 stereo. The wire arrangement is shown in figure 3-6. The axial superlayers (layers 0, 2, 4, 6 and 8) consist of 12 wires each, arranged parallel to the beam direction. They allow track reconstruction in the $r-\phi$ plane. The stereo superlayers, interspersed between the axial superlayers, have 6 wires each, at $\pm 3^{\circ}$ to the axial direction ($+3^{\circ}$ for superlayers 1 and 5, -3° for superlayers 3 and 7), and enable track recontruction in the $r-z$ plane. Tracks with hits in the axial and stereo superlayers are termed 3-D tracks.

The superlayers are further sub-divided into cells. This results in a maximum drift time of 800 ns which is much shorter than the 3.5 μs between bunch crossings. Cells are tilted by 45° with respect to the radial direction in order to compensate for the Lorentz angle of the drift electrons in the crossed magnetic and electric fields (1350 V/cm). This results in drift electron trajectories that are perpendicular to the radial direction. The tilt also resolves the left-right ambiguity for tracks. The large tilt angle ensures that the tracks will come very close to at least one sense wire in each superlayer they cross. This is is exploited to separate closely spaced tracks during their reconstruction. Track reconstruction in the CTC involves fitting the hits of a track to the arc of a helix. The transverse momentum resolution for the CTC alone is $\frac{\delta p_T}{p_T^2} \approx 0.002$ GeV^{-1}c. The p_T resolution of the combined SVX-CTC system is $\frac{\delta p_T}{p_T} = \sqrt{(0.0009 p_T)^2 + 0.0066^2}$ or $\frac{\delta p_T}{p_T^2} \approx 0.002$ GeV^{-1}c.

3.2.3 Calorimeters

The solenoid and the tracking system of the CDF are surrounded by the calorimeters. Their coverage is 2π in azimuth and $|\eta| < 4.2$ in pseudorapidity. The calorimeters are segmented in pseudorapidity and azimuth to form a projective tower geometry which points back to the geometric center of the detector. The calorimeters are divided into three regions according to their pseudorapidity coverage: the central, the plug and the forward. Each region has an electromagnetic calorimeter (CEM,PEM,FEM) followed by a hadronic calorimeter (CHA/WHA,PHA,FHA). This aids electron identification on a tower-by-tower basis through a comparison of the electromagnetic and hadronic energies deposited. The absorber in all hadronic calorimeters is iron and in all elec-

tromagnetic calorimeters is lead. Table 3.2 summarizes the coverage, thickness and resolution of each of the calorimeters. (The symbol $\oplus$ means that the constant term is added in quadrature to the resolution.) The segmentation of the central towers is $\Delta\phi \times \Delta\eta = 15^\circ \times 0.1$. A scintillator is used as the active sampling medium in the central calorimeters. Proportional chambers with strip and wire readout (CES) are located at a depth of six radiation lengths in the CEM calorimeter, which approximately corresponds to the shower maximum for electromagnetic showers. The CES provides both the z and $r - \phi$ measurements of the shower position. The CPR is composed of proportional chambers located between the solenoid and the CEM. It provides $r - \phi$ information about the electromagnetic showers. The active medium in the plug and forward regions of the detector are gas chambers, and the segmentation is $\Delta\phi \times \Delta\eta = 5^\circ \times 0.1$.

System	η Coverage	Energy Resolution	Thickness
CHA	$\lvert\eta\rvert < 0.9$	$50\%/\sqrt{E_T} \oplus 3\%$	4.5 λ_0
WHA	$0.7 < \lvert\eta\rvert < 1.3$	$75\%/\sqrt{E_T} \oplus 4\%$	4.5 λ_0
PHA	$1.3 < \lvert\eta\rvert < 2.4$	$90\%/\sqrt{E_T} \oplus 4\%$	5.7 λ_0
FHA	$2.4 < \lvert\eta\rvert < 4.2$	$130\%/\sqrt{E_T} \oplus 4\%$	7.7 λ_0
CEM	$\lvert\eta\rvert < 1.1$	$13.7\%/\sqrt{E_T} \oplus 2\%$	18 X_0
PEM	$1.1 < \lvert\eta\rvert < 2.4$	$28\%/\sqrt{E_T} \oplus 2\%$	18-21 X_0
FEM	$2.2 < \lvert\eta\rvert < 4.2$	$25\%/\sqrt{E_T} \oplus 2\%$	25 X_0

Table 3.2: A summary of the properties of the different CDF calorimeter systems. Energy resolutions for the hadronic calorimeters are for incident pions, and for the electromagnetic calorimeters are for incident electrons and photons. (The symbol $\oplus$ means that the constant term is added in quadrature to the resolution.) λ_0 signifies interaction lengths and X_0 radiation lengths.

3.2.4 Muon Identification

The central muon system (CMU) consists of four layers of drift chambers located outside the CHA. The CHA acts as a hadron absorber for the CMU. Muons with $p_T \geq 1.5$ GeV/c and $|\eta| < 0.6$ are detected by the CMU. Four additional layers of drift chambers located outside the solenoid return yoke and shielded by an extra 0.6 m of steel comprise the central muon upgrade (CMP). The central muon extension (CMX) consists of four free-standing conical arches comprising of drift chambers sandwiched between scintillator counters extend the coverage of the CMU and CMP to $|\eta| < 1.0$. For all central muon systems, the muon p_T is determined from the tracking chambers inside the solenoid.

3.2.5 The trigger system

CDF has a four level trigger system, numbered 0 to 3. Each level accepts events that pass any of the electron, muon or jet triggers. An input (bunch crossing) rate of 280 kHz is reduced to ~ 5 Hz which is written to tape at the end of level 3.

The first three levels (0-2) are hardware triggers implemented within the frontend readout electronics. Level 0 requires a crossing of the proton and anti-proton bunches. The Level 1 decision is based on calorimeter and muon chamber information. An event passes Level 1 if there is a pair of contiguous calorimeter towers above threshold, or if there is a candidate muon stub in any of the central muon chambers. The Level 2 decision is based on calorimeter, tracking and muon information. The Central Fast Tracker (CFT) provides the tracking information using lookup tables of hit patterns to determine the p_T of candidate tracks. The CFT has a p_T resolution of $\frac{\delta p_T}{p_T^2} = 0.035$ GeV/c. Tracks identified by the CFT, together with the calorimeter and muon chamber information, are used to identify electron and muon candidates. A hardware calorimeter cluster finder provides information on energy clusters. It first searches for seed *trigger* towers above a threshold ($E_T \geq 3$ GeV) and then finds all neighbouring towers above a lower threshold ($E_T \geq 1$ GeV). The procedure is repeated until no new towers are found. The cluster E_t, average η and average ϕ is

computed. An event passes Level 2 if there's significant jet activity, or if there are electron or muon candidates in the event. The Level 2 accept initiates a full detector readout, the scan time is $\sim$ 30ms and results in a 10% deadtime.

Events passing Level 2 are sent to Level 3, which is a software trigger running approximately the same FORTRAN code as the offline analyses. All the channels of the detector are read out, digitized and recorded by the CDF's Data Acquisition System (DAQ). Electron and muon tracks are fully reconstructed in 3 dimensions, and are required to be associated to electromagnetic clusters or muon stubs. Events accepted by Level 3 are written to tape. The Level 3 output rate is determined by the maximum rate at which the events can be written to tape. Data is written out in a *bank* format, in which information for each event is stored separately according to different detector systems (i.e. CTC, SVX etc.) and physics objects (i.e electrons, muons, jets etc.).

3.2.6 Offline Reconstruction

Offline reconstruction of events involves the identification of the various physics objects and attributes of an event. Some of the aspects of offline reconstruction relevant to this analysis are the identification of the primary event vertex, the reconstruction of jets in the event and the determination of the missing transverse energy in the event. They are discussed below.

Primary Event Vertex Identification

The precise determination of the primary event vertex is crucial for the calculation of the kinematic properties of jets and also for the identification of displaced secondary vertices in an event. As mentioned earlier, within the CDF interaction region, primary vertices have a bivariate Gaussian distribution parallel and perpendicular to the beam axis, with $\sigma_{||} \sim 30$ cm and $\sigma_{\perp} \sim 35\mu$m. The beam and the CDF detector axes are not exactly parallel and have relative slopes of $\sim -3\mu$m/cm and $\sim 5\mu$m/cm in the vertical and horizontal planes respectively. The beam axis at the nominal

interaction point, $z = 0$, is displaced from the CDF detector axis. The displacements are $\sim 400 - 1000\mu$m in the vertical and $\sim 200 - 1200\mu$m in the horizontal plane. Both the slopes and the displacements vary due to changing Tevatron conditions, and are measured on a run-by-run basis. The accuracies are $\sim 4\mu$m/cm for the slope and $\sim 10\mu$m for the average displacement.

The primary vertex is determined on an event by event basis. Using appropriate corrections for detector offset and slope, a weighted fit of the SVX tracks and the VTX event vertex z position is performed. Tracks with large impact parameters are removed iteratively. The impact parameter, d, of a track is the distance of closest approach in the $r - \phi$ plane of a track to the primary vertex. The uncertainty in the fitted primary vertex co-ordinates perpendicular to the direction of the beam lies in the range $6 - 36$ μm depending on the topology and the number of tracks in the event.

Due to high luminosity conditions, a large fraction of events have multiple primary vertices that are separated along the beam axis. For these events, the event vertex with the highest total transverse momentum of attached tracks is chosen, and furthermore, all tracks used in the vertex fit and subsequent analysis are required to extrapolate within 5 cm of this vertex along the beam direction. For CTC tracks with $p_T \geq 2$ GeV/c, the resolution on the extrapolation to the z position along the beam axis is $\sim$ 6mm.

Offline jet reconstruction

As mentioned in Chapter 1, the fragmentation of quarks and gluons yields collimated showers of hadrons or jets. The CDF jet reconstruction algorithm uses a cone of fixed radius $\Delta R \equiv \sqrt{(\Delta\eta)^2 + (\Delta\phi)^2}$ in $\eta - \phi$ space [43]. This is because, the jets are approximately circular in $\eta - \phi$ space. If the average longitudinal and transverse components of the momenta of fragmentation particles with respect to the jet axis are k_T and k_L respectively ($k_T \ll k_L$), then the typical angular spread of the jet will be $\Delta\theta \approx k_T/k_L$ and $\Delta\phi \approx k_T/(k_L \sin\theta)$ in θ and ϕ respectively. Therefore, $|\Delta\eta| = |(d\eta/d\theta)\Delta\theta| \approx \Delta\phi$.

As a first step, the calorimeter towers in the Plug and Forward region are combined to match the $\eta - \phi$ segmentation of the central region of the detector: $\Delta\phi \times \Delta\eta = 15^\circ \times 0.1$. Then the electromagnetic (E_T^{em}) and hadronic (E_T^{had}) transverse energies in all the towers are summed to form the total transverse energy, (E_T). The electromagnetic transverse energy, $E_T^{em} \equiv E^{em} \sin\theta^{em}$, is calculated using the electromagnetic energy in the tower, E^{em}, and the polar angle between the true event vertex and the center of the tower, θ^{em}. E_T^{had} is defined analogously.

Jet clustering then proceeds in the following manner: All towers with $E_T > 1$ GeV are taken as seed towers. Seed towers that are adjacent to one another, on a corner or side, are then grouped to form pre-clusters. The E_T weighted center of the pre-cluster is computed in $\eta - \phi$ space. Pre-clusters are expanded to form clusters using a fixed cone algorithm. A cluster is then defined as the set of all towers with $E_T > 100$ MeV and within a distance ΔR from the centroid of the pre-cluster. The cluster centroid is recomputed and its set of towers redefined accordingly. This procedure is repeated until the set of towers in the cluster does not change. In order to prevent the final cluster center from drifting too far away from the initial pre-cluster center, initial pre-clusters are always kept in a cluster irrespective of their distance from the final cluster center. If a cluster belongs to a larger cluster, only the larger cluster is retained. If two clusters share towers, they are merged into a single cluster if the total E_T in common towers is greater than one half of the E_T of the smaller cluster. Otherwise overlapping towers are divided according to their distance to the respective cluster centers. Then the cluster centers are recomputed until a stable configuration is achieved.

Using the energy deposited in the calorimeters and the event vertex measured by the VTX, the jet "four-momenta" (E,$\mathbf{p}$) are computed by summing over the towers in the clusters. This is not the proper four-momentum of the jet since the mass is not the proper jet mass.

$$
\begin{aligned}
E &= \sum_i (E_i^{em} + E_i^{had}) \\
p_x &= \sum_i (E_i^{em} \sin\theta_i{}^{em} + E_i^{had} \sin\theta_i{}^{had}) \cos\phi_i
\end{aligned}
$$

$$p_y = \sum_i (E_i^{em} \cos \theta_i{}^{em} + E_i^{had} \cos \theta_i{}^{had}) \sin \phi_i$$
$$p_z = \sum_i (E_i^{em} \cos \theta_i{}^{em} + E_i^{had} \cos \theta_i{}^{had})$$

The jet transverse momentum $p_T \equiv \sqrt{p_x^2 + p_y^2}$, momentum $p \equiv \sqrt{\sum_i p_i^2}$, the pseudo-rapidity $\eta \equiv \frac{1}{2} ln \left(\frac{p+p_z}{p-p_z} \right)$ and the transverse energy $E_T \equiv E \frac{p_T}{p}$ are then defined. The detector pseudo-rapidity, η_d, is defined similarly to η, using the nominal interaction point $(x = 0, y = 0, z = 0)$ as the primary event vertex instead of the true event vertex determined as described previously.

The size of a jet varies slightly with its transverse momentum. Using a simple model of jet fragmentation, it can be estimated that the angular size of the cone containing half of the particles in a jet varies as $1/\sqrt{E}$, where E is the energy of the jet. Therefore, the size of the cone used to reconstruct jets is determined by the size of the jet. On average, about 70% of the jet energy is contained in a cone of radius ΔR =0.4 [44]. At CDF, the typical cone sizes used are 0.4, 0.7 and 1.0. As shown in table 3.2, the resolution of the jet transverse energy measurement is given by $\Delta E_T / E_T \sim 1/\sqrt{E_T}$. This relatively poor resolution is due to a number of reasons: the non-linear response of the calorimeters for charged hadrons and electrons or photons, the reduced response of the calorimeters at the boundaries between different calorimeter sub-systems, large fluctuations in the response of the calorimeters to hadron showers, loss of energy falling outside the clustering cone-size and the contribution of hadrons from the underlying event to the jet energies. All of these effects are discussed in detail in chapter 4.

Missing E_T measurement

The missing transverse energy, $\not\!\!E_T$, of an event is defined to be the negative of the vector sum of transverse energy in all calorimeter towers with $|\eta_d| < 3.6$. Towers with $|\eta_d| \geq 3.6$ are not taken into account because the parts of the forward hadron calorimeter are obscured by the final focusing magnets of the Tevatron. To be included in the sum, the total energies of individual towers are required to be greater than specific detector-dependent thresholds. These thresholds are 100 MeV in the CEM

and the CHA, 300 MeV in the PEM, 500 MeV in the PHA and the FEM, and 800 MeV in the FHA.

3.2.7 Simulation of the CDF Detector

In this thesis, all Monte Carlo events pass through a full CDF detector simulation [45], including the trigger system [46]. The underyling philosophy of the simulation is to parameterize the detector response instead of deriving it from first principles. The parameterizations are tuned to the data, either from $p\bar{p}$ collisions or from calibration runs of the various detector components in test beam experiments. The output of the detector simulations is analogous to the data collected using the CDF detector.

Chapter 4

Data Sample

The data sample used in this thesis and some of the kinematical requirements imposed on it are described in this chapter. First, the expected signal from $t\bar{t}$ production and decay is discussed. The trigger used to collect the data sample has been modelled on the expected $t\bar{t}$ decay signature. The efficiency for passing the trigger requirement is discussed for different masses of the top quark. After the trigger, additional kinematical requirements are imposed to clean up the data sample. This results in the *Pre-Selection* sample. A *Selection* sample is obtained by requiring further constraints on the energy, pseudo-rapidity and the number of jets in an event. The Selection sample is dominated by QCD production of jets from light quarks and gluons. In order to reduce this background, additional kinematical variables are investigated and the total transverse energy of the events is required to be greater than 300 GeV.

4.1 Signal Expectation

In the fully hadronic decay of the $t\bar{t}$ pair, we expect at least six partons in the final state. As discussed in chapter 1, due to the confining properties of the strong interactions, these partons manifest themselves as jets (i.e. collimated collections of particles). Though one would nominally expect six jets in the final state from $t\bar{t}$ decay, the actual number will vary. Jets may not pass the kinematical requirements of the analysis, or may overlap and be resolved as a single jet, and therefore result

in a smaller number of observed jets. On the other hand, a parton coming from $t\bar{t}$ decay may radiate a high p_T ("hard") gluon, thereby increasing the number of jets observed. The effect of gaining or losing jets is illustrated in Figure 4-1 which shows the expected number of jets produced in $t\bar{t}$ decays from HERWIG Monte Carlo after a full simulation of the CDF detector has been applied. Distributions are shown for two cases, one in which the $t\bar{t}$ pair is allowed to decay to all possible final states (inclusive) and the other in which the $t\bar{t}$ pair is forced to decay hadronically (exclusive). It is seen that $\sim 98\%$ of the signal has four or more jets in the final state for both inclusive and exclusive decays.

Since the top quark is heavy, the decay of the $t\bar{t}$ pair produces a large total transverse energy in the event ($\Sigma E_T \sim 2m_t$)[1]. Figure 4-2 shows the total transverse energy of the final state *partons* in fully hadronic $t\bar{t}$ decay. Since some of the jets associated to the partons coming from $t\bar{t}$ decay may fail the acceptance requirements of the analysis, the total transverse energy observed in the final state can be lower.

Another signature of $t\bar{t}$ decay is the presence of two b quarks in the final state. The b quarks from top quark decay have a large p_T on average (~ 40 GeV/c). This, coupled with their long lifetime, implies that b quark hadrons travel a significant distance (~ 4 mm) in the laboratory frame before they decay. Therefore, they can be identified by searching for their decay vertices using the SVX detector, as described in the next chapter. These decay vertices are displaced from the primary interaction point of the protons and anti-protons. The c quark hadrons coming from the decay of b quarks, or from the $W \rightarrow c\bar{s}$ decay of the W bosons produced in $t\bar{t}$ decay also result in displaced decay vertices. The algorithm used to identify displaced decay vertices cannot distinguish between the decay vertices coming from b or c quark hadrons, it can only identify the jets associated to the displaced vertices. The efficiency for the identification of such jets reduces the number of identified b and c quark jets, and therefore most $t\bar{t}$ events do not have two identified b or c quark jets.

To summarize, the fully hadronic decays of the $t\bar{t}$ pairs are characterized by high

[1]Strictly speaking, the total energy in the event $\Sigma E \sim 2m_t$. The total transverse energy $\Sigma E_T \equiv \Sigma E \sin\theta$ can be lower because of the angle θ for each of the jets.

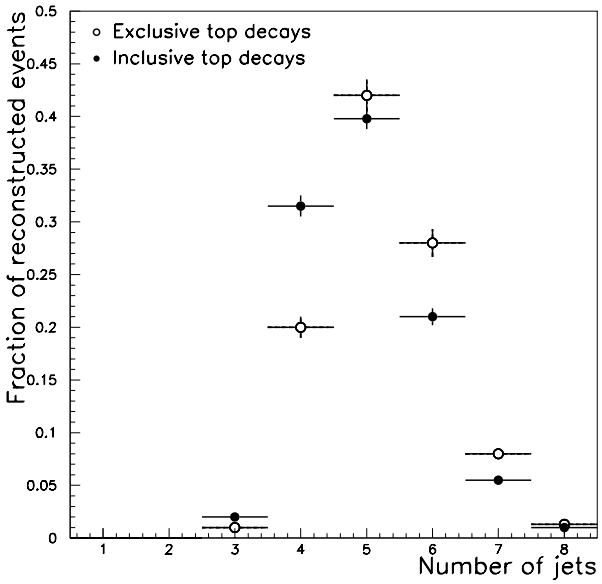

Figure 4-1: *A comparison of jet multiplicity distributions of inclusive ($t\bar{t} \rightarrow all$) and exclusive ($t\bar{t} \rightarrow jets\ only$) decays.*

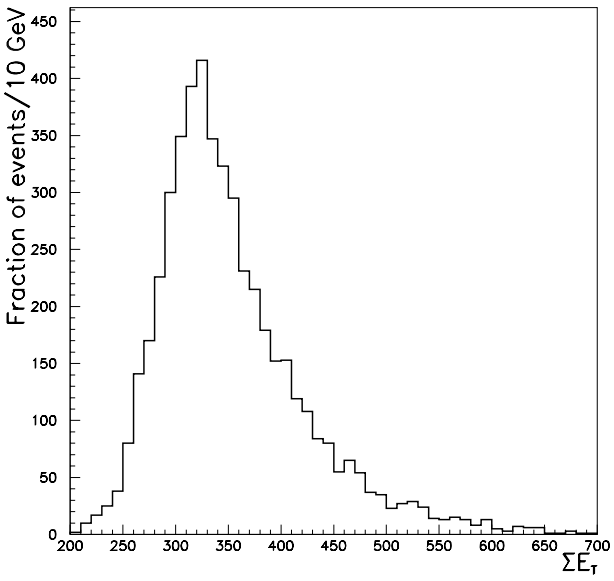

Figure 4-2: *Total transverse energy of all the partons in $t\bar{t}$ decay for a top quark mass of 170 GeV/c^2.*

jet multiplicity ($N_{jet} \geq 4$), large total transverse energy and the presence of b or c quark jets in the final state.

4.2 The Multijet Trigger

The data used in this thesis were collected using a dedicated Level 2 multijet trigger that was designed specifically for this analysis. In accordance with the discussion of the last section, the multijet trigger requires at least four energy clusters and a significant total transverse energy in an event. The requirements on the number of trigger tower clusters (N^{clus}), their minimum transverse energy (E_T^{clus}) and the total transverse energy in the event (ΣE_T^{clus}) are summarized in table 4.1. The trigger requirements are different for Runs 1A and 1B. For consistency, Run 1B Level 2 trigger requirements are imposed on Run 1A data in this thesis. For Run 1A and 1B combined, approximately 230,000 events pass the multijet trigger. No additional requirements are made for the Level 3 trigger.

Level 2	N^{clus}	E_T^{clus}	ΣE_T^{clus}
Run 1A	≥ 4	$\geq 10\ GeV$	$\geq 100\ GeV$
Run 1B	≥ 4	$\geq 15\ GeV$	$\geq 125\ GeV$

Table 4.1: Level 2 trigger requirements for Runs 1A and 1B.

4.2.1 The Trigger Behavior

The trigger response has been studied as a function of the E_T of the jets and the total transverse energy in the event [47]. As mentioned earlier in chapter 3, the definitions of energy clusters are different for the trigger and for the algorithm used to reconstruct jets in this analysis. The trigger clusters are formed by summing over all contiguous depositions of energy in the calorimeters. On the other hand, the algorithm used to reconstruct jets looks for the presence of energy in a fixed-cone of

certain radius in $\eta - \phi$ space. Therefore, a requirement that the transverse energy of a trigger tower cluster (E_T^{clus}) be greater than 15 GeV, does not imply that all the jets reconstructed with the fixed cone algorithm in the events passing this requirement, will have a transverse energy greater than 15 GeV. In reality, the fraction of fixed cone or "offline" jets that pass the $E_T^{clus} \geq 15$ GeV requirement at the trigger level will rise with their increasing transverse energy, and eventually reach a stable value. This is when the trigger is referred to as being "fully efficient". Similarly, since the total transverse energy requirement for the trigger is a sum of the energies of individual trigger clusters, the fraction of events that pass the trigger ΣE_T^{clus} requirement will also rise with an increasing offline total transverse energy. In 20% [47] of the cases, the energy flow in the region between two fixed cone jets is large enough that they can only be resolved as a single energy cluster at the trigger level. For jets with a small transverse energy ($\sim$ 15 GeV), this overlap of the energy can be significant.

To study the trigger efficiencies, a subset of a sample of events collected with an inclusive muon trigger (i.e. events containing one muon and anything else) is used [47]. These events contain a muon and a jet in the central region of the detector where the muon transverse momentum can be measured precisely. The jet has a trigger requirement of $E_T^{clus} \geq 15$ GeV. By looking at the offline transverse energy of jets passing the trigger E_T^{clus} requirement the behavior of the trigger can be mapped.

In this thesis, a simulation of the CDF trigger systems is used to determine the expected number of events from different physics processes and their kinematical distributions. The trigger simulation can be compared to the actual trigger behavior observed using inclusive muon events. Figure 4-3(a) shows the efficiency of the Level 2 trigger requirement of $E_T^{clus} \geq 15$ GeV as a function of the offline jet E_T for multijet trigger simulation and inclusive muon events. The efficiency is defined as the fraction of jets passing the Level 2 trigger E_T^{clus} requirement that also pass a given offline E_T requirement. It can be seen that the trigger simulation overestimates the efficiency for $E_T \leq 25$ GeV. It has been shown [47] that the Level 2 energies are $\sim$ 8% lower than the offline energies. If a Level 2 threshold of 17 GeV is used in the simulation instead of 15 GeV, a better agreement is seen between the inclusive muon sample

and the multijet trigger simulation as shown in figure 4-3(b). The efficiency of the $E_T^{4th-jet} \geq 17$ GeV requirement for the fourth highest trigger cluster as a function of the offline E_T is shown in figure 4-3(c). The trigger efficiency levels out at $\sim 80\%$ for $E_T \geq 25$ GeV. This is because of the overlap between two offline jets mentioned above and their identification as a single trigger cluster.

The efficiency curve for the Level 2 requirement of $\Sigma E_T^{clus} \geq 125$ GeV is shown in figure 4-3(d). This efficiency is the fraction of events passing the $\Sigma E_T^{clus} \geq 125$ GeV requirement in the trigger simulation that pass an offline ΣE_T cut. The trigger is fully efficient for an offline $\Sigma E_T \geq 160$ GeV.

4.2.2 The Trigger Efficiency for different top quark masses

We expect the trigger to become more efficient for an increasing top quark mass, since a heavier top quark implies higher jet transverse energies and a higher total transverse energy in the event. Table 4.2 summarizes the trigger efficiencies for $t\bar{t}$ events as a function of the top quark mass. Trigger efficiencies are calculated by taking the ratio of the number of Monte Carlo $t\bar{t}$ events that pass the trigger to the number generated. The uncertainties quoted are from Monte Carlo statistics only. The systematic uncertainties are neglected.

M_{top} (GeV/c^2)	155	165	175	185	195
ϵ_{trig}%	56.9±0.7	60.4±0.7	63.9±0.5	66.4±0.7	68.7±0.8

Table 4.2: Efficiencies for passing the multijet trigger for different top quark masses.

4.3 The Pre-Selection Sample

Not all the data collected by the CDF detector comes from $p\bar{p}$ interactions. Loss of focussing in the Main Ring causes the CDF detector to be sprayed with particles ("Main Ring Splashes"). Cosmic rays are an ever present background leaving tracks

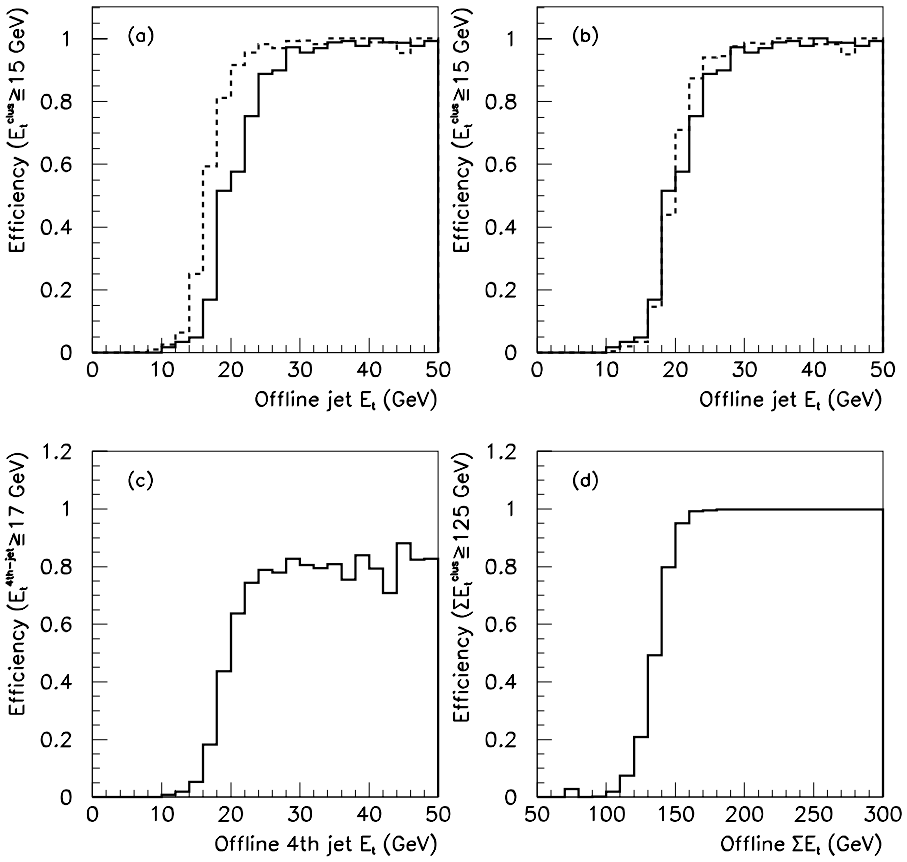

Figure 4-3: *Level 2 trigger efficiencies as a function of offline jet E_T and ΣE_T of the event. Plot (a) shows the Level 2 trigger efficiency for inclusive muon data (solid histogram) and multijet trigger simulation (dashed histogram) for a trigger requirement of $E_T^{clus} \geq 15$ GeV. Plot (b) shows the same for a trigger requirement of $E_T^{clus} \geq 17$ GeV. Plot (c) shows the efficiency as a function of the offline E_T of the fourth hardest jet in an event for a trigger requirement of $E_T^{4th-jet} \geq 17$ GeV. Plot (d) shows the efficiency as a function of the offline ΣE_T of the events for a trigger requirement of $\Sigma E_T^{clus} \geq 125$ GeV.*

and energy in the detector. Moreover, malfunctions in the individual components of the detector give rise to spurious signals or data of poor quality. Therefore, the data passing the trigger is cleaned up to remove the effect of main ring splashes, cosmic rays and detector malfunctions. The requirements are summarized below. Events that pass the cleanup procedure form the *Pre-Selection* sample.

The records of all the data runs are saved in a data-base, and the data runs marked by problems in components of the CDF detector ("bad" data runs) are flagged. During the cleanup procedure, the information on each data run is accessed and events in bad data runs are rejected. There is a total of about 12,000 such events.

Since the center of mass energy is 1.8 TeV, all events with a greater total transverse energy are mainly results of main ring splashes or detector malfunctions. Therefore all events with $\Sigma E_T > 2$ TeV in the calorimeters are rejected.

We require at least one primary vertex with $|z| < 60$ cm in the VTX. Since the $p\bar{p}$ interaction region has a longitudinal spread of about 30 cm, this requirement ensures that there is a $p\bar{p}$ interaction in the central region of the detector. Figure 4-4(a) compares the number of primary vertices for events passing this requirement. The number of vertices in Run 1B data is larger because of a higher average instantaneous luminosity and therefore a higher incidence of multiple $p\bar{p}$ hard scatters.

We also require a missing E_T significance, $S = \frac{\not\!\!E_T}{\sqrt{\Sigma|E_T|}} < 6$. Missing E_T, $\not\!\!E_T$, defined in chapter 3, is the vector sum of the transverse energies of all the calorimeter clusters in the detector. The scalar sum, $\Sigma|E_T|$, is the total transverse energy in the event. S quantifies the resolution of the detector E_T measurement, since the denominator represents the uncertainty in the $\not\!\!E_T$ measurement. In the fully hadronic decay of the top quark, the expected $\not\!\!E_T$ is small. As shown in figure 4-4(b), the distributions of S for Run 1A and 1B data are identical. This requirement removes the effect of Main Ring Splashes and detector malfunctions.

Finally, we require at least four jets (clustered with a cone of 0.4 or 0.7) with an offline $E_T \geq 15$ GeV and $|\eta| \leq 2.4$. Figures 4-4(c) and 4-4(d) compare the number of jets (for cone sizes of 0.7 and 0.4 respectively) in events passing the cleanup requirements. There are events with ≤ 3 jets because the trigger requires at least four

calorimeter clusters *anywhere* in the detector and not just in the $|\eta| \leq 2.4$ region. In addition, as discussed in the section on trigger behavior, the trigger E_T^{clus} requirement is not equivalent to the offline jet E_T requirement. The fraction of events with ≤ 2 jets passing the cleanup requirements is larger in Run 1B data which is primarily due to the higher average instantaneous luminosity in Run 1B. This implies that there are more multiple interactions as discussed above, which result in ≥ 4 jets coming from two or more separate interactions producing ≥ 2 jets each. Some of the primary vertices can be significantly displaced from the nominal interaction point resulting in jets that do not pass the E_T or $|\eta|$ requirement of the cleanup and thereby enhancing the number of events with ≤ 2 jets. An additional effect is from the Level 2 trigger E_T threshold for Run 1A. Because of a lower threshold, fewer jets pass the offline $E_T \geq 15$ GeV requirement resulting in a deficiency in Run 1A compared to Run 1B. The difference between the N_{jet} distributions for cone sizes of 0.4 and 0.7 can be understood by considering that on average 0.4 cone size jets will have a smaller E_T and therefore, in an event fewer jets will pass the offline jet E_T requirement. This will cause the average jet multiplicity to be lower for 0.4 cone size jets.

Table 4.3 summarizes the efficiency for $t\bar{t}$ events to pass all the cleanup requirements (after passing the trigger requirements) for different top quark masses. The efficiency ($\epsilon_{cln}\%$) is the fraction of the number of $t\bar{t}$ Monte Carlo events passing the trigger requirements that also pass the cleanup requirements. The uncertainties quoted are from Monte Carlo statistics only.

M_{top} (GeV/c^2)	155	165	175	185	195
$\epsilon_{cln}\%$	97.0±1.3	96.5±1.3	96.0±0.8	95.4±1.2	95.2±1.2

Table 4.3: The efficiency for passing the cleanup requirements for different top quark masses.

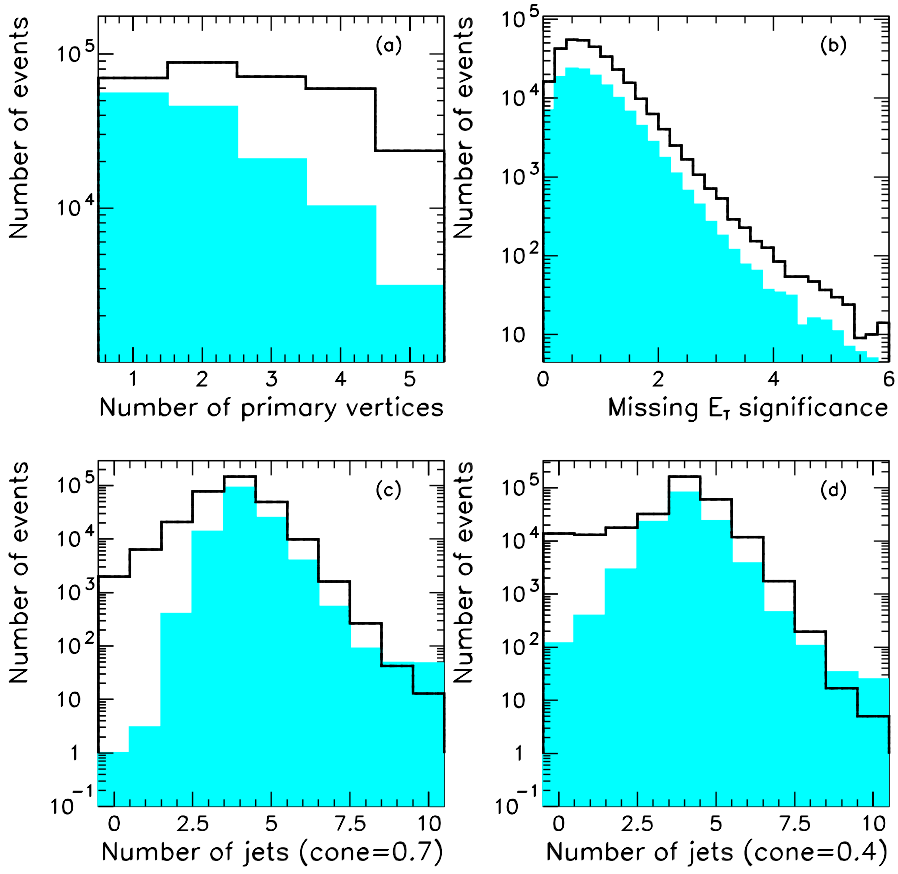

Figure 4-4: *Comparison of Run 1A (shaded) and 1B (white) data after the cleanup requirements. Plot (a) shows the number of primary vertices with* $|z| \leq 60$ *cm. Plot (b) shows the* $\not\!\!E_T$ *significance. Plot (c) shows the number of jets (clustered with a cone of 0.7) with* $E_T \geq 15$ *GeV and* $|\eta| \leq 2.4$*. Plot (d) shows the number of jets (clustered with a cone of 0.4) with* $E_T \geq 15$ *GeV and* $|\eta| \leq 2.4$*.*

4.4 The Selection Sample

For the final sample selection, additional requirements are imposed on the Pre-Selection sample. The additional requirements are summarized below.

- There should be no events with high p_T electron or muon candidates that pass the requirements of the $\ell + jets$ top data samples. This is done to ensure that the multijet data sample is completely orthogonal to the other top quark data samples at CDF. Similarly, jets that are consistent with isolated electrons are rejected. About 95% of inclusive $t\bar{t}$ Monte Carlo events passing the Pre-Selection requirements have no high p_T leptons.

- In order to ensure good calorimetery information, all jets are required to have $|\eta| \leq 2.0$.

- All events are required to have ≥ 4 jets clustered with a cone size of ΔR =0.4. This cone size is chosen to make the analysis compatible with the CDF's $\ell + jets$ top quark analyses, which use a cone size of 0.4. A cone size of ΔR =0.4 has been found to give improved efficiency compared to larger cone sizes for counting jets from Monte Carlo $t\bar{t}$ decays [51].

Events passing the selection requirements comprise the data sample used in this thesis. The efficiencies (ϵ_{sample}) for passing the final sample selection for different jet multiplicities are summarized in table 4.4. These are the efficiencies for $t\bar{t}$ (M_{top} = 175 GeV/c^2) Monte Carlo events to pass all the final sample selection requirements including the trigger and the cleanup. The uncertainties quoted are statistical only.

	$N_{jet} = 4$	$N_{jet} = 5$	$N_{jet} = 6$	$N_{jet} \geq 7$
ϵ_{sample} (%)	17.7±0.2	23.1±0.3	12.6±0.2	3.8±0.1

Table 4.4: Efficiency for passing the final sample selection requirements for $t\bar{t}$ events for a top quark mass of 175 GeV/c^2.

For all events that pass the final sample selection, the jet energies are corrected for different effects in order to reconstruct the total transverse energy of all final the state particles contained within the jet clustering cone of ΔR =0.4. These jet energy corrections are discussed in the next section.

4.5 Jet Energy corrections

The transverse energies and momenta of the jets, as defined in chapter 3, refer only to the energy deposition observed in the calorimeter. These values differ from the true partonic values for a variety of reasons, and therefore need to be corrected. There are four different corrections [48] that are applied to jet energies. They are the Absolute Energy Scale, the Relative Energy Scale, the Underlying Event and the "Out of Cone" corrections. They are described in detail below.

The Absolute Energy Scale corrections compensate for the non-linear response of the calorimeters for hadron showers and electrons or photons. They also compensate for the bending of low momentum particles in the magnetic field such that either they do not reach the calorimeters or fall outside the jet clustering cone. The determination of the response of the calorimeters involves the use of test beam data and the data taken during the normal running of the collider. Since the response of the calorimeter is non-linear, the observed jet energy depends both on the incident parton energies and the momentum spectrum of the particles produced in the fragmentation process. The momentum measurement of the CTC is used to study the fragmentation properties of the particles and the response of the calorimeters to low momentum particles. The ISAJET Monte Carlo generator, using the Field-Feynman[49] parameterization of fragmentation and tuned to the data, is then used to determine the correction factors required to reconstruct the momenta of the original partons.

The Relative Energy Scale corrections compensate for the non-linear response of the calorimeters as a function of η_d. Due to the reduced response of the calorimeters at the boundaries between different detector modules and calorimeter subsystems, the energies of jets are not reconstructed uniformly. In addition, there is also a small

effect from the different response of the different calorimeter systems. In order to correct for these effects, the energies of the jets are calibrated with respect to the energies measured in the central region ($|\eta| = 0.2 - 0.7$) of the detector where the detector response is well understood. To derive these corrections, a sample of events containing two jets is used, where one of the jets is required to lie in the central region of the detector. Since these events are composed of QCD $q\bar{q}, gg \rightarrow q\bar{q}, gg$ production, the transverse energies of the two jets must balance. Using the energies of the jets in the central region, the corrections are derived as a function of η_d.

The Underlying Event Corrections subtract the contribution of the underlying event to the jet energies. These corrections are derived using the data and Monte Carlo models of data described above. In the determination of this correction, the effect of multiple primary interactions is also taken into account. The Out of Cone corrections compensate for the energy falling outside a particular jet clustering cone size. These correction factors are derived using the Monte Carlo described above, and are dependent on the cone size used to cluster the jets.

The corrected p_T of a jet, clustered with a cone-size R, is calculated in terms of its uncorrected p_T, p_T^{raw} via:

$$p_T(R) = p_T^{raw}(R) \cdot c_{rel}(R) \cdot c_{npv} \cdot c_{abs}(R) - U(R) + O(R) \qquad (4.1)$$

Here, $c_{rel}(R)$, c_{npv} and $c_{abs}(R)$ correct for the relative η response of the detector, the effect of multiple interactions and for the absolute energy scale respectively. $U(R)$ takes into account the underlying event and $O(R)$ corrects for the energy loss outside the cone. The relative energy scale corrections ($c_{rel}(R)$) are applied first. Then the effect of multiple interactions (c_{npv}) is taken into account by correcting for $N_v - 1$ primary vertices, where N_v is the number of "good" primary vertices in the event i.e. vertices passing some quality cuts. Absolute energy corrections are then applied followed by underlying event subtraction and out of cone corrections. The underlying event and out of cone corrections are different for Monte Carlo, Run 1A and Run 1B data as summarized in table 4.5 for jets clustered with a cone of 0.4.

Type	Correction (GeV)
U (MC)	0.37
U (Run 1A)	0.72
c_{npv} (Run 1B)	$0.297 \cdot (N_v - 1)$
U (Run 1B)	0.65
O (All)	$1.95 + 0.156 p_T$

Table 4.5: Underlying event and out of cone jet energy corrections for Monte Carlo, Run 1A and Run 1B data. N_v is the number of primary vertices in an event.

4.5.1 Effect of Jet Energy corrections

Figure 4-6 shows the ratio of corrected and uncorrected jet transverse energies as a function of the jet detector pseudo-rapidity (Figure 4-6(a)) and transverse energy (Figure 4-6(b)). The large peaks in figure 4-6(a) correspond to the major detector boundaries, where the calorimeter response is suppressed. The transverse energy distributions of jets before and after the application of the corrections are displayed in Figure 4-6(c). Typically the jet energy corrections increase the jet energy by $\sim 30\%$. The corrected jet energy resolution also depends on the jet E_T and η. For high E_T jets, the resolution function has an rms width of about 10%. These corrections are meant to reproduce the average jet E_T correctly, not to reduce the jet energy fluctuations around this mean E_T.

The uncertainty in the jet energies introduced by these corrections can be probed by using a sub-sample of events containing two jets where most of the energy of one jet is carried by a single γ candidate. A sample of $Z + 1$ jet events can also be used where the Z boson is re-constructed using the $Z \rightarrow e^+e^-$ decay. By balancing the transverse momenta of the photon candidate or the Z boson with the corrected transverse energy of the jet recoiling against it, the fractional energy imbalance is measured to be within 3% of the energy of the photon or the Z. The main sources of uncertainty in the jet E_T due to detector effects are the calorimeter response

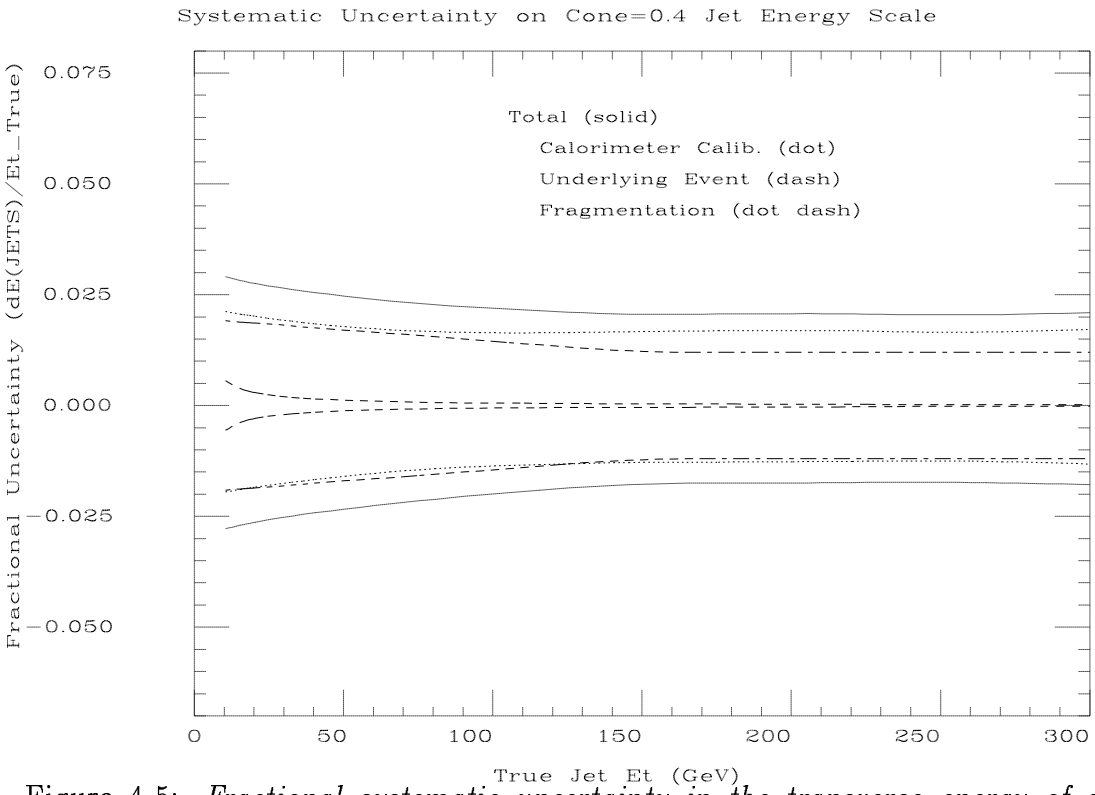

Figure 4-5: *Fractional systematic uncertainty in the transverse energy of a cone ΔR=0.4 jet as a function of the jet transverse energy.*

and time stability of calorimeter energy scales, underlying event correction and jet fragmentation. The systematic uncertainty in the jet energy is presented in figure 4-5 which shows the fractional uncertainty in the jet transverse energy for a $\Delta R = 0.4$ cone size jet as a function of the true jet transverse energy. In addition, there is a theoretical uncertainty in jet energies due to the possibility of large-angle gluon radiation which may not be modeled correctly in perturbative-QCD Monte Carlo programs. The combined uncertainty from all these effects in the jet energy scale is estimated to be $\pm 5\%$[51].

4.6 Effect of multiple interactions

Multiple interactions can give rise to events with high jet multiplicities or produce false displaced secondary vertices. Their effect on displaced vertices is addressed in

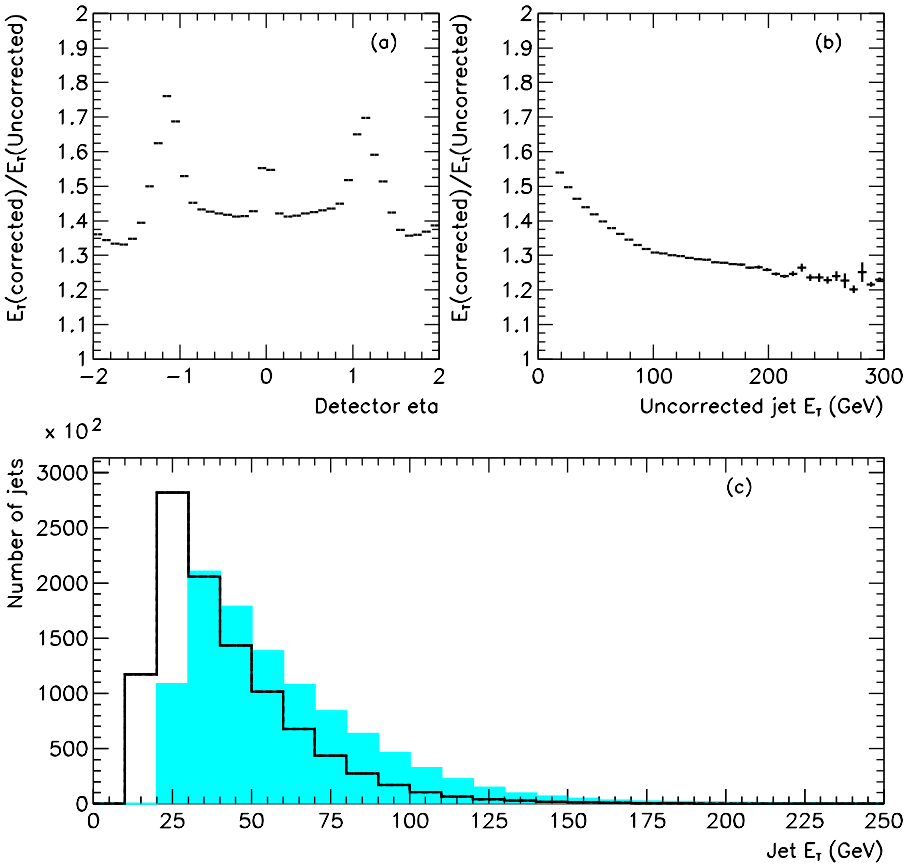

Figure 4-6: *The effect of jet energy corrections: (a) the ratio of corrected and uncorrected transverse energies of jets as a function of the detector pseudorapidity. (b) the ratio of corrected and uncorrected transverse energies of jets as a function of the uncorrected transverse energy. (c) the jet transverse energy distributions without (solid) and with (dashed) corrections.*

	$N_{jet} = 4$	$N_{jet} = 5$	$N_{jet} = 6$	$N_{jet} \geq 7$
Jets (%)	97.2±1.5	96.8±2.7	94.8±6.3	100±20
Events (%)	95.4±2.9	95.3±5.9	88.3±14.7	100±53

Table 4.6: Fraction of jets and events with all jets that are associated to the highest ranking primary vertex.

the next chapter.

The effect of multiple interactions on the number of jets in an event is investigated by determining how often jets within a same event are associated to different primary vertices. This is done as a two-step process. First, for each jet, it is determined which primary vertex it is associated to, and second, the fraction of events with all the jets associated to one primary vertex is calculated.

For the determination of the primary vertex for each jet, a simple algorithm is followed. In order to ensure good tracking information, only those events in the Selection sample are used in which all jets lie within $|\eta| \leq 1$. Tracks are associated to each jet by requiring them to be within $\Delta R \leq 0.4$ of the jet axis. Tracks assigned to each jet are then assigned to a primary vertex determined by the VTX. The vertex with the highest total transverse momentum of tracks attached to it is considered to be the primary vertex the jet originated from. For each event, the n different primary vertices $(V_1, \cdots, V_n)$ are ordered according to the number of jets attached to them, i.e V_1 has the highest number of jets attached to it etc. The number of jets in N-jet events that are attached to each vertex, V_i, is also determined.

In the absence of multiple interactions, an N-jet event will have all N jets associated to V_1, barring resolution effects. Multiple interactions will cause $(N - k)$ jets to be attached to V_1 and k to $V_2, V_3 \cdots$ etc. To take into account the effect of resolution, if other primary vertices are found within 5 cm of V_1, then the jets assigned to them are re-assigned to V_1. The fraction of jets and events with all jets assigned to V_1 is then determined. Table 4.6 summarizes the results for jets and events.

It is seen that about 5% of events with all jets that lie in the central region of the

detector have jets associated to different primary vertices. In the presence of larger sources of uncertainty, the effect of multiple interactions is not considered further in this thesis. The study of multiple interactions in the forward regions is complicated by the lack of reliable tracking information from the CTC and cannot be done in a straight-forward fashion. No studies of multiple interactions in the forward regions have been done so far at CDF.

4.7 Sources of systematic uncertainties

The primary sources of systematic uncertainty in ϵ_{sample} are the Monte Carlo modelling of gluon radiation, the modelling of fragmentation and the uncertainty in the jet energies These uncertainties are discussed individually below:

4.7.1 Radiation Modelling

The amount of initial and final state gluon radiation in $t\bar{t}$ Monte Carlo affects the jet multiplicity of the events. The fractional uncertainty due to this effect, Δ_{rad}, is estimated by comparing the total acceptances for $t\bar{t}$ events using the PYTHIA[38] Monte Carlo with and without initial state radiation. The PYTHIA Monte Carlo is used because it allows the user to control the amount of initial state radiation in a straight forward fashion. The magnitude of the effect is taken to be the semi-difference of the two acceptances. Since, $t\bar{t}$ acceptances are calculated using the HERWIG[37] Monte Carlo, the fractional uncertainty is calculated with respect to the acceptance from HERWIG. The effect of radiation modelling, Δ_{rad}, is determined to be $\pm 8\%$. The effect of radiation modelling is fully correlated across different jet multiplicities i.e. the acceptances for all individual jet multiplicities vary simultaneously by the same fractional amount.

$$\Delta_{rad} = \frac{\epsilon_{tot}^{pythia} - \epsilon_{tot}^{pythia/noisr}}{2\epsilon_{tot}^{herwig}}$$

4.7.2 Fragmentation Modelling

In addition to the modelling of gluon radiation, the modelling of fragmentation of quarks and gluons differs between different Monte Carlo generators. The fractional uncertainty in the acceptance from using different generators, Δ_{frag}, is determined by comparing the total acceptances from PYTHIA and HERWIG. The fractional uncertainty is calculated with respect to the acceptance from HERWIG and determined to be $\pm 6.5\%$. The effect of fragmentation modelling is also fully correlated across different jet multiplicities.

$$\Delta_{frag} = \frac{\epsilon_{tot}^{pythia} - \epsilon_{tot}^{herwig}}{2\epsilon_{tot}^{herwig}}$$

4.7.3 Jet Energy Scale

As mentioned earlier, the uncertainty in the jet energy scale is taken to be $\pm 5\%$. As the jet energy is varied, events shift between different jet multiplicities. This can be seen qualitatively by considering the response of multijet events to varying minimum jet E_T requirements. As the E_T threshold is lowered, more jets will pass the requirement, and events will populate the high jet multiplicity bins. The opposite happens when the E_T requirement is lowered. In this case, fewer jets pass and the events tend to have low jet multiplicities. For an event with a given jet multiplicity, the fractional effect of the uncertainty in the jet energy scale on the efficiency to pass the final sample selection, ϵ_{sample}, is given by:

$$\Delta\epsilon_{sample}^{\pm} = \frac{\epsilon_{sample}^{\pm} - \epsilon_{sample}}{\epsilon_{sample}} \tag{4.2}$$

Here $\epsilon_{sample}^{\pm}$ are the efficiencies after raising or lowering the jet energy scale by 5%. The effect of this uncertainty is summarized in table 4.7 for different jet multiplicities. $\Delta\epsilon_{sample}^{\pm}$ is the effect of $\pm 5\%$ variation in the jet energy scale. The uncertainty due to jet energy scale is also correlated across the different jet multiplicities i.e. changing the energy scale has an effect on all the jet multiplicity bins. To determine the effect of the variation in the jet energy scale by $x\sigma$ ($|x| \leq 1$) on the jet multiplicity distribution, $\Delta\epsilon_{sample}^{\pm}$ can be fit to a linear function, $\Delta\epsilon_{sample}^{\pm} = a_0 + a_1 x$. The values

	$N_{jet} = 4$	$N_{jet} = 5$	$N_{jet} = 6$	$N_{jet} \geq 7$
$\Delta\epsilon^{\pm}_{sample}$ %	$^{+9.1}_{-10.7}$	$^{+0.9}_{-0.7}$	$^{-6.8}_{+5.8}$	$^{-14.5}_{+17.5}$
a_0	-0.799	0.100	-0.499	1.500
a_1	-9.900	-0.800	6.300	16.000

Table 4.7: Effect of the jet energy scale uncertainty on the final sample selection efficiency for different jet multiplicities.

of the coefficients for the different jet multiplicities are summarized in table 4.7 also. This parameterization will be used later in chapter 7 to determine the systematic uncertainty in the $t\bar{t}$ cross-section from jet energy scale.

4.8 Requirement of ≥ 5 jets in an event

The number of events observed in the data is summarized in table 4.8 for different jet multiplicities. The number of expected $t\bar{t}$ events in the Selection sample is also shown. This number is calculated using the CDF measured $t\bar{t}$ production cross-section of $6.8^{+2.1}_{-1.7}$ pb for a top quark mass of 175 GeV/c^2 in the $\ell+jets$ channel and the selection efficiency (ϵ_{sample}) discussed earlier in this chapter. The uncertainty in the number of expected $t\bar{t}$ events is due to the uncertainty in the measured $t\bar{t}$ cross-section and finite Monte Carlo statistics only. Table 4.8 also shows the expected signal over background ratio (S/B). It is seen that without any additional kinematical requirements, the Selection sample is pre-dominantly composed of QCD multijet events. We confirm this by comparing the jet E_T and η distributions for data and QCD Monte Carlo events in figure 4-7. It is seen that the data are described well by QCD Monte Carlo. The discrepancy in the initial two bins results from the trigger simulation not reproducing the behavior of the multijet trigger exactly for jets with low E_T. The expected yield of $t\bar{t}$ in events with 4 jets is negligible. In addition, as shown in figure 4-1, the expected number of $t\bar{t}$ events is the largest for events with five jets. Therefore, in order to improve the signal to background ratio, we require that all events in our

analysis have at least five jets in them.

4.9 Investigation of kinematic variables

In order to reduce the contribution from QCD multijet production different kinematic variables are investigated. Since the identification of b-jets in the event will be required, as described in the next chapter, which in itself is a strong way of reducing background, very many or very tight kinematical requirements are not imposed. The expected $t\bar{t}$ signal is small, and each additional requirement reduces the expected yield.

4.9.1 Corrected ΣE_T

In order to reduce the contribution from QCD multijet production, we use the property of $t\bar{t}$ events that they have a large total transverse energy because of the large top quark mass. Figure 4-8 compares the total transverse energy (ΣE_T) distributions of the data and $t\bar{t}$ Monte Carlo events with ≥ 6 jets. A clear separation is seen between the $t\bar{t}$ and QCD events. For this analysis, which deals with the search for a new decay mode, it is necessary to maximize the significance of the signal, $\frac{S^2}{B}$. Since $S \ll B$, $\frac{S^2}{S+B} \simeq \frac{S^2}{B}$ can be maximized. By using the expected number of $t\bar{t}$ events to set the normalization of S, a requirement of $\Sigma E_T \geq 300$ GeV is chosen as shown in figure 4-8. The requirement is $\sim 83\%$ efficient for $t\bar{t}$ events and $\sim 47\%$ efficient for QCD events for events with ≥ 6 jets. The efficiency for passing the $\Sigma E_T \geq 300$ GeV requirement for data (QCD) and $t\bar{t}$ events is summarized in table 4.9 for different jet multiplicities for a top quark of mass 175 GeV/c^2. The uncertainties quoted are statistical only.

4.9.2 Sphericity and Aplanarity

Jets coming from a $t\bar{t}$ decay are expected to have high E_T and be well separated. In the center of mass frame of the collision, the jets are expected to be uniformly distributed, i.e. top events are expected to be *spherical*. This also implies that the

Events	$N_{jet} = 4$	$N_{jet} = 5$	$N_{jet} = 6$	$N_{jet} = 7$
Observed Run 1A	26321	9877	1993	331
Observed Run 1B	138258	49138	9498	1546
Observed Total	164579	59015	11491	1877
Expected Signal	147±44	192±57	105±31	32±9
Approx. S/B	1/1000	1/300	1/100	1/60

Table 4.8: The number of events observed in data, the number of expected signal events and the expected signal to background ratio for different jet multiplicities for a 175 GeV/c^2 top quark and $\sigma_{t\bar{t}} = 6.8$ pb.

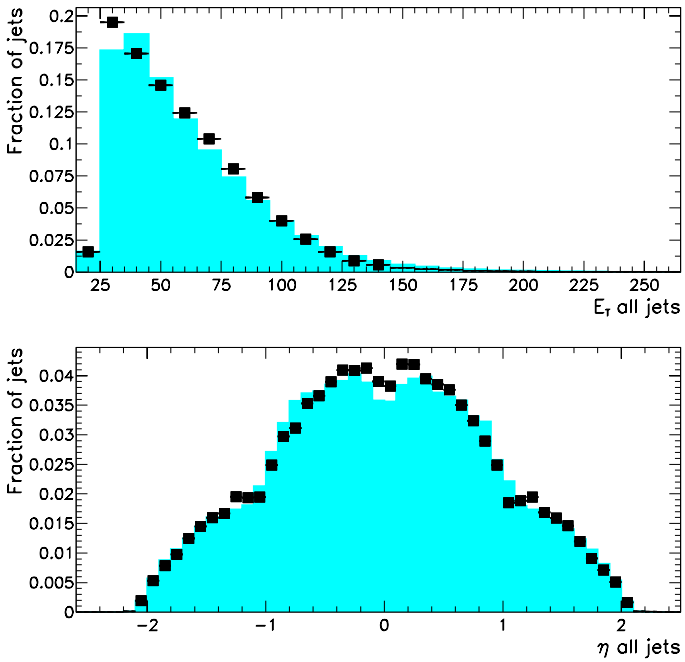

Figure 4-7: *A comparison of jet E_T (upper plot) and η (lower plot) distributions for data (histogram) and QCD Monte Carlo (squares).*

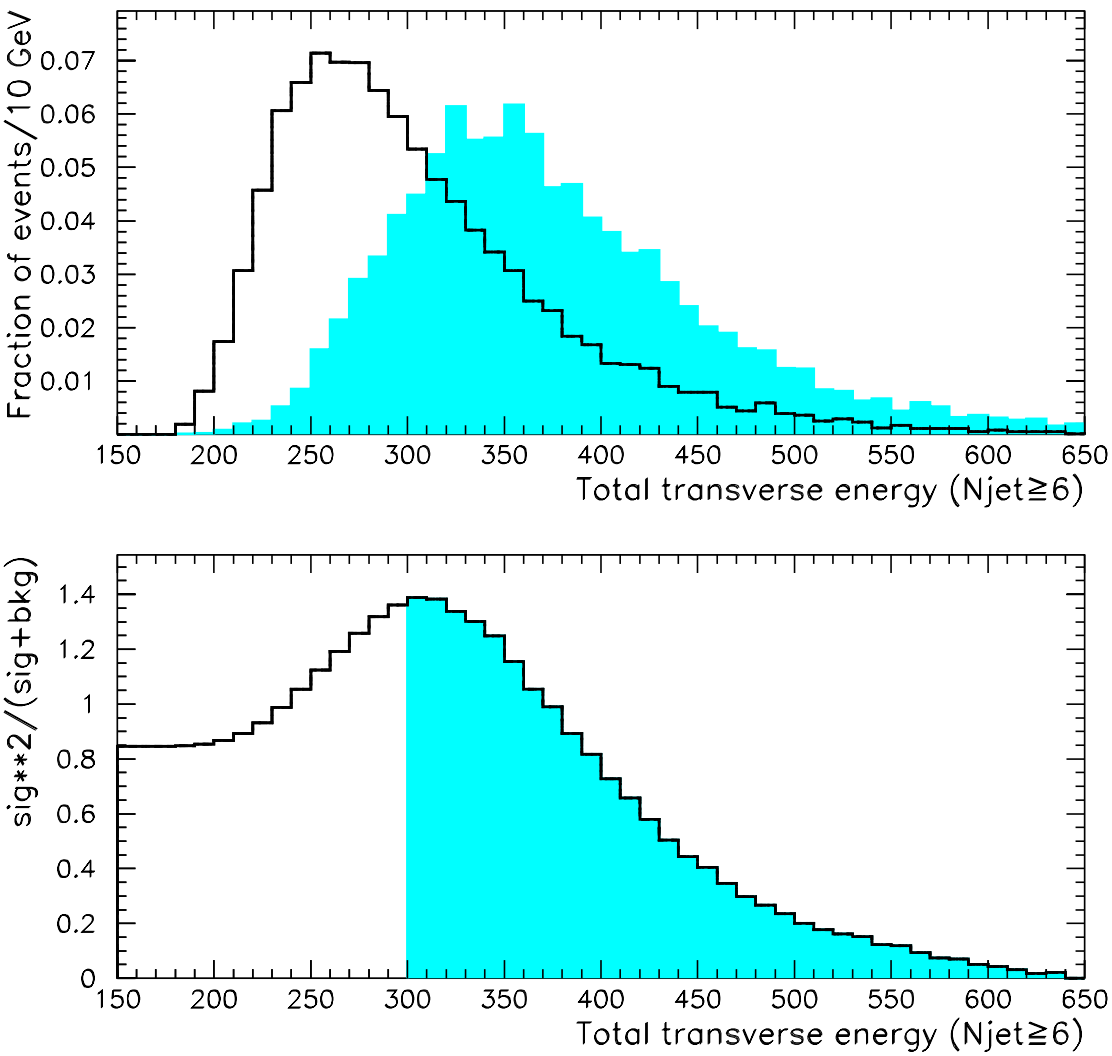

Figure 4-8: *The top figure shows the ΣE_T distribution of $\geq$ 6 jet events for data (white) and $t\bar{t}$ (shaded) events. Both distributions have been normalized to unit area. The bottom figure shows the selection of $\Sigma E_T \geq 300$ GeV requirement by maximizing* $\frac{S^2}{S+B}$.

	$N_{jet} = 4$	$N_{jet} = 5$	$N_{jet} = 6$	$N_{jet} = 7$
$\epsilon^{t\bar{t}}_{\Sigma E_T}$ (%)	30.0±0.77	57.3±1.0	79.6±1.8	93.2±3.6
$\epsilon^{QCD}_{\Sigma E_T}$ (%)	14.7±0.10	26.6±0.20	43.7±0.7	66.1±2.4

Table 4.9: Efficiencies for passing the ΣE_T requirement for different jet multiplicities for a top quark of mass 175 GeV/c^2 and for QCD multijet production.

jets will tend not to lie in the same plane, and therefore will be *aplanar*. These topological properties of top events can be quantified by defining the momentum tensor, $M_{ab} = \Sigma_i P_{ia} P_{ib}$ where $a, b = 1, 2, 3$ are the components of the momentum vector $\mathbf{P}$ and i is the jet index that is summed over. The three normalized and ordered eigenvalues of the tensor, $\lambda_1 \leq \lambda_2 \leq \lambda_3$, are used to define the sphericity, S, and the aplanarity, A, of the event in the center of mass frame of the collision:

$$S = \frac{3}{2}(\lambda_1 + \lambda_2); \quad A = \frac{3}{2}\lambda_1$$

Figure 4-9 shows the sphericity, aplanarity and sphericity versus aplanarity distributions for events with at least six jets in the data and the $t\bar{t}$ Monte Carlo. The top events are more spherical and aplanar. By maximizing $\frac{S^2}{S+B}$, requirements can be selected on S and A for events with ≥ 6 jets. A requirement of $S \geq 0.275$ is $\sim 89\%$ efficient for $t\bar{t}$ events and $\sim 71\%$ efficient for QCD events. For aplanarity, a requirement of $A \geq 0.05$ is $\sim 83\%$ efficient for $t\bar{t}$ events and $\sim 58\%$ efficient for QCD events. The sphericity and aplanarity of multijet events are not as efficient as the total transverse energy in rejecting the QCD background and therefore will not be used to discriminate between QCD and $t\bar{t}$.

4.9.3 Jet E_T

Figure 4-10 shows the corrected E_T distributions of the four hardest jets, both for data and for $t\bar{t}$ Monte Carlo. Leading jets from top are expected to have higher energies than generic jets from QCD processes. As shown in the figure, jet E_T for the leading jet does not provide a strong differentiation between the background and

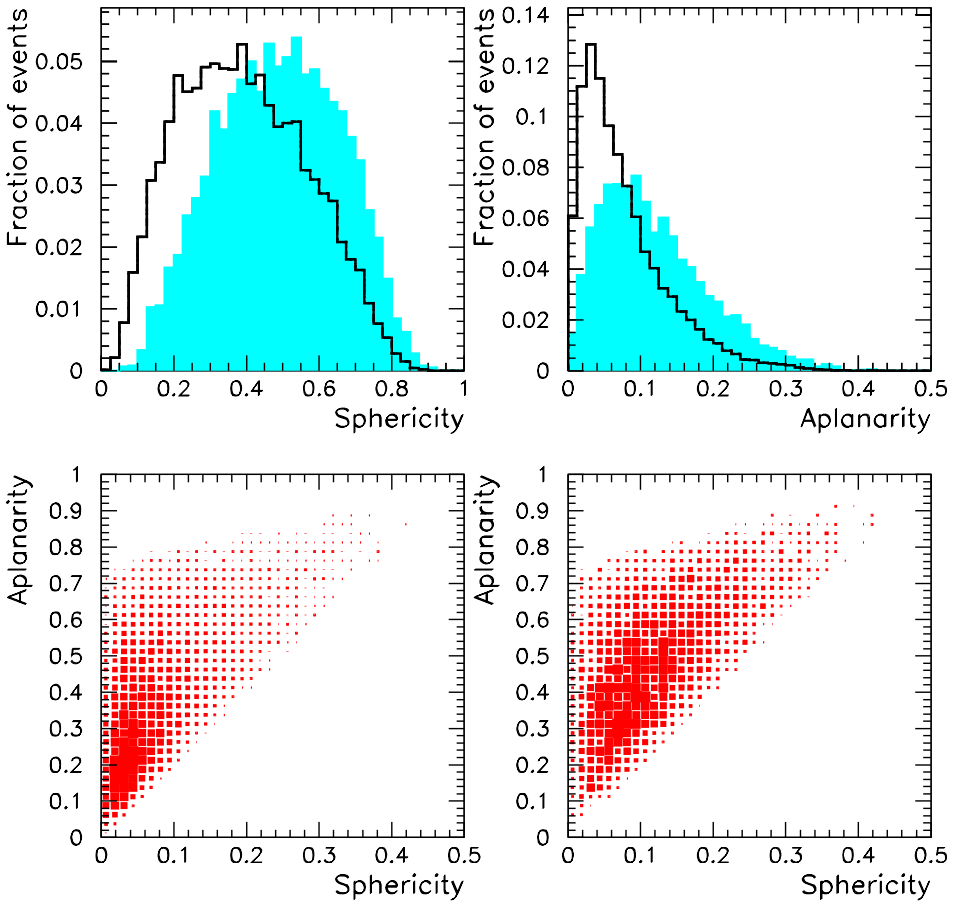

Figure 4-9: *A comparison of the sphericity and aplanarity distributions in data (white) and $t\bar{t}$ Monte Carlo (shaded). (a) shows the sphericity and (b) the aplanarity. (c) shows sphericity versus aplanarity for data and (d) for $t\bar{t}$ Monte Carlo.*

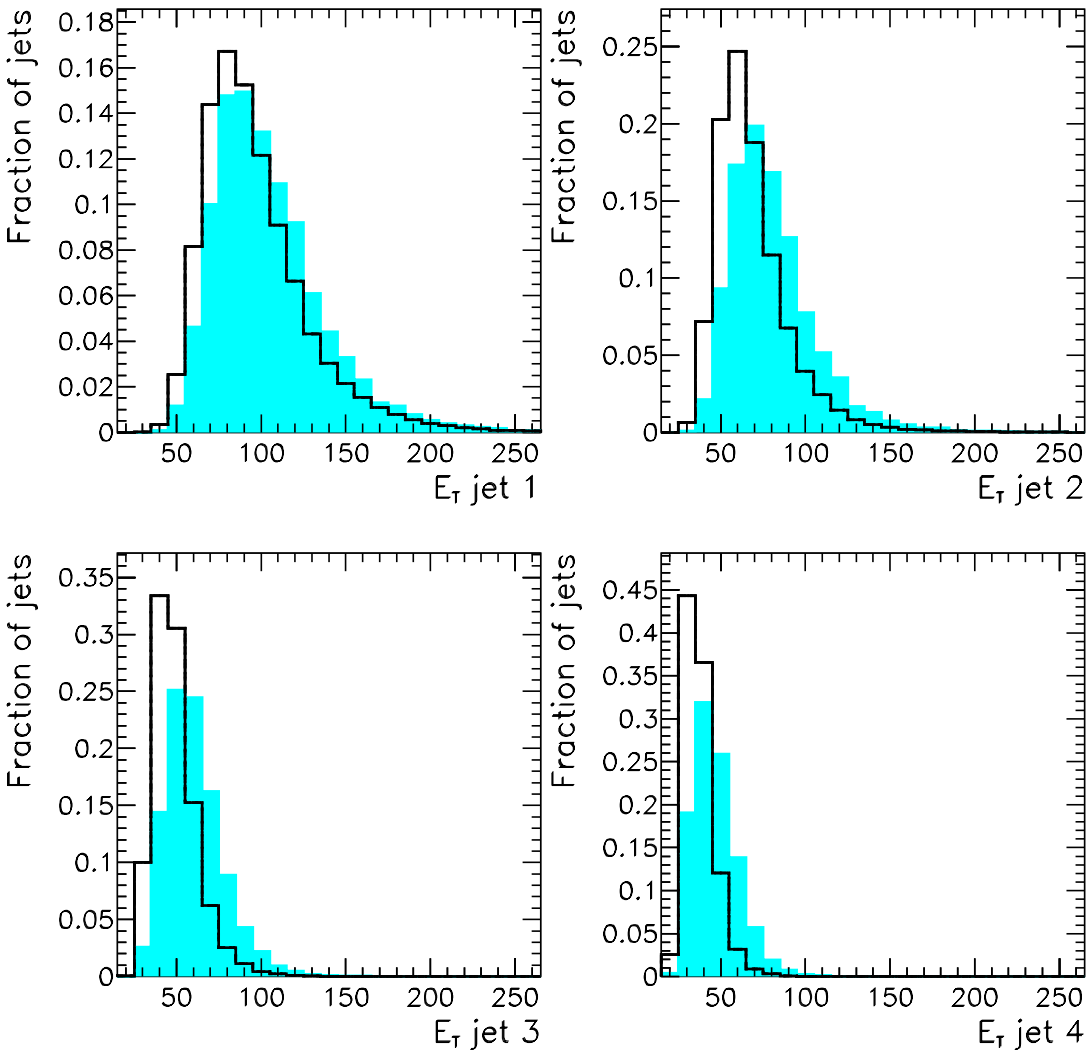

Figure 4-10: *A comparison of jet E_T's for the four highest E_T jets in the event, for data (white) and $t\bar{t}$ Monte Carlo (shaded). The jets are ordered in decreasing E_T i.e. jet 1 is the highest E_T jet in the event.*

the signal, without being inefficient for top. There is a more marked separation for the second, third and fourth leading jet, however it is not strong. E_T distributions for jets are also correlated, so imposing a requirement on the E_T of the highest jet, for example, will change the E_T distribution of the second highest jet. It is seen that a requirement on the E_T of the jets is not a strong discriminant.

4.9.4 Summary of the kinematical requirements

The $\Sigma E_T \geq 300$ GeV requirement is the most efficient in removing QCD multijet production and retaining $t\bar{t}$ of the three requirements discussed above. After requiring $\Sigma E_T \geq 300$ GeV, the signal to background ratio improves, as summarized in table 4.10, which shows the number of data events passing the ΣE_T cut, the expected number of signal events and the expected signal to background ratio. The uncertainties in the number of expected signal events are due to the uncertainty in the measured $t\bar{t}$ cross-section and finite Monte Carlo statistics.

Events	$N_{jet} = 4$	$N_{jet} = 5$	$N_{jet} = 6$	$N_{jet} = 7$
Observed Run 1A	3672	2605	898	231
Observed Run 1B	20489	13114	4139	1012
Observed Total	24161	15719	5037	1243
Expected Signal	44±13	110±33	83±25	30±9
Approx. S/B	1/550	1/140	1/60	1/40

Table 4.10: The number of events observed in data, the number of expected signal events and the expected signal to background ratio for different jet multiplicities for a 175 GeV/c^2 top quark and $\sigma_{t\bar{t}} = 6.8$ pb after the application of the ΣE_T requirement.

Even after the application of the ΣE_T requirement, there is a large contribution from gluon and light quark QCD multijet production. In the next chapter the identification of b quark jets (from $t\bar{t}$ decay) is discussed and required as an additional requirement to lower the QCD background contribution.

Chapter 5

Identification of b quark jets

We have seen in chapter 4 that events with a total transverse energy greater than 300 GeV are dominated by QCD multijet production and most of the jets present in these events are from light quarks (u,d or s) or gluons. Since the presence of b quarks in the final state is a characteristic of $t\bar{t}$ decays, we can reduce the contribution from QCD multijet production by requiring that events have jets from b quarks in them. The identification of jets from b quarks is called "b-tagging".

The average p_T ($\sim$ 40 GeV) of b quark hadrons produced in $t\bar{t}$ decay is large compared to the mass of the b quark. Moreover, due to the small magnitude of the CKM matrix elements $|V_{ub}|$ and $|V_{cb}|$, b quark hadrons have long lifetimes ($c\tau \approx$ 450 μm [6]). This implies that they travel a significant distance ($\sim 3-4$ mm) before they decay. In addition, upon decay, they produce multi-particle final states. Therefore, the characteristic signature of b quark decay is a "secondary" vertex that is displaced from the primary event vertex and has two or more tracks with large impact parameters associated to it. The b-tagging technique used in this analysis, Secondary Vertex Tagging, searches for such decay vertices.

Not all b-tagged jets are from b quark decays. The c quark hadrons also have a long lifetime ($c\tau \approx 150-300$ μm [6]) and decay into multi-particle final states. Displaced vertices arising from c quark decays can therefore also be identified, although with a lower efficiency (a factor of $\sim \frac{1}{3}$ [32]) because of their smaller lifetime and track multiplicity. The decay of b quarks also produces c quarks, which in turn can produce

secondary vertices. Therefore, in practice, the identified b quark secondary vertices also contain a contribution from c quark decays. In addition, light quark or gluon jets may also be tagged. Such "fake" tags or "mistags" are the result of detector resolution, tracking inefficiencies and mistakes of the b-tagging algorithm. Such tags constitute the instrumental background to our b-tagging.

In this chapter, we use b-tagging to reduce the contribution from QCD multijet production. By studying events observed in the data which contain one b-tagged jet, we conclude that they are consistent with non-$t\bar{t}$ production of b and c (*heavy flavor*) quarks. We determine the efficiency for identifying b quark jets in $t\bar{t}$ decays using a Monte Carlo, and calculate the expected number of signal events. By maximizing the expected signal to background ratio, we select events with ≥ 2 b-tagged jets as our final sample.

5.1 Secondary Vertex Tagging

At CDF, the excellent position resolution of the SVX is used to identify the displaced secondary b decay vertices. Obviously, the ability to identify the displaced tracks associated to such vertices depends on the resolution for determining the trajectory of each track and the primary vertex of the event. The determination of the primary event vertex has already been described in chapter 3. Depending on the number of tracks and the event topology, the uncertainty in the fitted primary-vertex coordinates transverse to the beam direction ranges from 6 to 36 μm. The b-tagging algorithm requires the size of the impact parameter, d_0, of a track to be large compared to its estimated uncertainty. The sign of the impact parameter is given by the location of the beam in the transverse plane, relative to the circle which describes the track trajectory in the transverse plane. For positively charged tracks, the CDF convention is to assign a negative sign to d_0 when the location of the beam lies inside the circle, and a positive sign to d_0 when it is outside. This convention is reversed for negatively charged tracks. Tracks from heavy flavor decay will populate both the positive and negative tails of the impact parameter distribution. The uncertainty on d_0, σ_{d_0}, is

computed for each track with the measured momentum and multiple scattering based on the traversed material. It ranges from 50 μm for 1 GeV/c charged tracks to 15 μm for 10 GeV/c tracks. A check of the calculation of σ_{d_0} is given in [51].

Tracks arising from the decay of heavy flavor quarks are expected to have large impact parameters, and the non-heavy flavor *prompt* tracks are expected to extrapolate back to the primary vertex. However, detector resolution and tracking inefficiencies result in prompt tracks with large impact parameters.

5.1.1 b-tagging algorithm

The b-tagging algorithm is applied to SVX tracks with large impact parameter significance ($d_0/\sigma_{d_0} > 2.5$) which are associated to "taggable" jets. A jet is defined to be taggable if it has $E_T \geq 15$ GeV, $|\eta| \leq 2$ and at least two SVX tracks passing certain track quality requirements. The tracks are associated to a jet if they lie within a cone of $\Delta R = 0.4$ of the jet axis. In order to remove tracks consistent with photon conversions ($\gamma \rightarrow e^+e^-$) and decays of K_s mesons or Λ baryons originating from the primary vertex, a maxmimum impact parameter requirement is imposed. In addition, track pairs consistent with the K_s or Λ mass are also removed. These requirements are imposed because K_s and Λ decays also produce displaced secondary vertices ($c\tau(K_s) = 2.7$cm and $c\tau(\Lambda) = 7.9$cm [6]).

An attempt is made to vertex ≥ 3 SVX tracks using a 3-dimensional constrained fit (Pass 1). If no secondary vertex is found then track quality requirements are tightened and ≥ 2 tracks are used in the fit (Pass 2). If a secondary vertex is found in Pass 1 or 2, the jet is flagged as b-tagged. The details of the Secondary Vertex Tagging algorithm and the requirements for Pass 1 and Pass 2 are given in Appendix A.

The SVX detector provides information only in the $r - \phi$ plane. Therefore, the tracks are used to calculate a two dimensional transverse decay length of the secondary vertex, L_{xy}, and its uncertainty, $\sigma_{L_{xy}}$. If (x_p, y_p, z_p) and (x_s, y_s, z_s) are the co-ordinates of the primary and secondary vertices respectively, then L_{xy} is the signed magnitude of the vector $\vec{L}$ in the transverse $(r - \phi)$ plane. The unit vector pointing along the

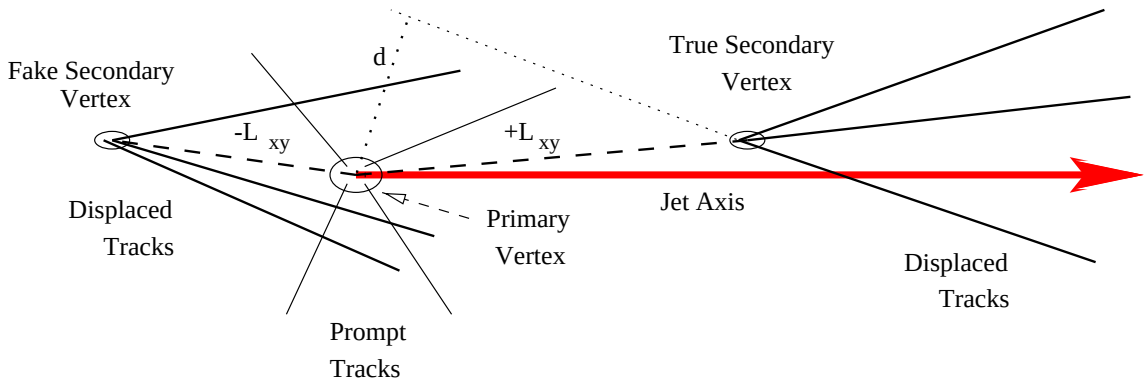

Figure 5-1: *A schematic view in the $r-\phi$ plane showing a real and a fake displaced secondary vertex (mistag). The bold arrow denotes the direction of the jet axis.*

axis of the jet is denoted by $\hat{n}$.

$$L_{xy} = \vec{L} \cdot \hat{n}; \quad \vec{L} = (x_s - x_p)\hat{i} + (y_s - y_p)\hat{j}$$

Figure 5-1 shows a view of the primary and secondary vertices in the transverse plane. In order for a jet to be tagged, the secondary vertex is required to have a two dimensional decay length significance of $|L_{xy}|/\sigma_{L_{xy}} \geq 3$. The typical value of $\sigma_{L_{xy}}$ is $\sim 130\mu$m, which is much smaller than the distance travelled by b quark hadrons. This results in a clean identification of displaced secondary vertices.

While the secondary vertices from heavy flavor quark decays are expected to have an L_{xy} distribution with a positive sign, the L_{xy} distribution of mistags is expected to be symmetric about zero. Accordingly, jets containing candidate secondary vertices with positive (negative) L_{xy} are termed as positive (negative) tagged jets.

Resolution effects also imply that even for heavy flavor quark decays, the L_{xy} distribution will have a small negative component, typically of the order of a few percent of the positive component [32].

This algorithm was developed for the discovery of the top quark in the $\ell + jets$ channel at CDF [3, 51]. The optimization of the algorithm, to maximize the efficiency for identifying heavy flavor jets while minimizing the contributions from mistags is described elsewhere [32].

To confirm that the b-tagging algorithm identifies b quarks, a large inclusive elec-

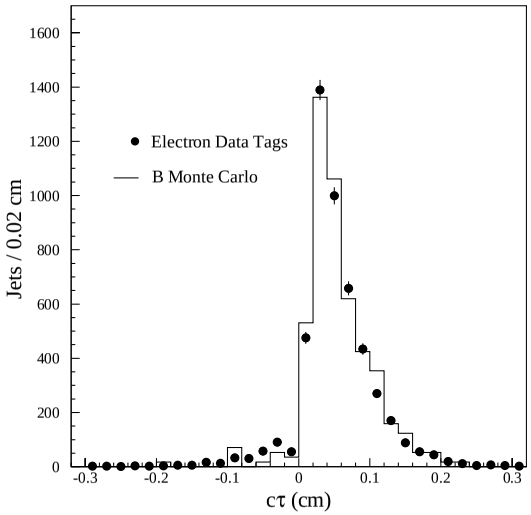

Figure 5-2: *The $c\tau_{\rm eff}$ distribution for jets with a secondary vertex in the inclusive electron data (points with error bars) compared to Monte Carlo simulation (histogram) with the world average B lifetime.*

tron sample (i.e. events with an electron and anything else) is used [51]. This sample, selected by requiring an electron with $|\eta| < 1.0$ and $p_T \geq 10$ GeV/c, is rich in $b\bar{b}$ events, where the semi-leptonic (i.e. $b \rightarrow cl\nu$) decay of the b quarks results in the electron in the event. To verify that the b-tagged jets associated with the electrons include a high percentage of b quark jets, the decay length of the secondary vertex associated to the jet is converted into an estimate of the effective proper decay length, $c\tau_{eff}$, using the expression [50]:

$$c\tau_{eff} = L_{xy}\frac{M}{p_T f}$$

Here M is the invariant mass of the tracks associated to the secondary vertex, p_T is their total vector transverse momentum, and f is a scale factor determined from a Monte Carlo of b decays, which accounts for b-hadron decay products that are not attached to the secondary vertex. This simulated sample was made using the HERWIG[37] event generator and the standard CDF detector simulation.

The $c\tau_{eff}$ distribution for the electron data is shown as the points in figure 5-2, and the $c\tau_{eff}$ distribution for jets in the Monte Carlo sample is shown as the solid

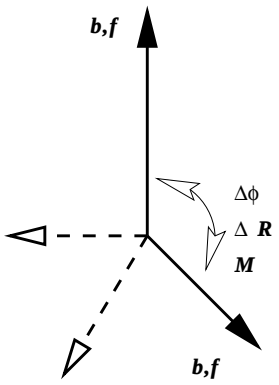

Figure 5-3: *Definition of a double tagged combination. A four jet event is shown with two tagged jets (solid). A double tagged combination is a distinct jet pair with both jets tagged. The tagged jets can be heavy flavor jets (b) or mistags (f). Given two tagged jets, their separation in azimuth ($\Delta\phi$), separation in $\eta - \phi$ space (ΔR) and their invariant mass (M) can be calculated.*

histogram. The data agree well with the Monte Carlo simulation of b decay which uses the world average b-hadron lifetime[6]. More details can be found elsewhere [51].

The yields of events with b-tagged jets in the data are summarized in tables 5.1 and 5.2 for different jet multiplicities before and after the $\Sigma E_T \geq 300$ GeV requirement. Here "N SVX +" means events that have N positive tags in them regardless of the number of negative tags. "N SVX $-$" is similarly defined.

We also count the number of distinct tagged jet pairs or *double tagged combinations* in each event. Figure 5-3 illustrates the defintion of a double tagged combination. In events with N tags ($N \geq 2$), there are $\frac{N(N-1)}{2}$ double tagged combinations. Given two tagged jets, their separation in azimuth ($\Delta\phi_{jj}$), their separation in $\eta - \phi$ space (ΔR_{jj}) and their invariant mass (M_{jj}) can be calculated. In chapter 7, we will make use of these topological variables. Double tagged combinations can be *real* or *fake*. Real double tagged combinations have both jets tagged positively. Fake double tagged combinations have at least one mistagged jet.

In the absence of heavy flavor production, the number of events with positive and negative tags should be the same. However, a clear excess of positive tags over negative tags is a proof that we are tagging heavy flavor jets.

All ΣE_T	$N_{jet} = 4$	$N_{jet} = 5$	$N_{jet} = 6$	$N_{jet} \geq 7$
Total	164579	59015	11491	1877
1 SVX +	7683	3270	778	123
2 SVX +	606	275	71	17
3 SVX +	12	9	8	1
4 SVX +	2	2	0	0
1 SVX −	1945	920	225	36
2 SVX −	17	5	0	0

Table 5.1: Summary of the number of positively and negatively tagged events seen in Run 1A and 1B data before the $\Sigma E_T \geq 300$ GeV requirement.

$\Sigma E_T \geq 300$ GeV	$N_{jet} = 4$	$N_{jet} = 5$	$N_{jet} = 6$	$N_{jet} \geq 7$
Total	24161	15719	5037	1243
1 SVX +	1313	978	366	81
2 SVX +	91	100	38	13
3 SVX +	3	1	4	0
4 SVX +	1	1	0	0
1 SVX −	394	315	116	26
2 SVX −	3	2	0	0

Table 5.2: Summary of the number of positively and negatively tagged events seen in Run 1A and 1B data after the $\Sigma E_T \geq 300$ GeV requirement.

5.2 Tagged events in the multijet sample

As described in chapter 4, events with five or more jets comprise the $t\bar{t}$ signal sample. We now need to determine if the number of b-tagged events observed in our signal sample is consistent with the number of expected events from non-$t\bar{t}$ (background) sources. We do this by comparing the heavy flavor content of our signal sample with that of a background sample where the expected contribution from $t\bar{t}$ decays is small. If the heavy flavor content of the signal sample is significantly higher, then it indicates the presence of new sources of heavy flavor that are not present in the background sample. For this analysis, the background sample consists of events with four jets.

The two main sources of positively tagged jets in the 4-jet events are heavy flavor decays and mistags. We measure the probability for b-tagging a taggable jet or a "positive tagging rate" in 4-jet events as a function of several relevant variables. This tagging rate is then applied to all the taggable jets in our signal sample to get an estimate of the number of expected positively tagged jets from non-$t\bar{t}$ heavy flavor production and mistags. This method requires no a priori knowledge of the tagging rates of jets or the heavy flavor content of the background sample. A $t\bar{t}$ signal would manifest itself as an excess of b-tagged jets in the signal sample.

The negatively tagged jets are dominated by mistags. Applying "negative tagging rates" measured in the 4-jet events to the taggable jets in our signal sample allows us to test if the number of negatively tagged jets observed in the signal sample is consistent with mistags.

A similar method was used in the search for the top quark in the $\ell + jets$ channel. A sample of "generic" jets (i.e. events with at least one jet passing a minimum trigger transverse energy requirement) was taken to be a background sample to the $W + jets$ events used in the analysis. Assuming that the heavy flavor content of the generic jets sample is at least as large as the $W + jets$ sample, an upper limit for the sum of heavy flavor and mistag backgrounds in the $W + jets$ sample was calculated [51].

5.2.1 Tagging rate of jets

The ability to reconstruct a secondary vertex in a jet depends on the jet energy and the number of SVX tracks in the jet. Due to these dependencies, the b-tagging rates are parametrized in terms of the number of SVX tracks (N_{SVX}) and the transverse energy (E_T) of jets. In addition, as discussed later in this chapter, a slight dependence of the tagging rates is also seen on the total transverse energy (ΣE_T) of the event, and is included in our parameterization.

The positive (negative) tagging rate of jets (R) is defined as the number of positive (negative) tagged jets, N_{tag}, divided by the number of taggable jets, N_{able}. The tagging rates, when parametrized in terms of N_{SVX}, E_T and ΣE_T are determined using a finite bin size for these parameters. Therefore, the tagging rate of jets, for i^{th} bin in N_{SVX}, j^{th} bin in E_T and k^{th} in ΣE_T is given by:

$$R(i,j,k) = \frac{N_{tag}(i,j,k)}{N_{able}(i,j,k)}$$

The positive and negative tagging rates, R^+ and R^-, in multijet events as a function of uncorrected jet E_T are shown in figure 5-4 before and after the requirement of $\Sigma E_T \geq 300$ GeV. The positive (negative) tagging rates increase with jet E_T and are constant at $\approx$ 3% ($\approx$ 0.8%) for jets with $E_T \geq 50$ GeV. The fact that the positive tagging rates are higher than the negative rates is again indicative that we are tagging of heavy flavor jets. It is also seen that the ΣE_T requirement does not alter the observed tagging rates.

For reference, tagging rates seen in the generic jets sample are also shown. It is seen that the tagging rates are different in the multijet and generic jets sample. The difference is due to the different trigger requirements of the two data samples. Figure 5-4 also shows the positive and negative tagging rate dependence on the number of SVX tracks in a jet. Again, the positive tagging rates are about 4 times higher than the negative tagging rates. The tagging rates are also seen to be unaffected by the $\Sigma E_T \geq 300$ GeV requirement.

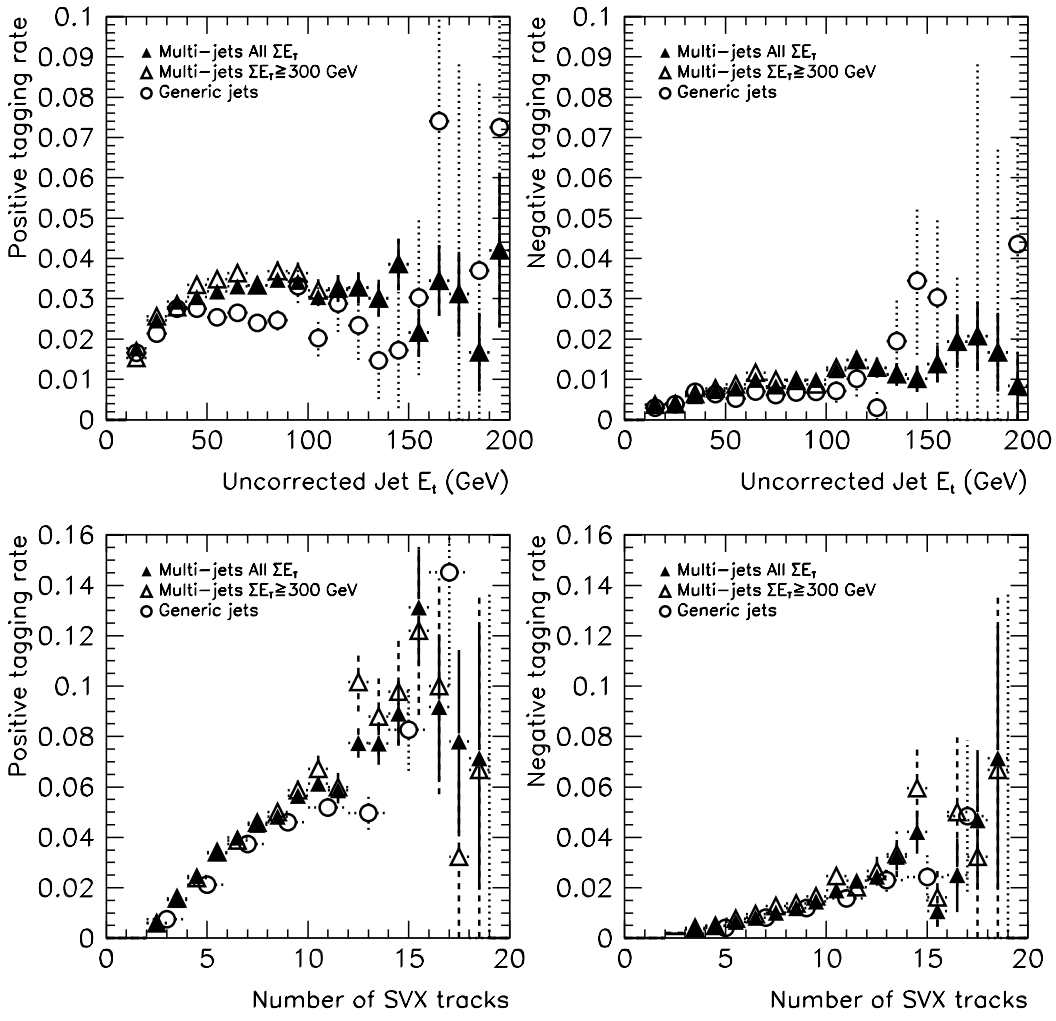

Figure 5-4: *The positive (left) and negative (right) tagging rates as a function of the uncorrected E_T and the number of tracks in a jet. Three sets of points are shown, filled triangles for all the 4-jet events, open triangles for 4-jet events passing the $\Sigma E_T \geq 300$ GeV requirement and circles for generic jet events.*

Dependence on ΣE_T

The rate for observing ≥ 1 b-tags in an event is shown as a function of the total transverse energy of the event in figure 5-5. A clear dependence on ΣE_T is seen. However, this dependence is misleading because of the inherent E_T dependence of tagging rates. To check the dependence of the tagging rates on ΣE_T alone, the E_T dependence must be taken into account. We assign, to each taggable jet, a weight proportional to $1/R^{\pm}(E_T, N_{SVX})$, where $R^{\pm}(E_T, N_{SVX})$ is the positive or negative tagging rate for a jet with transverse energy E_T and N_{SVX} tracks irrespective of the ΣE_T of the event. A weak dependence on the ΣE_T of the event after the weighting procedure is seen for both positively and negatively tagged events as shown in figure 5-5.

Dependence on Instantaneous Luminosity

As discussed in chapter 4, high instantaneous luminosity results in a higher incidence of multiple primary interactions which can affect b-tagging in two ways. First, the number of taggable jets in an event can be increased, and second, tracks from a jet can be mis-associated to another jet from a *different* primary vertex. Such tracks can have large impact parameters and can therefore result in fake displaced secondary vertices. These two effects may not be accounted for properly by the 4-jet tagging rates because multiple interactions may influence different jet multiplicities differently. Therefore, we explicitly check the dependence of tagging rates on the instantaneous luminosity ($\mathcal{L}$). Figure 5-6 shows the positive and negative tagging rate of jets as a function of $\mathcal{L}$. No dependence is seen for positive tagging rates. There is a slight dependence for negatively tagged jets, coming from 4-jet events primarily. It is seen, however, that higher jet multiplicities do not exhibit any dependence of negative tagging rate on $\mathcal{L}$. Therefore, the effect of multiple interactions on tagging rates is taken to be negligible.

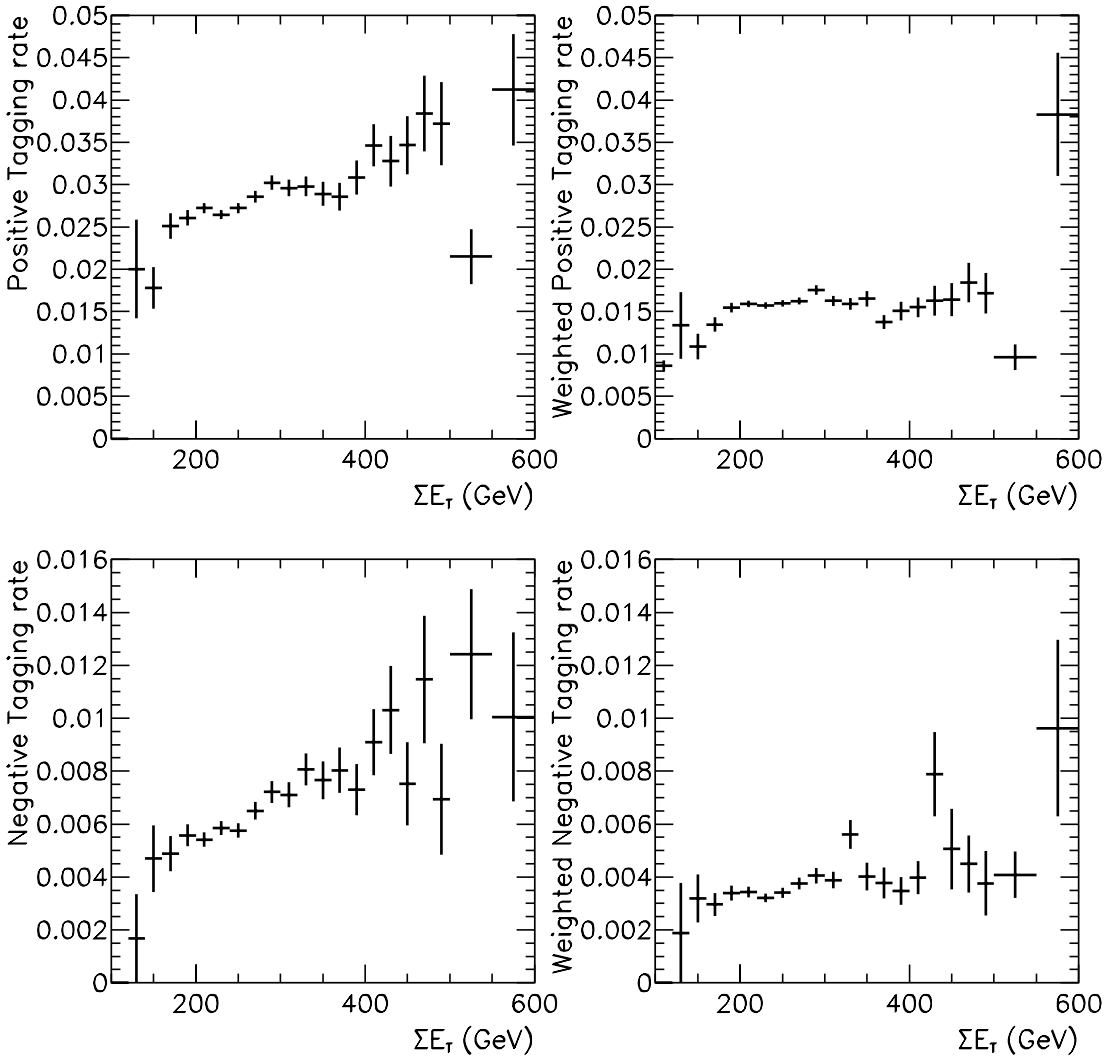

Figure 5-5: *Tagging rate dependence on the ΣE_T of the events before and after the weighting procedure.*

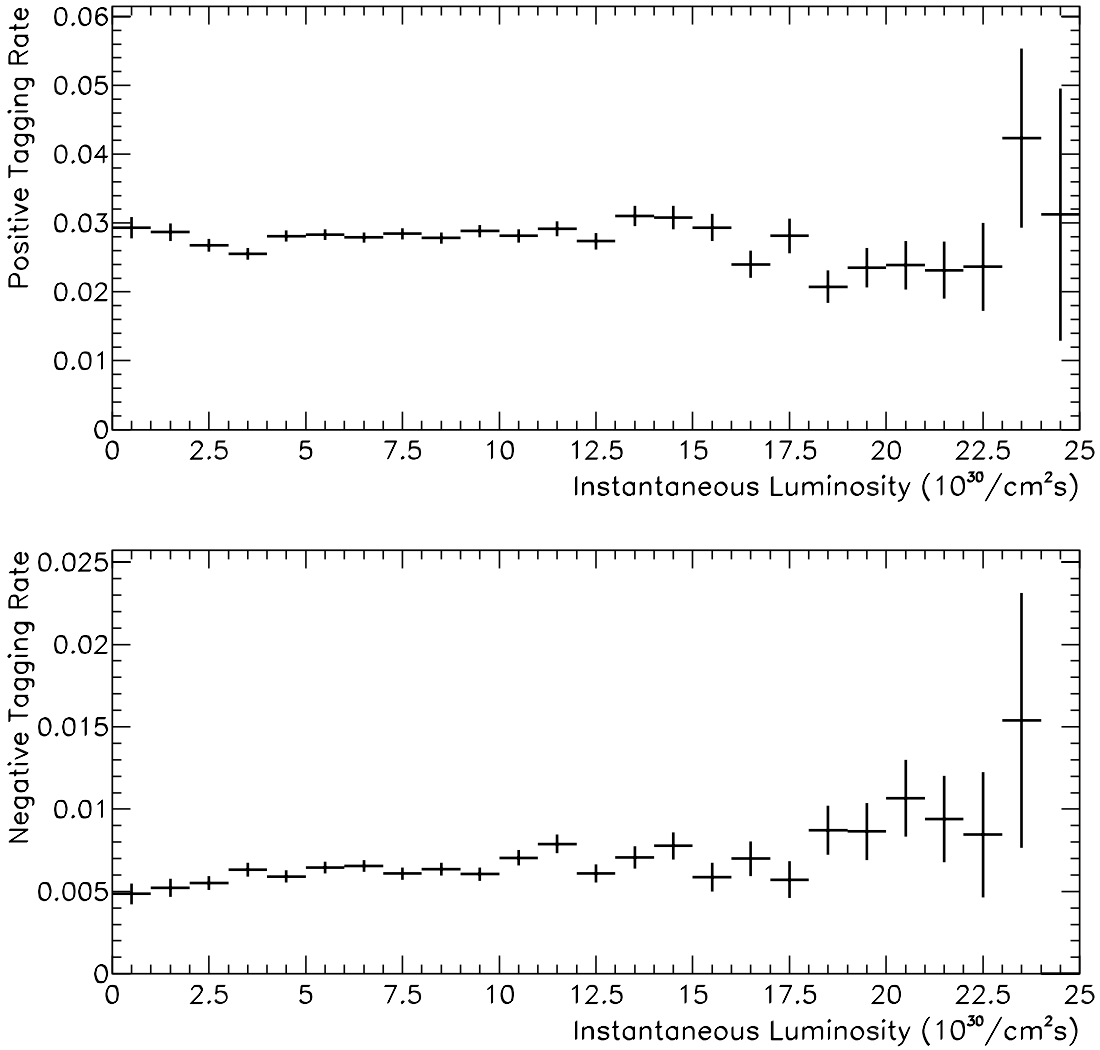

Figure 5-6: *Positive and negative tagging rates as a function of instantaneous luminosity.*

5.2.2 Calculation and Application of tagging rate matrices

Tagging rate matrices, R_{ijk} ($\equiv r(i,j,k)$), for positive (negative) tagged jets can be used to predict the number of positive (negative) tags expected from a data sample, and their distributions.

Consider first the sample used to calculate the tagging rates (i.e. the 4-jet events). We introduce the following notation: R_{ijk} is the tagging rate for jets which are in the i^{th} E_T bin, j^{th} N_{SVX} bin and k^{th} ΣE_T bin, T_{ijk} is the number of tagged jets in that bin and U_{ijk} is the number of untagged taggable jets in that bin. The tagging rate R_{ijk} is therefore given by:

$$R_{ijk} = \frac{T_{ijk}}{T_{ijk} + U_{ijk}}$$

The statistical uncertainty in R_{ijk}, ΔR_{ijk} is given (using binomial statistics) by:

$$\Delta R_{ijk} = R_{ijk}\sqrt{\frac{U_{ijk}}{T_{ijk}\left(T_{ijk} + U_{ijk}\right)}}$$

Now consider the sample the tagging rates are being applied to (i.e. events with ≥ 5 jets). The background prediction, B, from the tagging rate matrix is given by:

$$B = \sum_{ijk} B_{ijk} \equiv \sum_{ijk} R_{ijk} M_{ijk}$$

Here B_{ijk} is the background prediction for each bin, and M_{ijk} is the number of taggable jets in a particular bin. The statistical uncertainty on B is given by:

$$\Delta B = \sqrt{\sum_{ijk} \left(\Delta B_{ijk}\right)^2} = \sqrt{\sum_{ijk} B_{ijk}^2 \left[\left(\frac{\Delta R_{ijk}}{R_{ijk}}\right)^2 + \frac{1}{M_{ijk}}\right]}$$

For $M_{ijk} \to 0$ or $\frac{\Delta R_{ijk}}{R_{ijk}}$ large, ΔB is large. As $T_{ijk} \to 0$, ΔR_{ijk} diverges. Therefore, in the construction of a tagging rate matrix, it is important to bin the matrix in a way such that there are no bins with zero rates.

The tagging rate matrix can also be used to get a prediction of the distribution of tags as a function of any given variable A. Let $P(\alpha)$ be the predicted number of tagged jets in the α^{th} bin of the variable A. It is a sum of the predicted numbers for

each individual bin in E_T, N_{SVX} and ΣE_T, $P_{ijk}(\alpha)$. If $L_{ijk}(\alpha)$ is the corresponding number of taggable jets and $R_{ijk}(\alpha)$ is the tagging rate, then $P(\alpha)$ can be written as:

$$P(\alpha) = \sum_{ijk} P_{ijk}(\alpha) = \sum_{ijk} L_{ijk}(\alpha)\frac{P_{ijk}(\alpha)}{L_{ijk}(\alpha)} \equiv \sum_{ijk} L_{ijk}(\alpha)R_{ijk}(\alpha)$$

If there is no dependence of tagging rates on A, then $R_{ijk}(\alpha) \rightarrow R_{ijk}$ in the limit of infinite statistics, and therefore:

$$P(\alpha) = \sum_{ijk} L_{ijk}(\alpha)R_{ijk}$$

On the other hand, if there is an explicit dependence of tagging rates on A and the rates are parameterized in terms of A, then:

$$P(i) = \sum_{jk} P_{ijk} = \sum_{jk} L_{ijk}\frac{P_{ijk}}{L_{ijk}} \equiv \sum_{jk} L_{ijk}R_{ijk}$$

Therefore, whether the tagging rates are explicitly parameterized in terms of A or not, the predicted distribution of tagged jets as a function of A is obtained by weighting the distribution of taggable jets by the tagging rates for each of the taggable jets. The uncertainty in the predicted distribution is given by:

$$\Delta P(\alpha) = P_{ijk}(\alpha)\sqrt{\frac{1}{L_{ijk}(\alpha)} + \left(\frac{\Delta R_{ijk}}{R_{ijk}}\right)^2}$$

In order to construct the tagging rate matrix and to choose the appropriate binning for different parameters, we look at the kinematic distributions of tagged jets in the 4-jet events. The corrected transverse energies of jets in the 4-jet events lie in a range of 20 to 200 GeV. Approximately 90% (95%) of the jets have a transverse energy less than 120 (140) GeV. Since there is a strong dependence of the tagging rates on the transverse energies of jets, the jets are binned as finely as possible in transverse energy. As mentioned in chapter 3, the uncertainty in the measurement of the transverse energy of a jet is $\sim$ 10% of the transverse energy of the jet, which corresponds to 10 GeV for a jet with E_T = 100 GeV. Jets with 20 GeV$\leq E_T \leq$120 GeV are partitioned into bins of 10 GeV in transverse energy in the tagging rate matrix. To reduce statistical uncertainties, jets with 120 GeV$\leq E_T \leq$140 GeV and $E_T >$140 GeV are grouped in individual bins. This results in a total of 12 bins.

The number of SVX tracks in a jet, N_{SVX}, ranges from 2 to 15. Approximately 90% (95%) of the jets have N_{SVX} less than 11 (13). The jets are therefore binned in the following fashion: ten bins for jets with $2 \leq N_{SVX} \leq 11$, one for $12 \leq N_{SVX} \leq 13$ and one for $N_{SVX} \geq 14$, for a total of 12 bins.

As shown in figure 5-5, the tagging rate in the 4-jet data shows a weak dependence on ΣE_T even after the E_T dependence is taken into account. Events observed in the data have ΣE_T from $\approx$ 150 to 600 GeV. They are grouped into three bins, $\Sigma E_T \leq 200$, $200 < \Sigma E_T \leq 350$ and $\Sigma E_T > 350$ GeV. A coarse binning in ΣE_T is chosen since the dependence of tagging rates on it is not as strong as for E_T and N_{SVX}.

Tagging rate matrices are constructed separately for positively and negatively tagged jets since the positive and negative tagging rates are not identical. As explained earlier, bins in the tagging rate matrix with a small number of tagged jets, result in large statistical uncertainties in their tagging rates. Therefore, the bins with zero tagging rates are collapsed into the nearest non-zero tagging rate bins in ΣE_T. ΣE_T is chosen because the dependence of the tagging rates on it is the weakest. Since the number of negatively tagged jets is significantly smaller than the number of positively tagged jets, this procedure is done separately for positive and negative tagging rate matrices.

5.2.3 Events with ≥ 1 b-tagged jets

We now apply the tagging rates measured in the 4-jet events (the background sample) to events with five or more jets (the signal sample). Using the tagging rates, the expected number of tagged jets and their kinematical distributions are calculated. It is seen that the tagging rates measured in the background dominated sample yield predictions that are in good agreement with what is observed in the data both before and after the $\Sigma E_T \geq 300$ GeV requirement. This implies that events with five or more jets are dominated by non-$t\bar{t}$ sources of heavy flavor production.

Table 5.3 summarizes the number of positive (N^+_{obs}) and negative (N^-_{obs}) tagged jets observed in the data and the number predicted ($N^{\pm}_{pred}$) using the 4-jet matrix before the ΣE_T requirement. The number observed should be identical to the number

predicted in 4-jet events since the tagging rates are derived from these events. Here, N_{able} is the number of taggable jets that the tagging rates are applied to. Figure 5-7 shows the E_T and N_{SVX} distributions of positively tagged jets observed in the data for events with ≥ 5 jets. The predictions of the tagging rate matrix are also shown. Similarly, figure 5-8 shows the distributions for negatively tagged jets. It is seen that the number of tagged jets in the data and their kinematical distributions are reproduced well by the predictions based on tagging rates derived from 4-jet events.

The results after the $\Sigma E_T \geq 300$ GeV requirement are summarized in table 5.4. The E_T and N_{SVX} distributions of positively tagged jets observed in the data for events with ≥ 5 jets and the predictions of the tagging rate matrix are shown in figure 5-9. The distributions for negatively tagged jets are shown in figure 5-10. Again, it is seen that the number of tagged jets in the data and their kinematical distributions are reproduced well by the predictions based on tagging rates derived from 4-jet events.

Events before the $\Sigma E_T \geq 300$ GeV requirement have already been shown to be consistent with QCD multijet production in chapter 4. Using the good agreement seen between our predictions and the tagged jets observed in the data, we infer that the dominant source of heavy flavor before the $\Sigma E_T \geq 300$ GeV requirement is also QCD multijet production. Since a good agreement is also seen after the $\Sigma E_T \geq 300$ GeV requirement, we further conclude that QCD multijet production is also the dominant source of heavy flavor in events with high total transverse energy.

As a basic check of this conclusion, we look at the kinematic distributions of the excess of positively tagged jets over negatively tagged jets. Since the positively tagged jets are primarily from heavy flavor production and mistags, the excess of the positively tagged jets over the negatively tagged jets consists only of heavy flavor jets. In figure 5-11 we compare the jet E_T distribution of the excess of positively tagged jets with the distribution from a QCD multijet Monte Carlo simulation. The good agreement seen both before and after the $\Sigma E_T \geq 300$ GeV requirement confirms that QCD multijet production is the dominant source of heavy flavor.

All ΣE_T	$N_{jet} = 4$	$N_{jet} = 5$	$N_{jet} = 6$	$N_{jet} \geq 7$
N_{able}	317776	140455	32639	5780
N^+_{obs}	8939	3855	944	160
N^+_{pred}	8939.0±94.5	3769.5±46.9	851.2±15.5	147.3±4.8
N^-_{obs}	1979	930	225	36
N^-_{pred}	1979.0±44.5	813.2±21.5	187.5±7.1	34.8±2.1

Table 5.3: Summary of the number of positive and negative tags observed and predicted using 4 jet tagging rate matrices in Run 1 data before the $\Sigma E_T \geq 300$ GeV requirement.

$\Sigma E_T \geq 300$ GeV	$N_{jet} = 4$	$N_{jet} = 5$	$N_{jet} = 6$	$N_{jet} \geq 7$
N_{able}	49089	39416	14860	3980
N^+_{obs}	1508	1185	454	107
N^+_{pred}	1468.8±28.0	1139.7±24.4	413.5±12.0	105.9±4.5
N^-_{obs}	400	319	116	26
N^-_{pred}	414.1±15.2	306.3±12.5	107.8±5.9	27.7±2.0

Table 5.4: Summary of the number of positive and negative tags observed and predicted using 4 jet tagging rate matrices in Run 1 data after the $\Sigma E_T \geq 300$ GeV requirement.

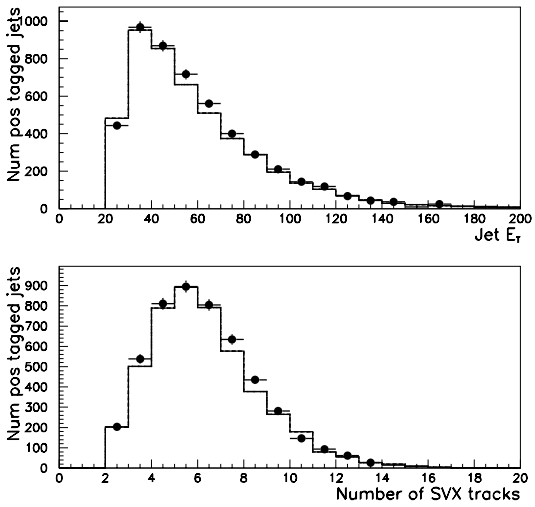

Figure 5-7: *A comparison of the predicted (histogram) and observed (squares) distributions of the transverse energies of positively tagged jets in events with* ≥ 5 *jets before the* ΣE_T *requirement.*

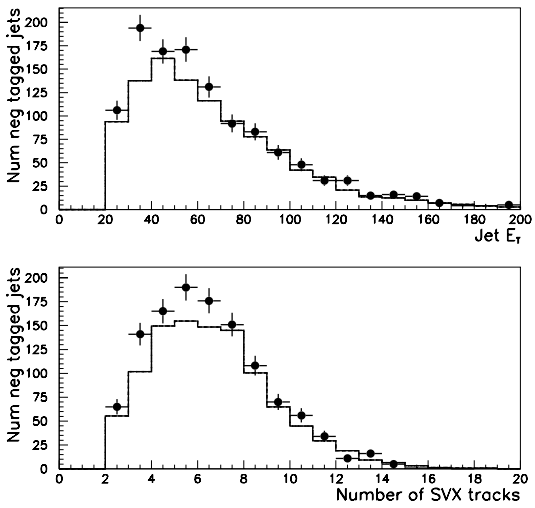

Figure 5-8: *A comparison of the predicted (histogram) and observed (squares) distributions of the transverse energies of negatively tagged jets in events with* ≥ 5 *jets before the* ΣE_T *requirement.*

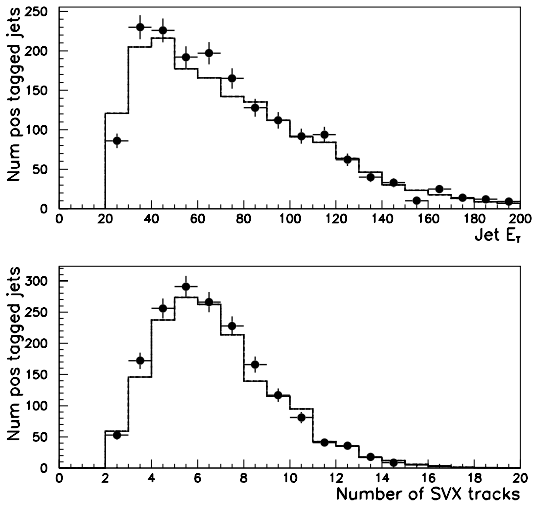

Figure 5-9: *A comparison of the predicted (histogram) and observed (squares) distributions of the transverse energies of positively tagged jets in events with* ≥ 5 *jets after the* ΣE_T *requirement.*

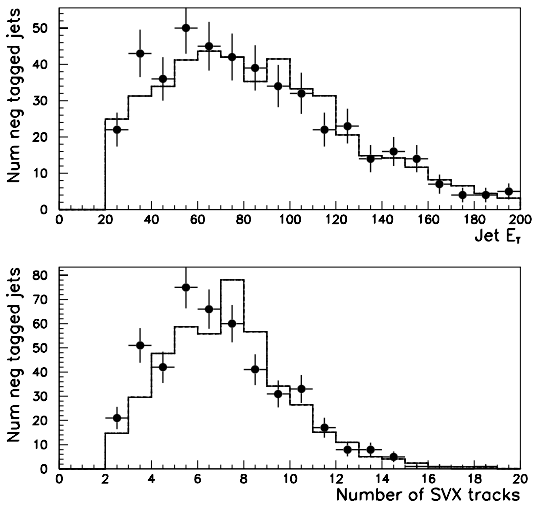

Figure 5-10: *A comparison of the predicted (histogram) and observed (squares) distributions of the transverse energies of negatively tagged jets in events with* ≥ 5 *jets after the* ΣE_T *requirement.*

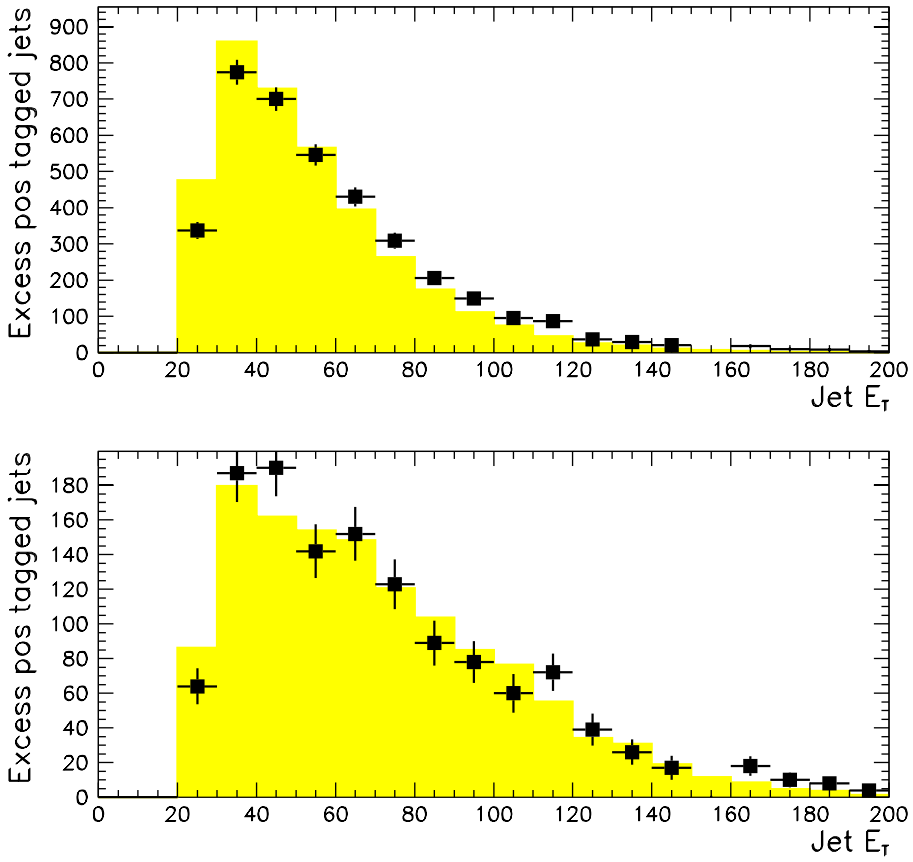

Figure 5-11: *A comparison of the jet E_T distribution of the excess of positively tagged jets over the negatively tagged jets (points) with QCD multijet Monte Carlo (histogram). The upper plot shows a comparison before the $\Sigma E_T \geq 300$ GeV requirement. The bottom plot shows the comparison after the $\Sigma E_T \geq 300$ GeV requirement. The normalization of the QCD Multijet Monte Carlo has been fixed to the normalization of the data.*

5.3 b-tagging efficiencies in $t\bar{t}$ events

In chapter 7 we will discuss the $t\bar{t}$ production cross-section which requires a knowledge of the b-tagging efficiencies in $t\bar{t}$ events. To permit a comparison with b-tagging efficiency studies that have been performed elsewhere[32], b-tagging efficiency is calculated for three different cases: the efficiency of identifying ≥ 1 b jets per event, the efficiency of identifying ≥ 2 b jets per event and the efficiency of identifying ≥ 1 double tagged combinations per event. In the first two cases, the efficiency is given by the number of $t\bar{t}$ events with ≥ 1 or ≥ 2 b-tags divided by the total number of events. In the last case, the efficiency is given by the number of double tagged combinations divided by the number of $t\bar{t}$ events.

In order to determine b-tagging efficiencies, we use a $t\bar{t}$ Monte Carlo followed by a CDF detector simulation. Because of the dependence on the CDF detector simulation, in particular on the simulation of the CTC and SVX tracking efficiencies, we need to cross-check the modelling of b quark jets in our simulation with the data. These cross-checks were performed in detail for the top quark search in the $\ell + jets$ channel [51, 3] and are briefly summarized here.

By studying individual tracks, it is determined that the CDF tracking simulations are optimistic. The reconstruction efficiency of tracks is higher in the Monte Carlo simulations than the efficiency observed in the data. As mentioned in chapter 3, tracks are reconstructed from individual hits in the CTC and SVX detectors. When the number of hits is high, the probability of reconstructing a given track decreases due to the ambiguities introduced by the presence of extra hits around the track. The tracking simulations do not take this effect into account properly. In order to compensate for this effect, the loss of track reconstruction efficiency is parameterized as a function of the number of hits around the track, and then the track finding efficiency is degraded in the Monte Carlo simulations using this parameterization. Since b-tagging depends on the identification of tracks in the CTC and the SVX, the track degradation results in a lower b-tagging efficiency.

The track finding degradation method is checked by looking at the inclusive elec-

tron sample. As already mentioned, this data sample is enriched in $b\bar{b}$ events, where an electron from a semileptonic b-hadron decay is recoiling against a jet from the other b. Distributions of track multiplicity and other kinematical properties (e.g. invariant mass of the tracks associated to a secondary vertex, their total transverse momentum and their $c\tau$) in a Monte Carlo simulation with track finding degradation are compared to the distributions observed in the data. A good agreement is seen between the two, and their level of disagreement is used to estimate the systematic uncertainties introduced by the track degradation procedure.

Using a sample of $t\bar{t}$ Monte Carlo events, the tagging efficiency for a b quark jet is determined before and after the application of track finding degradation. The effect of track degradation on b-tagging efficiencies is two-fold. First, the number of taggable jets in an event is reduced. This is because jets have fewer "good" SVX tracks (as defined in Appendix A) required for them to be taggable. Second, the tagging rate per taggable jet is also reduced. This also results from a reduction in the overall number of tracks and therefore fewer tracks pass the Pass 1 and Pass 2 requirements of the b-tagging algorithm. It is seen that the b-tagging efficiency for taggable jets in the Monte Carlo is lower by a factor of $s_j = 0.85 \pm 0.01$ (statistical uncertainty only), also referred to as the "jet scale factor". We also define an "event scale factor", s_{evt}, as the fractional loss in the efficiency to observe at least one b-tagged jet in a $t\bar{t}$ event. If ϵ_j is the probability of tagging a taggable b or c quark jet, and f_k is the fraction of events with k taggable jets, then the event tagging efficiency, ϵ_{evt} is given by:

$$\epsilon_{evt}(f_k, s_j, \epsilon_j) \;=\; \sum_{k=1}^{\infty} f_k[1 - (1 - s_j\epsilon_j)^k]$$

The event scale factor, s_{evt}, is then defined as:

$$s_{evt} \;\equiv\; \frac{\epsilon_{evt}(f_k, s_j, \epsilon_j)}{\epsilon_{evt}(f_k, 1, \epsilon_j)}$$

For Run 1B data, the event scale factor is measured to be 0.87 ± 0.06, where the uncertainty includes the contribution from all the systematic and statistical sources.

The track degradation method is tuned to reproduce Run 1B data (with the SVX′ detector) and is an improvement over the method originally used for the Run

1A data [51]. For Run 1A, the scale factors are directly determined by comparing the b-tagging efficiencies of jets in the inclusive electron data sample and a Monte Carlo simulation. This method introduces large uncertainties in the scale factor due to two reasons. First, due to limited statistics, the uncertainties in the b-tagging efficiencies in the data are large. And second, the b-tagged jets in the inclusive electron sample are from semileptonic decays of the b quark, whereas the b quark jets in $t\bar{t}$ decays include all the possible decay modes of the b quarks. In addition, the average E_T of the b quark jets in $t\bar{t}$ decays is higher than it is in inclusive electron events. Although the scale factor is not seen to be strongly dependent on the E_T of the jets, a large systematic uncertainty is assigned to the scale factor in extrapolating to $t\bar{t}$ events. Finally, the scale factor for Run 1A is determined to be 0.72 ± 0.21.

In order to determine the expected number of $t\bar{t}$ events with ≥ 2 b-tagged jets, we also calculate the efficiencies for tagging ≥ 2 jets and ≥ 1 double tagged combinations in an event. Their corresponding scale factors are also determined by comparing the tagging rates in the $t\bar{t}$ Monte Carlo before and after track degradation. In terms of the scale factor for tagging ≥ 1 jets, s_{evt}, the scale factor for tagging ≥ 2 jets is s_{evt}^2 and the scale factor for tagging ≥ 1 double tagged combinations is s_{evt}^3. This is because of a combined effect of the reduction in the number of taggable jets and tagging rates per taggable jet for every event. An investigation of the effect of track degradation in $t\bar{t}$ Monte Carlo is detailed in Appendix B. The uncertainties in the efficiencies for tagging ≥ 2 jets and ≥ 1 double tagged combinations are $2\delta s_{evt}$ and $3\delta s_{evt}$ respectively, where δs_{evt} is the fractional uncertainty in s_{evt}.

The efficiencies for tagging ≥ 1 jets, ≥ 2 jets and ≥ 1 double tagged combinations in a $t\bar{t}$ event are summarized in table 5.5 for Run 1A and 1B respectively. These tagging efficiencies are for $t\bar{t}$ events with $\Sigma E_T \geq 300$ GeV. The tagging efficiencies for $t\bar{t}$ events before the ΣE_T requirement are in very good agreement with these values.

Using the b-tagging efficiencies we calculate the expected number of $t\bar{t}$ events with tagged jets. To see the effect of b-tagging in reducing background from light quark and gluon jets, the signal to background ratio (S/B) is shown in table 5.6 after the $\Sigma E_T \geq 300$ GeV requirement using a $t\bar{t}$ production cross-section of 6.8 pb. The

$\Sigma E_T \geq 300$ GeV	$N_{jet} = 4$	$N_{jet} = 5$	$N_{jet} = 6$	$N_{jet} \geq 7$
$\geq 1b$ tags (1A)	35.1±17.3%	36.5±17.9%	37.0±18.2%	35.8±17.7%
$\geq 1b$ tags (1B)	42.4±11.4%	44.1±11.7%	44.7±11.9%	43.2±11.6%
$\geq 2b$ tags (1A)	7.6±5.3%	7.7±5.4%	8.4±5.8%	8.5±6.0%
$\geq 2b$ tags (1B)	11.1±4.2%	11.3±4.2%	12.2±4.6%	12.4±4.8%
$\geq 1b$ comb (1A)	6.5±5.5%	7.1±6.1%	7.7±6.6%	7.6±6.5%
$\geq 1b$ comb (1B)	11.5±5.3%	12.5±5.8%	13.7±6.3%	13.3±6.2%

Table 5.5: b-tagging efficiencies in $t\bar{t}$ Monte Carlo events for Run 1A and 1B data after the ΣE_T requirement. The efficiencies are given for observing events with ≥ 1 b-tagged jets, ≥ 2 b-tagged jets and ≥ 1 b-tagged combinations.

$\Sigma E_T \geq 300$ GeV/c^2	$N_{jet} = 4$	$N_{jet} = 5$	$N_{jet} = 6$	$N_{jet} \geq 7$
$\geq$1 SVX +	1/80	1/24	1/12	1/8
$\geq$2 SVX +	1/22	1/9	1/5	1/4

Table 5.6: Signal to background ratio, for different tagging requirements assuming a $t\bar{t}$ cross section of 6.8 pb.

S/B ratio is maximum when events have ≥ 2 b-tagged jets. Therefore, as the final requirement of the analysis, we require that events have ≥ 2 b-tagged jets in them.

It should be noted that $t\bar{t}$ events can have ≥ 3 b-tagged jets because of two reasons. First, 50% of the hadronic decays of the W boson are into a $c\bar{s}$ pair where the c quark can be tagged. Second, less frequently, a hard gluon in the event can split into a $b\bar{b}$ or a $c\bar{c}$ pair. Therefore, in order to include events with ≥ 3 b-tagged jets and also to facilitate the background calculation for fake double tagged combinations, we count the number of double tagged combinations in the data, and use the efficiency for tagging ≥ 1 double tagged combinations to calculate the $t\bar{t}$ production cross-section.

5.4 Expected number of double tagged combinations

In order to calculate the expected number of fake and real double tagged combinations, we again use a method based on the tagging rates of jets. We apply the positive and negative tagging rates determined from the 4-jet events to pairs of taggable jets in ≥ 5 jet events to determine the expected number of double tagged combinations.

5.4.1 Fake double tagged combinations

Fake double tagged combinations can be of the type bf or ff, where b denotes a b quark jet and f denotes a mistagged jet. The calculation of the expected number of fake double tagged combinations proceeds in two steps. First, the expected number of fake double tagged combinations is calculated for each event, and second the answer is summed for all the events to get the total number. The calculation is done separately for bf and ff combinations.

For bf combinations, all events with at least one positive tag are considered, and the negative tagging rate is applied to each of the extra taggable jets in the event. The result is summed over all distinct combinations of the type bj where j denotes a taggable jet (j may or may not be tagged) to give the expected number of fake double tagged combinations for an event. Figure 5-12 shows the expected number of bf combinations in a 4-jet event for two different cases. First, for an event with three taggable jets and only one tagged jet. And second, for an event with three taggable jets of which two are tagged. Finally, the expected number of double tagged combinations for each event are summed to get the total expected number in the data sample. The number of fake double tagged combinations of the type bf, N_{bf}, is thus given by:

$$N_{bf} = \sum_{events} \sum_{N_c^+} \sum_{j} r_j^-$$

Here N_c^+ is the number of distinct combinations (pairs) of taggable jets such that at least one jet is positively tagged, and j is the index for all the extra taggable jets

in the event.

The number of fake double tagged combinations of the type ff, N_{ff}, is also calculated in a similar fashion. For ff combinations, events with at least one negative tag are used to calculate the expected number per event and then the result is summed over all events. Therefore, N_{ff} can be written as:

$$N_{ff} = \sum_{events} \sum_{N_c^-} \sum_{j} r_j^-$$

Here N_c^- is the number of distinct combinations (pairs) of taggable jets such that at least one jet is negatively tagged, and j is the index for all the extra taggable jets in the event.

This calculation method uses only the negative tag rates. Since the number of fake combinations is being used, this method naturally accommodates events which have multiple positive or negative tags.

We check this background calculation by comparing the predicted number of fake double tagged combinations and their kinematical distributions with the number and distributions of fake combinations actually present in the ≥ 5 jet data. Table 5.7 summarizes the number of fake combinations observed in the data and the number predicted by the 4-jet tagging rate matrix for different jet multiplicities without any ΣE_T requirement. Figure 5-13 compares the azimuthal separation ($\Delta\phi$) of the tagged jets in the fake combinations observed in data with the predicted distribution. The comparison is shown separately for the background (4-jet events) and signal (≥ 5 jet events) samples. Similarly, table 5.8 and figure 5-14 show the comparison for fake double tagged combinations in events with $\Sigma E_T \geq 300$ GeV. It is seen that the predicted number and distributions of fake double tagged combinations are in good agreement with those observed in the data.

In this analysis, the number of fake combinations in data is taken to be the number observed. Their kinematic distributions are taken from the predictions of the negative tagging rate matrix. This results in smooth high-statistics distributions.

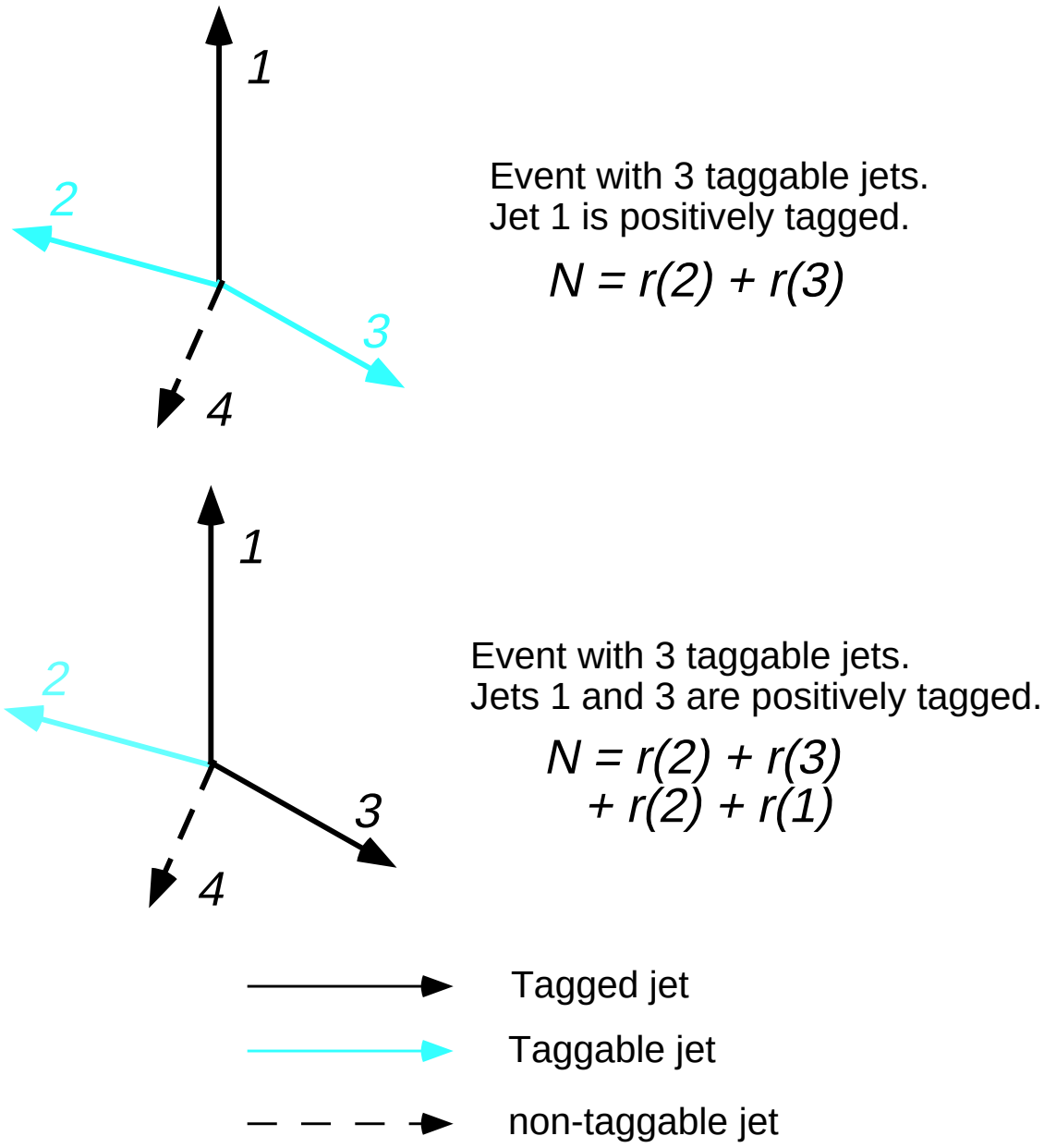

Figure 5-12: *An illustration of the method used to calculate the number of fake double tagged combinations.*

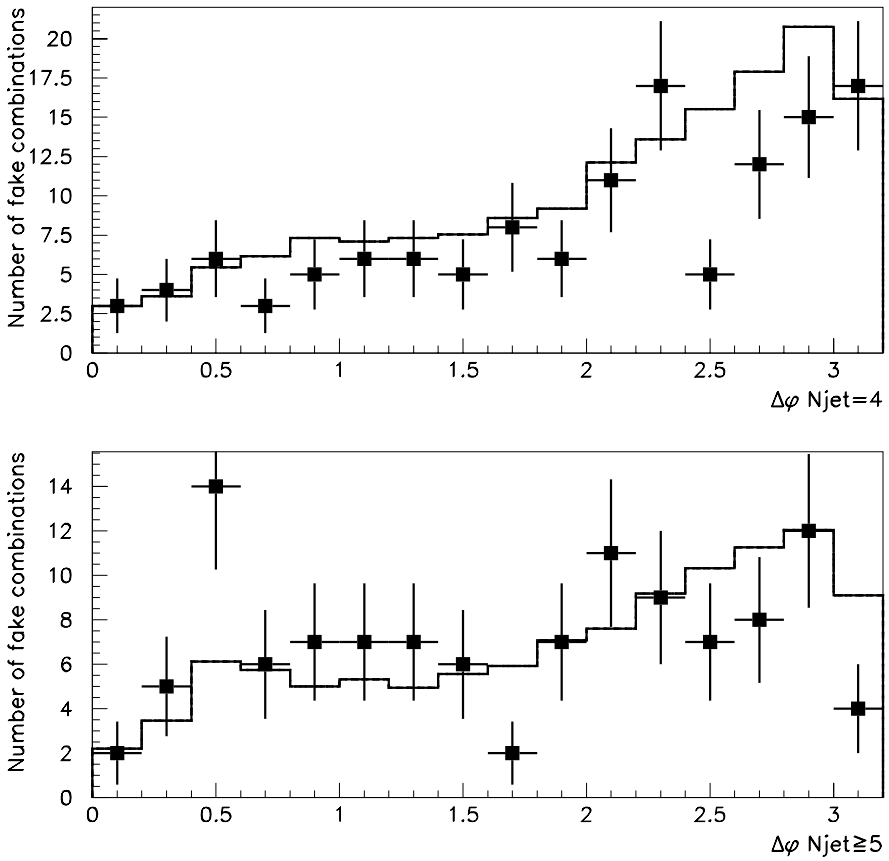

Figure 5-13: *Observed (squares) and predicted (histogram) $\Delta\phi$ distributions for different jet multiplicities before the ΣE_T requirement. The top plot shows the distribution for 4 jet events, and the bottom plot for ≥ 5 jet events.*

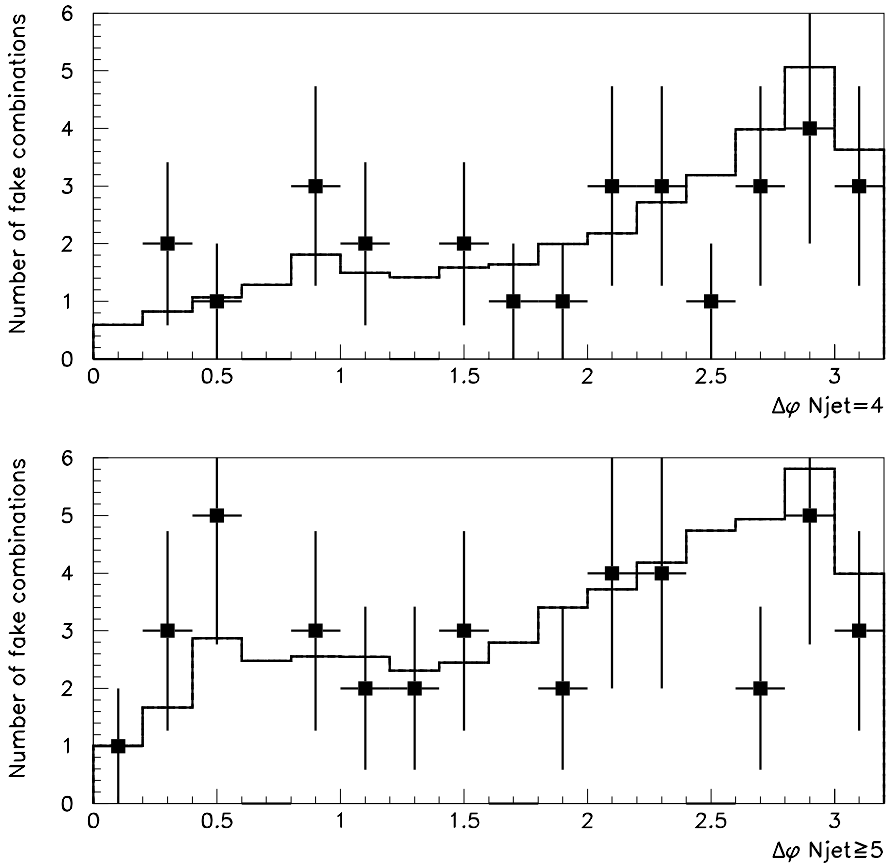

Figure 5-14: *Observed (squares) and predicted (histogram) $\Delta\phi$ distributions for different jet multiplicities after the ΣE_T requirement. The top plot shows the distribution for 4 jet events, and the bottom plot for ≥ 5 jet events.*

All ΣE_T	$N_{jet} = 4$	$N_{jet} = 5$	$N_{jet} = 6$	$N_{jet} = 7$
$N_{obs}^{+-/--}$	163	95	29	3
$N_{pred}^{+-/--}$	161.3±3.4	82.4±2.1	23.6±1.0	4.9±0.2

Table 5.7: Summary of the number of fake combinations observed in Run 1 data and the number predicted using the fake tagging rate matrix before the ΣE_T requirement.

$\Sigma E_T \geq 300$ GeV	$N_{jet} = 4$	$N_{jet} = 5$	$N_{jet} = 6$	$N_{jet} = 7$
$N_{obs}^{+-/--}$	29	26	12	1
$N_{pred}^{+-/--}$	34.5±1.2	33.4±1.4	14.1±0.8	4.0±0.2

Table 5.8: Summary of the number of fake combinations observed in Run 1 data and the number predicted using the fake tagging rate matrix after the ΣE_T requirement.

5.4.2 Real double tagged combinations

The number of real double tagged combinations can be calculated using a method similar to the calculation for the fakes. For bb combinations, all events with at least one positive tag are considered, and the positive tagging rate is applied to each of the extra taggable jets in the event. The result is summed over all distinct combinations of the type bj where j denotes a taggable jet (j may or may not be tagged). The prediction, N_{bb} can be written as:

$$N_{bb} = \sum_{events} \sum_{N_c^+} \sum_{j} r_j^+$$

Here N_c^+ is the number of distinct combinations (pairs) of taggable jets such that at least one jet is positively tagged, and j is the index of all the extra taggable jets in the event.

Before requiring $\Sigma E_T \geq 300$ GeV, 778 real double tagged combinations are observed in 4-jet events. The predicted number of double tagged combinations is 609.3±8.1. This drastic underprediction suggests that a naive application of the 4-jet tagging rates cannot be used in this case. In the calculation of the expected number

of fake double tagged combinations, the negative tagging rates were applied to the taggable jets assuming that the probability of a negative tag for a jet depended only on the parameters of that jet and was independent of the rest of the event. This was justified because mistags arise primarily from finite detector resolution. Thus tagged jets were taken to be independent of each other. This assumption is borne out by the good agreement between the predictions and the fake double tagged combinations observed in the data.

However QCD production of $b\bar{b}$ and $c\bar{c}$ pairs is *correlated*. This means that the identification of one b or c quark in the event enhances the probability of observing another. This main reason for this correlation is the fiducial and kinematic acceptance of the heavy flavor quarks. Since these quarks are produced in pairs, their kinematical properties are very similar from different conservation principles. For example, for directly produced $q\bar{q}, gg \rightarrow b\bar{b}$ pairs, the transverse momenta of the two jets should match, and therefore, if one results in a jet passing the minimum transverse energy requirement to be taggable, the other one is also likely to. Similarly, if one quark lies within the fiducial acceptance of the SVX, the other one is also likely to be accepted. Application of jet tagging rates to individual taggable jets cannot account for these correlations. To take these correlations into account, the rates for events to have ≥ 2 tagged jets must be calculated, using variables that incorporate information not only about the tagging rates of individual jets and but also the global kinematical properties of the events. In the application of the event tagging rates, the average number of taggable jets also needs to be considered for different jet multiplicities. Clearly the number rises as the number of jets increases. An ideal scenario is to measure the double b-tagging rates in an independent sample of QCD rich double tagged events. No such high statistics data sample is available in the CDF data set at the moment. Therefore, this analysis relies on a Monte Carlo based method for the determination of the QCD normalization, as described in the next chapter.

Chapter 6

Physics backgrounds to the $t\bar{t}$ signal

Our final data sample consists of events with a total transverse energy greater than 300 GeV and containing at least two b-tagged jets. In the previous chapter, we have discussed the mistag background to such events. In this chapter we consider different Standard Model sources (other than $t\bar{t}$) of such events, and calculate the expected number of events from each of them. In increasing order of importance, these Standard Model processes include the production of W or Z boson pairs, single top quark production, production of W or Z bosons in association with quark or gluon jets, and QCD multijet production. We use Monte Carlo simulations of these processes followed by a simulation of the CDF detector to calculate the expected number of events. For each process, a Monte Carlo generator is used that is known to model it most reliably.

6.1 Diboson production

The production of heavy boson (W or Z) pairs and their fully-hadronic decay into quarks results in events with four jets. However, emission of hard gluons increases the jet multiplicity of the final state. The hadronic decays $Z \rightarrow b\bar{b}, c\bar{c}$ and $W \rightarrow c\bar{s}$ produce high E_T heavy flavor jets that can be tagged. Diboson production is

simulated separately for WW, WZ and ZZ pairs using the ISAJET[36] Monte Carlo. The number of expected events are calculated using the theoretical cross sections [1] for these processes which are known accurately [58]. Diboson events have a low efficiency ($\sim$ 17%) for passing the trigger and the cleanup requirements of the analysis, which reduces the expected number of events. In addition, since the b-tagging efficiency for c quark jets is low, most of the events with ≥ 2 b-tagged jets come from WZ or ZZ decay. Due to the small cross-sections of these processes, the expected contribution of diboson production to our final data sample is negligible as summarized in table 6.1. After the $\Sigma E_T \geq 300$ GeV requirement, the number of events with ≥ 2 b-tagged jets is taken to be zero.

All ΣE_T	$N_{jet} = 4$	$N_{jet} = 5$	$N_{jet} = 6$	$N_{jet} = 7$
≥ 2 b-tags	0.6	0.5	0.1	0.0

Table 6.1: Expected number of double tagged events (N_{2tag}) from diboson production before the $\Sigma E_T \geq 300$ GeV requirement.

6.2 Single top quark production

Single top quark production has been discussed previously in chapter 2. The theoretical production cross-section is $\sim$ 4 pb. Only the fully hadronic final decay modes are pertinent to this analysis, which reduces the effective cross section by approximately a factor of two. Single top events were simulated using the PYTHIA[38] Monte Carlo. Table 6.2 summarizes the expected number of single top events for different jet multiplicities, with ≥ 0, ≥ 1 and ≥ 2 b tagged jets after the $\Sigma E_T \geq 300$ GeV requirement. Their contribution to our final data sample is small.

[1] The production cross-sections for dibosons are: $\sigma(WW) = 10.0$ pb, $\sigma(WZ) = 2.5$ pb and $\sigma(ZZ) = 1.0$ pb

$\Sigma E_T \geq 300$ GeV	$N_{jet} = 4$	$N_{jet} = 5$	$N_{jet} = 6$	$N_{jet} = 7$
All	3.8	4.3	1.9	0.5
≥ 1 b-tags	1.6	1.7	0.8	0.2
≥ 2 b-tags	0.4	0.7	0.3	0.1

Table 6.2: Expected number of single top quark events after the ΣE_T requirement.

6.3 Production of W or Z bosons with jets

The production of a W or a Z boson in association with jets contributes to the multijet data through three distinct processes. These are $Z + jets$ production followed by the $Z \rightarrow b\bar{b}/c\bar{c}$ decay, production of the W boson in association with $b\bar{b}/c\bar{c}$ pairs and production of the Z boson in association with $b\bar{b}/c\bar{c}$ pairs. We calculate the expected number of events from each of them using the cross-sections for $W/Z + jets$ measured at CDF. The expected numbers for each process are detailed separately below.

6.3.1 $Z + jets$ $(Z \rightarrow b\bar{b}/c\bar{c})$

Z+1 jet events are produced through $qg \rightarrow qZ$ (Compton scattering) and $q\bar{q} \rightarrow gZ$ (quark annihilation) processes as shown in figure 6-1. Gluon radiation and gluon splitting are the dominant sources of higher jet multiplicities. The $Z \rightarrow b\bar{b}/c\bar{c}$ decay produces high E_T jets that can be tagged with a high efficiency. The cross-section for $Z+ \geq N$ jet $(Z \rightarrow e^+e^-)$ production has been measured at CDF [55] using $\Delta R = 0.4$ cone size jets with $E_T \geq 15$ GeV and $|\eta| \leq 2.4$. The jets are required to be a distance $R = 1.3 \times \Delta R$ away from the closest electron from the Z decay. In addition, all jets that are less than the distance R are merged into a single jet. This procedure ensures that the jets are not misidentified electrons and are not the jets from the hadronic decay of the Z itself.

The $Z+ \geq 2$ jet events were simulated using the HERWIG[37] Monte Carlo. Default HERWIG does not include Z+jets production, so the W+jets generation routine was modified for this purpose [35]. Consistency checks between the HERWIG

and the VECBOS[54] Monte Carlo predictions for Z+jets production with $Z \rightarrow e^+e^-$ have been performed, and indicate that the modelling of $Z+ \geq 2$ jet events in HERWIG agrees with the data.

Since the selection of the $Z+ \geq N$ jet ($Z \rightarrow e^+e^-$) cross-section measurement is different from the selection of the present analysis, the number of expected events is calculated using the following procedure: $Z+ \geq N$ jet ($Z \rightarrow e^+e^-$) events are generated using the Monte Carlo. The ratio $K_N \equiv \frac{\sigma_{measured}}{\sigma_{Monte\ Carlo}}$ is measured for each jet multiplicity (N), and applied as an event weight to $Z+N$ jet Monte Carlo events. The K_N factors arise because the Monte Carlo cannot simulate physics processes to all orders in the perturbation expansion. By applying the K_N factors, the Monte Carlo calculations can be corrected for the effect of the neglected higher order terms. After applying the K_N factors, the Monte Carlo events are redistributed in different jet multiplicity bins according to the selection of this analysis. Finally, the number of expected events is calculated by scaling the Monte Carlo predictions to the total Run 1 luminosity of 109.4 pb^{-1} [56]. Table 6.3 shows the expected number of $Z+N$ jet events with ≥ 2 b-tagged jets before and after the ΣE_T requirement. The expected number includes the contributions from two different decay modes, $Z \rightarrow b\bar{b}$ and $Z \rightarrow c\bar{c}$. The efficiency to pass the trigger, the ΣE_T and b-tagging requirements, for different jet multiplicities, is calculated using the Monte Carlo. It is seen that the expected contribution from this process to our final data sample is small.

$Z+jets\ (Z \rightarrow b\bar{b}/c\bar{c})$	$N_{jet}=4$	$N_{jet}=5$	$N_{jet} \geq 6$
≥ 2 b-tags (All ΣE_T)	25.7 ± 3.6	8.0 ± 3.5	3.3 ± 3.1
≥ 2 b-tags ($\Sigma E_T \geq 300$ GeV)	1.7	1.5	1.4

Table 6.3: Expected number of double tagged Z+N events before and after the $\Sigma E_T \geq$ 300 GeV requirement.

6.3.2 $Wb\bar{b}, Wc\bar{c}$

Figure 6-2 shows the leading order Feynman diagram for $W/Z + b\bar{b}/c\bar{c}$ production. The predominant source of heavy flavor pair production in $W+ \geq N$ jet events is final state gluon splitting with some contribution from initial state gluon splitting and higher order diagrams. The HERWIG[37] Monte Carlo was used for $Wb\bar{b}$ and $Wc\bar{c}$ simulation. The contribution of $Wb\bar{b}$ and $Wc\bar{c}$ production to the $\ell + jets$ top analysis has been thoroughly investigated previously [3, 51]. We use the b-tagging rates estimated in these studies in this calculation. The efficiencies for passing the trigger and the ΣE_T cut are calculated using a Monte Carlo simulation.

The production cross section for $W+ \geq N$ jet ($W \rightarrow e\nu$) events has been measured at CDF in a similar way to the $Z+ \geq N$ jet events [57]. Therefore, the expected number of $W + N$ jet ($W \rightarrow qq'$) events in the multijet sample is calculated using a method analogous to the $Z + N$ jet event calculation [56]. The number of expected events with ≥ 2 b-tagged jets and $\Sigma E_T \geq 300$ GeV are summarized in table 6.4.

$Wb\bar{b}/c\bar{c}$	$N_{jet} = 4$	$N_{jet} = 5$	$N_{jet} \geq 6$
≥ 2 b-tags (All ΣE_T)	1.7 ± 0.8	0.4 ± 0.2	0.2 ± 0.1
≥ 2 b-tags ($\Sigma E_T \geq 300$ GeV)	0.1	0.1	0.1

Table 6.4: Expected number of double tagged $Wb\bar{b}/c\bar{c}$ events before and after the $\Sigma E_T \geq 300$ GeV requirement.

6.3.3 $Zb\bar{b}, Zc\bar{c}$

The $Zb\bar{b}/c\bar{c}$ process is distinct from $Z + jets$ ($Z \rightarrow b\bar{b}/c\bar{c}$) production and is the analogue of $Wb\bar{b}/Wc\bar{c}$ process. The contribution of this background is calculated in the same way as the $Wb\bar{b}/Wc\bar{c}$ background, by applying double tagged event rates in $W + jets$ events to the number of $Z + jets$ events expected. This mthod is justified because the predominant source of $b\bar{b}/c\bar{c}$ pairs is initial and final state gluon splitting which should be independent of the heavy boson being produced. The efficiency to

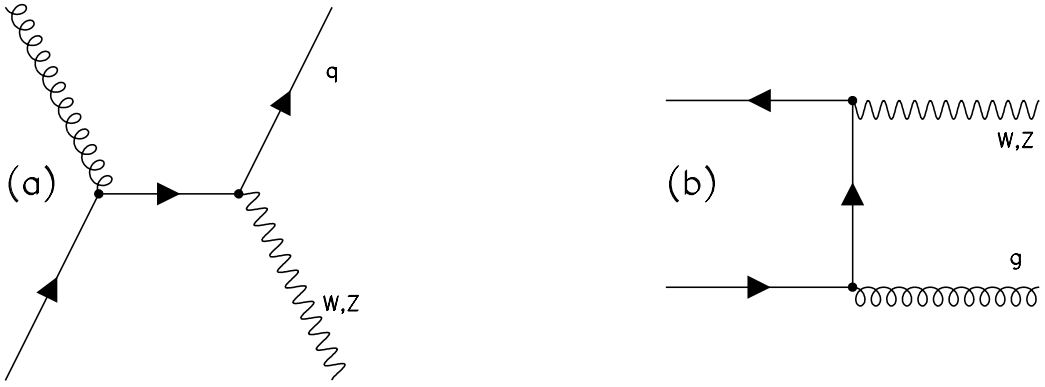

Figure 6-1: *Leading order Feyman diagrams for W/Z+jets production, Compton scattering (a) and quark annihilation (b).*

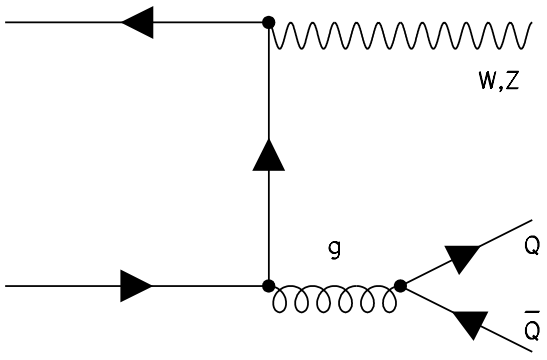

Figure 6-2: *Leading order Feyman diagram for $W/Z + b\bar{b}/c\bar{c}$ production.*

pass the total transverse energy requirement is taken to be the same as for Z+jets events. The results are summarized in table 6.5.

$Zb\bar{b}/c\bar{c}$	$N_{jet} = 4$	$N_{jet} = 5$	$N_{jet} \geq 6$
≥ 2 b-tags (All ΣE_T)	0.74 ± 0.35	0.38 ± 0.22	0.05 ± 0.04
≥ 2 b-tags ($\Sigma E_T \geq 300$ GeV)	0.1	0.1	0.0

Table 6.5: Expected number of double tagged $Zb\bar{b}/c\bar{c}$ events before and after the $\Sigma E_T \geq 300$ GeV requirement.

6.4 QCD multijets with heavy flavor

QCD processes are the dominant source of heavy flavor production in the multijet channel. The primary $2 \rightarrow 2$ processes that yield a heavy flavor quark pair ($Q\bar{Q}$, Q=b or c) are Direct Production ($q\bar{q}, gg \rightarrow Q\bar{Q}$), Flavor Excitation (initial state $g \rightarrow Q\bar{Q}$ with subsequent $Qg \rightarrow Qg$) and Gluon Splitting ($g \rightarrow Q\bar{Q}$) in the initial or final state. Some of the Feynman diagrams for QCD multijet production with $Q\bar{Q}$ pairs are shown in figure 6-3. Higher jet multiplicities are due to gluon radiation and/or splitting in the initial or final states to quarks and gluons. QCD produces correlated $Q\bar{Q}$ pairs and therefore their expected number cannot be estimated using a naive application of positive jet tagging rates, as explained in chapter 5. Therefore, a QCD Multijet Monte Carlo is used.

QCD $Q\bar{Q}$ production is simulated using the PYTHIA[38] Monte Carlo. The simulation is very CPU intensive because of three reasons. First, the leading order processes are a $2 \rightarrow 2$ scattering. Therefore, N jet processes are supressed by a factor $\sim \alpha_s^{N-2}$ (the multijet events of this analysis have at least 4 jets). Second, the requirement of b or c quarks in the final state adds another suppression factor, since the predominant process is light quark production. And finally, QCD multijet production has a low efficiency for passing the trigger, selection and $\Sigma E_T \geq 300$ GeV kinematical requirements of our analysis.

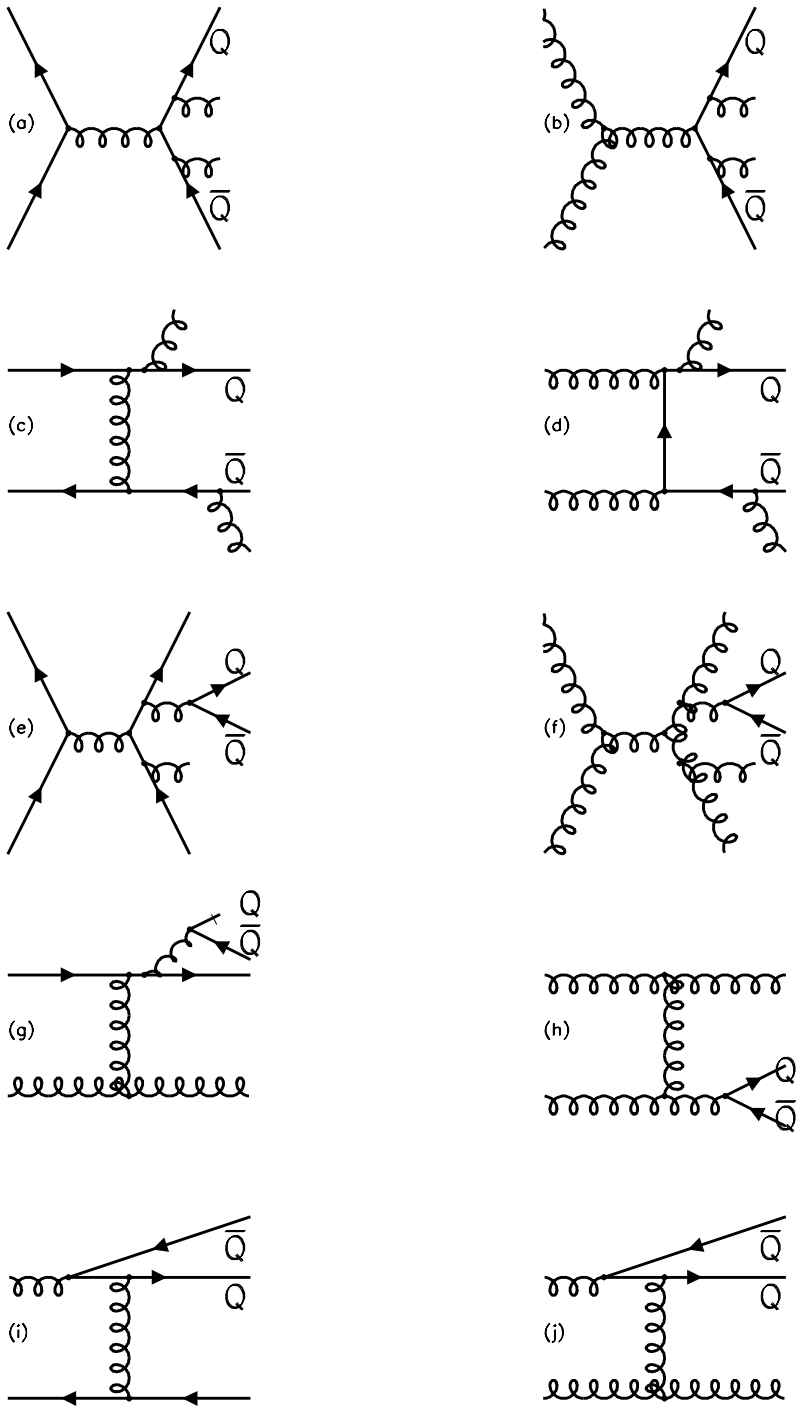

Figure 6-3: *Some of the Feynman diagrams for QCD multijet production with correlated heavy flavor $Q\bar{Q}$ production. Diagrams (a)-(d) are examples of direct production, (e)-(h) are examples of final state gluon splitting and (i)-(j) are examples of flavor excitation.*

	$N_{jet} = 4$	$N_{jet} = 5$	$N_{jet} = 6$	$N_{jet} = 7$
FE (%)	21.8±1.0	14.8±1.3	10.2±2.5	8.6±5.2
DP (%)	15.6±0.8	5.6±0.8	8.0±2.1	2.9±2.9
GS (%)	62.6±1.9	79.6±3.7	81.2±8.9	88.6±21.9

Table 6.6: Fraction of ≥ 2 b-tagged events that are produced by Flavor Excitation, Direct Production and Gluon Splitting before the $\Sigma E_T \geq 300$ GeV requirement.

The relative contribution of different production mechanisms to heavy flavor pair production can be studied by looking at the distributions of double tagged combinations in events with at least two b-tags. By studying their differences, the composition of the QCD background can be estimated. For each of the primary $2 \rightarrow 2$ processes (flavor excitation, direct production and gluon splitting), figure 6-4 shows the separation in $\eta - \phi$ space (ΔR), the separation in azimuth ($\Delta\phi$), the invariant mass (M) and the combined transverse momentum (p_T) distributions of tagged jet pairs in ≥ 2 b-tagged 4-jet Monte Carlo events before the $\Sigma E_T \geq 300$ GeV requirement. The fractions of ≥ 2 b-tagged events from each process in the QCD Monte Carlo simulation are summarized in table 6.6 for different jet multiplicities before the $\Sigma E_T \geq 300$ GeV requirement. The quoted uncertainties are statistical only. It is seen that gluon splitting is the dominant $Q\bar{Q}$ pair production mechanism and its contribution increases with increasing jet multiplicity.

6.4.1 Comparison of QCD Monte Carlo and Data

In order to check our Monte Carlo modelling of QCD multijet production of $Q\bar{Q}$ pairs, we look at the 4-jet events with ≥ 2 b-tagged jets and $\Sigma E_T \geq 300$ GeV. The expected contribution from $t\bar{t}$ production is small in these events and therefore they are dominated by QCD multijet production and mistags. Figure 6-5 shows a fit of the invariant mass ($M_{b\bar{b}}$) distribution of double tagged combinations in 4-jet events to a sum of QCD multijets and mistags. The $M_{b\bar{b}}$ distribution of the mistag background

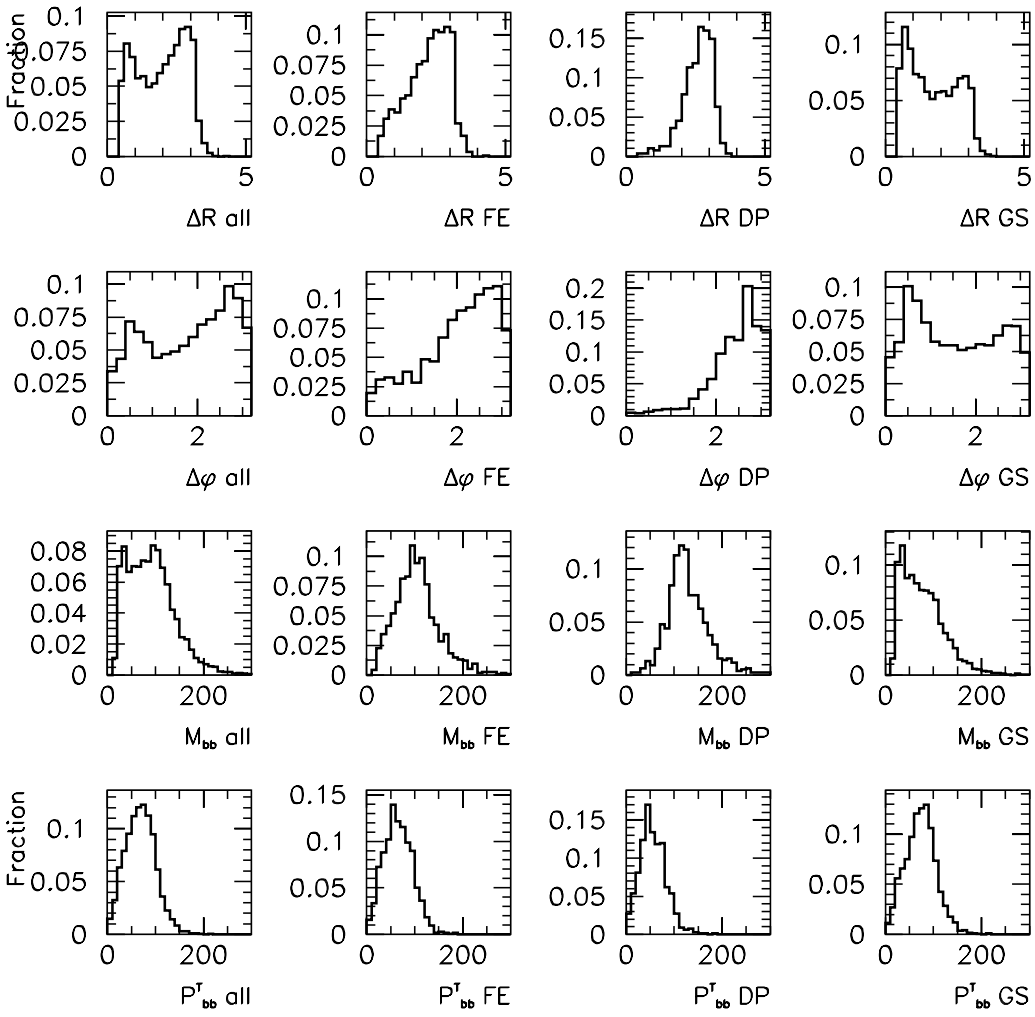

Figure 6-4: *Kinematical distributions of the double tagged combinations in 4 jet events for different production mechanisms. Going from left to right, figures show: all events, events with flavor excitation $Q\bar{Q}$ production, events with direct $Q\bar{Q}$ and events with gluon splitting $Q\bar{Q}$ production. From top to bottom, ΔR_{bb}, $\Delta\phi_{bb}$, M_{bb} and p_{bb}^T distributions are shown.*

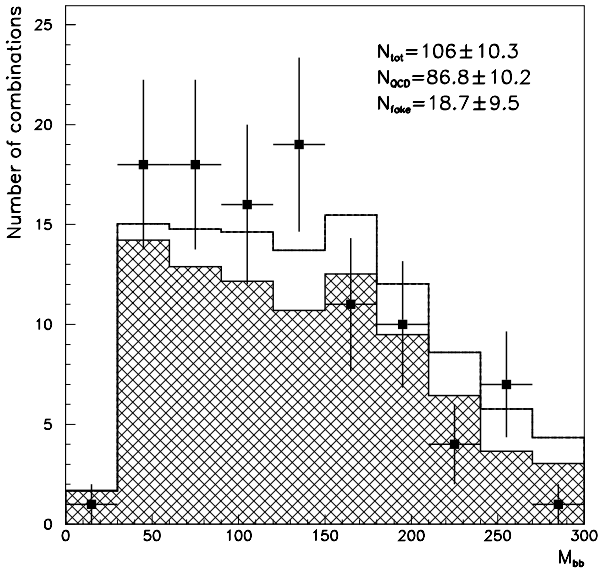

Figure 6-5: *Fit of double tagged combinations observed in data events with 4 jets to a sum of QCD (hatched) and Fakes (white) after the* $\Sigma E_T \geq 300$ *GeV requirement. The normalization of the Fakes has been fixed to the number observed allowing for statistical fluctuations. The results of the fit are shown in the figure.*

has been determined using the method based on jet tagging rates, as described in the previous chapter. The fit χ^2 per degree of freedom is 1.3. This implies that the kinematical distributions of the heavy flavor quark pairs in the QCD Monte Carlo model the data reasonably well, since the kinematical distributions of the fake double tagged combinations have already been shown to be in agreement with the data in chapter 5. The normalization of the fake double tagged combinations has been fixed to the number observed in the data, allowing them to fluctuate within their statistical uncertainties in the fit.

6.4.2 Calculation of the expected QCD background

Having demonstrated that our simulation of QCD multijets agrees well with the QCD rich data, we use the simulation to calculate the expected number of double tagged combinations from QCD multijets in events with ≥ 5 jets that consitute our final data sample. The calculation of the expected QCD background proceeds in two

steps. First, the QCD Monte Carlo is scaled to properly reproduce the jet multiplicity distribution of data rich in QCD b jets i.e. events with ≥ 1 b-tags after accounting for mistags. With the shape of the jet multiplicity distribution thus determined from events with one b-tag, the Monte Carlo can be used to predict the QCD background in all jet multiplicities for events with ≥ 2 b-tags, as long as the absolute QCD cross section is known. To obtain this cross section, we use events with four jets and ≥ 2 b-tags. As the second step, the absolute prediction of the QCD Monte Carlo is normalized to the total number of such events after accounting for mistags. Using this normalization and the shape of the jet multiplicity distribution of the scaled Monte Carlo, the number of expected QCD heavy flavor events with ≥ 2 b-tags can be determined.

A small correction to the normalization arises from the presence of $t\bar{t}$ decays in four jet events. To account for this, the calculated QCD contribution in four or more jet events is iteratively adjusted to account for the presence of a $t\bar{t}$ component in 4-jet events. This is done by using the excess in five or more jet events (over QCD and mistags) and the jet multiplicity distribution of ≥ 2 b-tagged events derived from a $t\bar{t}$ Monte Carlo.

Table 6.7 gives the definitions of the variables used to calculate the expected number of double tagged combinations in data from QCD. The index k indicates the jet multiplicity of the event. Our objective is to calculate the number of double tagged combinations in the data from QCD for each jet mutliplicity, $N^{2c}_{data,QCD}(k)$.

In order to simplify the notation, the following are defined:

- The number of net positive tagged jets in the data after accounting for fake tags, $x_i \equiv \{N^{\geq 1}_{data}(i) - N^{\geq 1}_{data,fake}(i)\}$. These are also referred to as "QCD tags".

- The number of net positive double-tagged combinations in data after accounting for fake combinations, $y_i \equiv \{N^{2c}_{data}(i) - N^{2c}_{data,fake}(i)\}$.

- The ratio of the number of double-tagged combinations to the number of tagged jets relative to events with 4 jets in the QCD Monte Carlo, $K_i \equiv \frac{N^{2c}_{QCD}(i)}{N^{2c}_{QCD}(4)} \frac{N^{\geq 1}_{QCD}(4)}{N^{\geq 1}_{QCD}(i)}$.

Variable	Definition
$N^{\geq 1}_{data}(k)$	Positive b-tags in data
$N^{2c}_{data}(k)$	Double b-tagged combinations in data
$N^{\geq 1}_{data,fake}(k)$	Negative b-tags in data
$N^{2c}_{data,fake}(k)$	Fake double b-tagged combinations in data
$N^{\geq 1}_{data,t\bar{t}}(k)$	Positive b-tags in data from $t\bar{t}$
$N^{2c}_{data,t\bar{t}}(k)$	Double b-tagged combinations in data from $t\bar{t}$
$N^{\geq 1}_{data,QCD}(k)$	Positive b-tags in data from QCD
$N^{2c}_{data,QCD}(k)$	Double b-tagged combinations in data from QCD
$N^{\geq 1}_{QCD}(k)$	Positive b-tags in QCD Monte Carlo
$N^{2c}_{QCD}(k)$	Double b-tagged combinations in QCD Monte Carlo
$N^{\geq 1}_{t\bar{t}}(k)$	Positive b-tags in $t\bar{t}$ Monte Carlo
$N^{2c}_{t\bar{t}}(k)$	Double b-tagged combinations in $t\bar{t}$ Monte Carlo

Table 6.7: Definition of the variables used in the QCD normalization calculation. The index k indicates the jet multiplicity of the event.

- The ratio of the number of tagged jets to the number of double-tagged combinations in the $t\bar{t}$ Monte Carlo, $\gamma_i \equiv N^{\geq 1}_{t\bar{t}}(i)/N^{2c}_{t\bar{t}}(i)$.
- The ratio of the number of double-tagged combinations in 4-jet events to the i-jet events in the $t\bar{t}$ Monte Carlo, $\lambda_i \equiv N^{2c}_{t\bar{t}}(4)/N^{2c}_{t\bar{t}}(i)$.

The number of b-tags from QCD production in events with i jets (QCD tags) is given by $\{x_i - \gamma_i N^{2c}_{data,t\bar{t}}(i)\}$. To tune the jet multiplicity distribution of the QCD Monte Carlo, the ratio of QCD tags in Monte Carlo and data, a_i, is considered.

$$a_i = \frac{N^{\geq 1}_{QCD}(i)}{x_i - \gamma_i N^{2c}_{data,t\bar{t}}(i)}$$

The ratio a_i should be a constant equal to $\frac{(\int \mathcal{L}dt)_{QCD\ MC}}{(\int \mathcal{L}dt)_{data}}$ across different jet multiplicities (i.e. different i's) if the Monte Carlo properly simulates the jet multiplicity distributions of QCD production. Here $(\int \mathcal{L}dt)_{QCD\ MC}$ is the integrated luminosity of

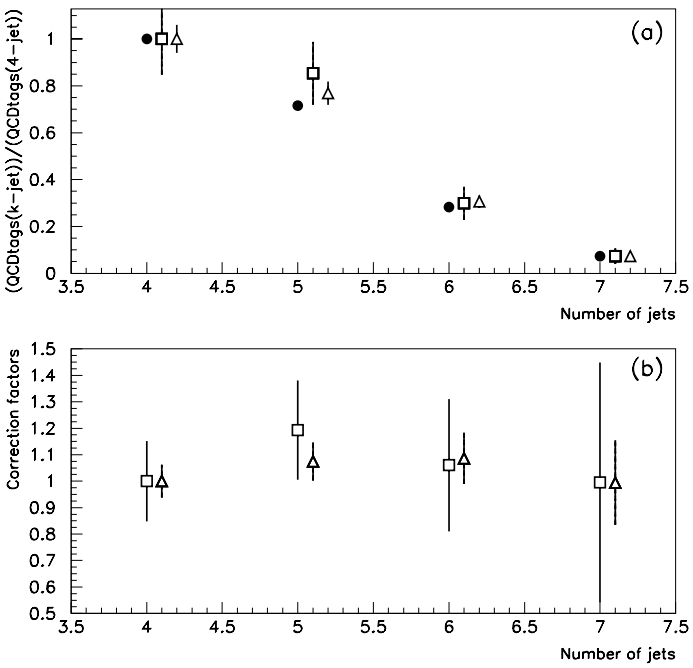

Figure 6-6: *Upper plot (a) shows a comparison of jet multiplicity distributions of "QCD tags" for QCD MC (dots), 1A data (squares) and 1B data (triangles). Lower plot (b) shows the correction factors for run 1A (squares) and 1B data (triangles).*

the generated QCD Monte Carlo sample and $(\int \mathcal{L}dt)_{data}$ is the integrated luminosity of Run 1 data. Defining $\alpha_i \equiv \frac{a_i}{a_4}$, the correction factors relative to 4-jet events, α_i^{-1}, can be obtained. Figure 6-6(a) shows a comparison of the jet multiplicity distributions of QCD tags in QCD Monte Carlo and data. Figure 6-6(b) shows the correction factors α_i^{-1} that are applied to make the Monte Carlo jet multiplicity distribution agree with the data. Using these correction factors, we determine β_i which is the ratio of the corrected number of double tagged combinations in QCD Monte Carlo events with i jets to events with 4 jets.

$$\beta_i \equiv \frac{N^{2c}_{QCD}(i)}{N^{2c}_{QCD}(4)}\frac{\alpha_4}{\alpha_i} = \frac{N^{2c}_{QCD}(i)}{N^{2c}_{QCD}(4)}\frac{1}{\alpha_i} \equiv K_i \left(\frac{x_i - \gamma_i N^{2c}_{data,t\bar{t}}(i)}{x_4 - \gamma_4 N^{2c}_{data,t\bar{t}}(4)} \right)$$

The number of double tagged combinations in the data from QCD is the number of double tagged combinations from QCD observed in 4-jet events scaled by the factor

β_i. Therefore, the number from QCD is given by:

$$N^{2c}_{data,QCD}(i) = \beta_i\{y_4 - N^{2c}_{data,t\bar{t}}(4)\} = K_i\left(\frac{x_i - \gamma_i N^{2c}_{data,t\bar{t}}(i)}{x_4 - \gamma_4 N^{2c}_{data,t\bar{t}}(4)}\right)\{y_4 - N^{2c}_{data,t\bar{t}}(4)\}$$

The number of double tagged combinations in data from $t\bar{t}$ is now given by the total number of double tagged combinations observed in data minus the number from fakes and QCD.

$$N^{2c}_{data,t\bar{t}}(i) = y_i - N^{2c}_{data,QCD}(i) = y_i - K_i\left(\frac{x_i - \gamma_i N^{2c}_{data,t\bar{t}}(i)}{x_4 - \gamma_4 N^{2c}_{data,t\bar{t}}(4)}\right)(y_4 - N^{2c}_{data,t\bar{t}}(4))$$

Rewriting:

$$N^{2c}_{data,t\bar{t}}(i) = \frac{y_i(x_4 - \gamma_4\overline{N^{2c}_{data,t\bar{t}}(4)}) - K_i x_i(y_4 - \overline{N^{2c}_{data,t\bar{t}}(4)})}{(x_4 - \gamma_4\overline{N^{2c}_{data,t\bar{t}}(4)}) - K_i\gamma_i(y_4 - \overline{N^{2c}_{data,t\bar{t}}(4)})}$$

Where, $\overline{N^{2c}_{data,t\bar{t}}(4)} \equiv \frac{1}{3}\sum_{5,6,7}\lambda_i N^{2c}_{data,t\bar{t}}(i)$ is the mean number of combinations in 4-jet events from $t\bar{t}$ production. The result is iterated till convergence and the final values of $N^{2c}_{data,t\bar{t}}(i)$ are used to calculate the number of double tagged combinations from QCD.

The sources of systematic uncertainty in the predicted QCD normalization are the uncertainty in radiation modelling, the uncertainty in fragmentation modelling, the uncertainty in the jet energy scale and the uncertainty in the b-tagging scale factor. The fractional uncertainty due to radiation modelling, fragmentation modelling and b-tagging is the same for different jet multiplicities, while the effect of jet energy scale varies for different jet multiplicities. Since K_i and γ_i are ratios, most of the systematic effects cancel. Therefore, the uncertainty in the predicted QCD normalization is predominantly statistical.

The calculation is performed separately for Run 1A and 1B. The results are summarized in table 6.8.

6.5 Summary

It is seen that the expected number of ≥ 2 b tagged events from all processes except for QCD and Fakes is small. Since the uncertainty in the QCD normalization is larger

$\Sigma E_T \geq 300$ GeV	$N_{jet} = 4$	$N_{jet} = 5$	$N_{jet} = 6$	$N_{jet} \geq 7$
N_{QCD} (1A)	12.9±2.6	10.6±2.3	4.2±1.1	1.3±0.5
N_{QCD} (1B)	60.5±12.0	49.3±10.8	19.7±5.2	5.9±2.2

Table 6.8: Number of real and fake double tagged combinations expected from QCD for Runs 1A and 1B.

than the total number of events from other non-fake and non-$t\bar{t}$ sources, only fakes and QCD are considered to be the background sources in this analysis. In the next chapter, we will compare our total background expectation with the number of double tagged combinations observed in the data.

Chapter 7

The $t\bar{t}$ production cross-section

This chapter describes the isolation of a $t\bar{t}$ signal and a measurement of the $t\bar{t}$ production cross-section using events with at least 5 jets including at least two b-tagged jets and a total transverse energy greater than 300 GeV. The two sources of background in this sample are mistags and QCD multijet production of $b\bar{b}/c\bar{c}$ pairs. Their contributions have been calculated in chapters 5 and 6 respectively. An excess of double tagged combinations over the background expectation is seen in ≥ 5 jet events. Taking the excess to be from $t\bar{t}$ production, a likelihood method is used to measure the cross-section.

In order to further discriminate between the QCD and $t\bar{t}$ production of $b\bar{b}/c\bar{c}$ pairs, additional kinematic variables are investigated. The variables that are found to be the most discriminating are the difference in the azimuth of the tagged jets ($\Delta\phi_{b\bar{b}}$), their separation in $\eta - \phi$ space ($\Delta R_{b\bar{b}}$) and their invariant mass ($M_{b\bar{b}}$). Accounting for the correlations between these variables, we again use a likelihood method to measure the $t\bar{t}$ production cross-section with a reduced total uncertainty. The additional sources of systematic uncertainty from the usage of these kinematic variables are studied and the significance of the measurement is calculated.

$\Sigma E_T \geq 300$ GeV	$N_{jet} = 4$	$N_{jet} = 5$	$N_{jet} = 6$	$N_{jet} \geq 7$
N_{obs} (1A)	21	13	12	2
N_{mistag} (1A)	10	3	1	1
N_{QCD} (1A)	12.9±2.6	10.6±2.3	4.2±1.1	1.3±0.5
N_{obs} (1B)	85	96	38	11
N_{mistag} (1B)	19	23	11	0
N_{QCD} (1B)	60.5±12.0	49.3±10.8	19.7±5.2	5.9±2.2

Table 7.1: A summary of the number of double tagged combinations observed in the data (N_{obs}), the number expected from QCD (N_{QCD}) and the number expected from mistags (N_{mistag}). The numbers are shown for Runs 1A and 1B separately.

7.1 A Summary of Data and Backgrounds

The number of observed double tagged combinations, the number of observed mistag combinations and the number of expected double tagged combinations from QCD are summarized in table 7.1 for Runs 1A and 1B. The total integrated luminosities for the two data taking periods are 19.3 ± 0.68 pb^{-1} and 90.1 ± 7.21 pb^{-1} respectively. It is seen that there is an excess of observed double tagged combinations over the expected background from QCD and mistags in events with five or more jets. Since, we have already seen that the contribution of other physics background sources is negligible, we attribute the excess entirely to $t\bar{t}$ production, and use it to calculate the production cross-section. In order to evaluate the cross-section, we need to calculate the total acceptance for $t\bar{t}$ decays. This is addressed in the next section.

7.2 Total acceptance for $t\bar{t}$ decays

The total acceptance is defined as the fraction of the number of $t\bar{t}$ events generated that pass all the requirements of the analysis. The total acceptance for a k-jet event,

	$N_{jet} = 4$	$N_{jet} = 5$	$N_{jet} = 6$	$N_{jet} \geq 7$
ϵ_{sample} (%)	17.7±0.2	23.1±0.3	12.6±0.2	3.8±0.1
$\epsilon_{\Sigma E_T}$ (%)	30.0±0.8	57.3±1.0	79.6±1.8	93.2±3.6
ϵ_{comb} (1A %)	6.5±5.5	7.1±6.1	7.7±6.6	7.6±6.5
ϵ_{comb} (1B %)	11.5±5.3	12.5±5.8	13.7±6.3	13.3±6.2

Table 7.2: Summary of the efficiencies for passing the final sample selection and the $\Sigma E_T \geq 300$ GeV requirements in $t\bar{t}$ decays for a top quark of mass 175 GeV/c^2. Efficiencies for observing ≥ 2 b-tagged events and ≥ 1 double tagged combinations are also given.

α^k_{tot} is given by:

$$\alpha^k_{tot} = \epsilon_{sample} \cdot \epsilon_{\Sigma E_T} \cdot \epsilon_{comb}$$

The efficiencies for passing the final sample selection (ϵ_{sample}), the ΣE_T ($\epsilon_{\Sigma E_T}$) and the b-tagging (ϵ_{comb}) requirements have already been discussed in chapters 4 and 5. For reference they are summarized in table 7.2. The uncertainties quoted for ϵ_{sample} and $\epsilon_{\Sigma E_T}$ are statistical only while the uncertainty in ϵ_{comb} includes the systematic uncertainty from the Monte Carlo to data scale factor.

The primary sources of systematic uncertainty in ϵ_{sample} are the Monte Carlo modelling of gluon radiation ($\Delta_{rad} = 8\%$), the Monte Carlo modelling of fragmentation ($\Delta_{frag} = 6.5\%$) and the uncertainty in the jet energies (see table 4.7). The uncertainty due to b-tagging comes from the uncertainty in the scale factors for Runs 1A and 1B. As explained in chapter 5, due to the cubic dependence of the number of double tagged combinations seen in the $t\bar{t}$ Monte Carlo on the scale factor, the uncertainties (29.2% for 1A and 7% for 1B) are multiplied by a factor of 3. The uncertainty from b-tagging is 87.5% (21%) for Run 1A (1B).

Tables 7.3 and 7.4 summarize the total acceptance for this analysis for different jet multiplicities for Run 1A and 1B respectively. The uncertainties from different systematic effects are also shown separately.

Run 1A	$N_{jet} = 4$	$N_{jet} = 5$	$N_{jet} = 6$	$N_{jet} \geq 7$	$N_{jet} \geq 5$
α_{tot} (%)	0.35	0.94	0.78	0.27	2.34
	$\pm$0.03 (rad)	$\pm$0.08 (rad)	$\pm$0.06 (rad)	$\pm$0.02 (rad)	$\pm$0.19 (rad)
	$\pm$0.02 (gen)	$\pm$0.06 (gen)	$\pm$0.05 (gen)	$\pm$0.02 (gen)	$\pm$0.15 (gen)
	$\pm$0.03 (jet)	$\pm$0.01 (jet)	$\pm$0.05 (jet)	$\pm$0.04 (jet)	$\pm$0.13 (jet)
	$\pm$0.31 (tag)	$\pm$0.82 (tag)	$\pm$0.68 (tag)	$\pm$0.24 (tag)	$\pm$1.14 (tag)
α_{tot} (%)	0.35$\pm$0.32	0.94$\pm$0.83	0.78$\pm$0.69	0.27$\pm$0.25	2.34$\pm$1.17

Table 7.3: Total acceptance for a top quark of mass 175 GeV/c^2 for Run 1A.

Run 1B	$N_{jet} = 4$	$N_{jet} = 5$	$N_{jet} = 6$	$N_{jet} \geq 7$	$N_{jet} \geq 5$
α_{tot} (%)	0.61	1.66	1.37	0.47	4.11
	$\pm$0.05 (rad)	$\pm$0.13 (rad)	$\pm$0.11 (rad)	$\pm$0.04 (rad)	$\pm$0.33 (rad)
	$\pm$0.04 (gen)	$\pm$0.11 (gen)	$\pm$0.09 (gen)	$\pm$0.03 (gen)	$\pm$0.27 (gen)
	$\pm$0.05 (jet)	$\pm$0.01 (jet)	$\pm$0.09 (jet)	$\pm$0.08 (jet)	$\pm$0.23 (jet)
	$\pm$0.13 (tag)	$\pm$0.35 (tag)	$\pm$0.29 (tag)	$\pm$0.10 (tag)	$\pm$0.48 (tag)
α_{tot} (%)	0.61$\pm$0.18	1.66$\pm$0.43	1.37$\pm$0.37	0.47$\pm$0.16	4.11$\pm$0.68

Table 7.4: Total acceptance for a top quark of mass 175 GeV/c^2 for Run 1B.

7.3 A preliminary determination of the cross-section

Using the excess observed in ≥ 5 jet events and the total acceptance, the $t\bar{t}$ production cross-section can be measured. However, as mentioned earlier, the total acceptance has both correlated and uncorrelated parts across different jet multiplicities. In addition, the uncertainty in the QCD background expectation is fully correlated across different jet multiplicities due to the method of its calculation. All these cor-

relations need to be taken into account in order to calculate the uncertainty in the cross-section. As an initial approach, the number of combinations from $t\bar{t}$ and their production cross-section is calculated in a straight-forward fashion using the number of background combinations $N_{bkg} \equiv N_{mistag} + N_{QCD}$:

$$\sigma_{t\bar{t}} = \frac{N_{obs} - N_{bkg}}{\epsilon_{tot} \cdot \int \mathcal{L} dt}$$

The total uncertainty in the cross-section is calculated using estimates of the systematic uncertainties in the acceptance and the background normalization. This method is being presented mainly to provide the reader with an estimate of the number of combinations from $t\bar{t}$, their production cross-section and their respective uncertainties.

In the data, 172 double tagged combinations are observed (N_{obs}). To take into account the correlations, the uncertainties in the QCD background for each jet multiplicity bin are summed linearly to get the total uncertainty in N_{QCD}. The number of combinations from QCD are 16.1 ± 3.9 and 74.9 ± 18.2 for Run 1A and 1B respectively. The number of combinations from mistags are uncorrelated across different jet multiplicities and therefore their uncertainties are summed in quadrature. Taking the QCD background to be uncorrelated between Run 1A and 1B, the total background (N_{bkg}) is determined to be 130.0 ± 19.6. Therefore, the number of combinations from $t\bar{t}$ is 42 ± 23.6. The combined acceptance for Run 1A and 1B is determined by taking an integrated luminosity weighted average of the two individual acceptances, and is determined to be 0.0321 ± 0.0085. Using these numbers we get a production cross-section of $12.0^{+9.3}_{-7.3}$ pb.

The jet multiplicity distribution of the data is an additional piece of information that can be used. The $t\bar{t}$ production cross-sections are calculated for each jet multiplicity and combined by taking their average. All systematic uncertainties are added linearly and all statistical uncertainties are added in quadrature. This method clearly over-estimates the total systematic uncertainty. The individual cross-sections for each jet multiplicity and the combined cross-section is summarized in table 7.5.

N_{jet}	Cross-section (pb)
5	13.1±9.0(stat)±7.5(syst)
6	8.8±6.6(stat)±4.7(syst)
7	13.5±10.2(stat)±6.6(syst)
≥5	11.8±5.0(stat)±6.3(syst)

Table 7.5: A cross-check of the cross-section calculation using the N_{jet} distribution.

7.4 Likelihood Method I

In order to calculate the $t\bar{t}$ cross-section in ≥ 5 jet events, an binned likelihood fit is performed to combine the cross-sections in individual jet multiplicity bins. Using the fit, the correlated systematic uncertainties between different jet multiplicity bins can be properly taken into account. The likelihood function has a separate term for each jet multiplicity. In addition, Run 1A and 1B data are treated separately because of their different acceptances. For each jet multiplicity bin, the number of fit combinations from QCD and mistags are constrained to the number calculated and observed in the data respectively. However, they are allowed to vary within their total uncertainties. By imposing a constraint that for each jet multiplicity, the number of combinations returned by the fit for QCD, mistags and $t\bar{t}$ sum to the number observed in the data, the $t\bar{t}$ production cross-section can be measured. This is because the number of observed double tagged combinations in any jet multiplicity bin (N_k^{data}) can be written in terms of the number of double tagged combinations from QCD and mistags as:

$$\begin{aligned} N_k^{data} &= N_k^{t\bar{t}} + N_k^{QCD} + N_k^{mistag} \\ &= \epsilon_{tot} \cdot \sigma_{t\bar{t}} \cdot \int \mathcal{L}dt + N_k^{QCD} + N_k^{mistag} \end{aligned}$$

Here ϵ_{tot} is the total acceptance for a given jet multiplicity, $\sigma_{t\bar{t}}$ is the $t\bar{t}$ production cross-section and $\int \mathcal{L}dt$ is the integrated luminosity. The uncorrelated uncertainties in the total acceptance are taken to be Gaussian distributed, and appropriate terms are

included in the likelihood function. Finally, there is an uncertainty in the integrated luminosity, for both periods of data taking, which is taken to be Gaussian distributed. The likelihood function for Run 1A and 1B data is given by:

$$
\begin{aligned}
L &= \prod_{k=5}^{\geq 7} (L_k^{QCD} \cdot L_k^{mistag} \cdot L_k^{t\bar{t}}) \cdot L_{\int \mathcal{L} dt} \\
L_k^{QCD} &= P(N_k^{QCD/1A}; \overline{N_k^{QCD/1A}}) \cdot P(N_k^{QCD/1B}; \overline{N_k^{QCD/1B}}) \\
L_k^{mistag} &= P(N_k^{mistag/1A}; \overline{N_k^{mistag/1A}}) \cdot P(N_k^{mistag/1B}; \overline{N_k^{mistag/1B}}) \\
L_k^{t\bar{t}} &= G(\epsilon_k^{1A}; \overline{\epsilon_k{}^{1A}}, \sigma_{\overline{\epsilon_k{}^{1A}}}) \cdot P(N_k^{data/1A}; \epsilon_k^{1A} \sigma_{t\bar{t}} \int \mathcal{L}_{1A} dt + \overline{N_k^{mistag/1A}} + \overline{N_k^{QCD/1A}}) \\
&\quad G(\epsilon_k^{1B}; \overline{\epsilon_k{}^{1B}}, \sigma_{\overline{\epsilon_k{}^{1B}}}) \cdot P(N_k^{data/1B}; \epsilon_k^{1B} \sigma_{t\bar{t}} \int \mathcal{L}_{1B} dt + \overline{N_k^{mistag/1B}} + \overline{N_k^{QCD/1B}}) \\
L_{\int \mathcal{L} dt} &= G(\int \mathcal{L}_{1A} dt; \overline{\int \mathcal{L}_{1A} dt}, \sigma_{\int \mathcal{L}_{1A} dt}) \cdot G(\int \mathcal{L}_{1B} dt; \overline{\int \mathcal{L}_{1B} dt}, \sigma_{\int \mathcal{L}_{1B} dt})
\end{aligned}
$$

$P(n;\mu)$ is a Poisson distribution with a mean μ and observation n. $G(x;\bar{x},\sigma_x)$ is a Gaussian distribution with a mean $\bar{x}$ and standard deviation σ_x.

- The L_k^{QCD} term constrains the fit QCD normalization of a k jet event, $\overline{N_k^{QCD}}$, to the number expected N_k^{QCD}. For each jet multiplicity, separately for Runs 1A and 1B, the fit QCD normalization is written as $\overline{N_k^{QCD}} \equiv \alpha_k N_k^{data}$ where α_k is the fraction of total double tagged combinations that are from QCD.

- The L_k^{mistag} term constrains the mistag normalization of a k jet event, $\overline{N_k^{mistag}}$, to the expected number N_k^{mistag}. For each jet multiplicity, separately for Run 1A and 1B, the fit mistag normalization is written as $\overline{N_k^{mistag}} \equiv (1-\alpha_k)\beta_k N_k^{data}$. Here $(1-\alpha_k)\beta_k$ is the fraction of total double tagged combinations that are from mistags.

- The $L_k^{t\bar{t}}$ term measures the $t\bar{t}$ production cross-section by constraining the total number of combinations in each jet multiplicity bin, after the fit for individual contributions from QCD and mistags, to the number observed. The two measurements from Runs 1A and 1B are taken to be independent of each other. The fraction of double tagged combinations from $t\bar{t}$ is $(1-\alpha_k)(1-\beta_k)$. The Gaussian terms for the total acceptances for Run 1A and 1B, constrain the fit

total acceptances for each jet multiplicity (ϵ_k) to the input acceptances ($\overline{\epsilon_k}$) allowing for their total uncorrelated uncertainties ($\sigma_{\overline{\epsilon_k}}$).

- Finally, the $L_{\int \mathcal{L}dt}$ term takes into account the uncertainty in the integrated luminosity.

The fit parameters in the likelihood function are α_i, β_i, ϵ_i ($i = 5, 6, \geq 7$ for 1A and 1B data), $\sigma_{t\bar{t}}$ ($t\bar{t}$ production cross-section) and the integrated luminosities of Run 1A and 1B, for a total of 21. The likelihood function is maximized using the MINUIT[59] fitting package.

7.4.1 Systematic Uncertainties in the cross-section

The sources of systematic uncertainties in the measurement of the cross-section are the uncertainties in the total acceptance, QCD normalization and integrated luminosity. The correlations between the different systematic effects are taken into account by repeating the likelihood fit multiple times while varying individual systematic effects independently within their uncertainties every time.

To take into account the uncertainty in the QCD normalization, the QCD normalization is varied in a completely correlated fashion across different jet multiplicity bins. Every time the fit is performed, a random number x is chosen from a normal distribution. The calculated QCD normalizations for a given data taking run are then simultaneously varied for all jet multiplicities by $x \cdot \delta N_k^{QCD}$, where δN_k^{QCD} is the uncertainty in the calculated QCD normalization for an event with k jets. The fit QCD normalization, $\overline{N_k^{QCD}}$, is then constrained to $N_k^{QCD} + x \cdot \delta N_k^{QCD}$ in the L_k^{QCD} term. Different random numbers are chosen for the two data taking runs.

To take into account the effect of radiation modelling, fragmentation modelling and the jet energy scale, the total acceptances for Run 1A and 1B are varied separately. Every time the fit is performed, three normally distributed random numbers (x, y and z) are chosen for a given data taking run, say Run 1A. The input acceptance used in the $L_k^{t\bar{t}}$ term to constrain ϵ_k^{1A} is then given by:

$$\overline{\epsilon_k^{1A}} \cdot (1 + x\Delta_{rad}) \cdot (1 + y\Delta_{frag}) \cdot (1 + a_0 + za_1)$$

As described earlier in chapter 4, a_0 and a_1 are the parameters used to determine the variation of ϵ_{sample} with a changing energy scale. A similar procedure is followed for Run 1B.

The motivation behind using multiple likelihood fits to determine the uncertainties from correlated systematic effects is the following. The i^{th} individual fit returns, for each fit parameter ξ, a value ξ_i, and a *statistical* uncertainty $\delta\xi_i$ calculated using the shape of the likelihood function. When the fits are repeated multiple times, with varying input parameters, both ξ_i and $\delta\xi_i$ will be distributed over a range of values. We need to determine the mean of the ξ_i distribution ($\bar{\xi}$) and its total systematic ($\overline{\delta\xi}_{sys}$) and statistical ($\overline{\delta\xi}_{stat}$) uncertainties.

The value of the fit parameter ξ_i is Gaussian distributed where the mean of the distribution is the required value, $\bar{\xi}$. Its standard deviation is the uncertainty in $\bar{\xi}$ due to *systematic* effects, $\delta\bar{\xi}$. The mean of the distribution of $\delta\xi_i$, $\overline{\delta\xi}$, is the sum in quadrature of uncertainties from *both* statistical and systematic sources, $(\overline{\delta\xi}_{stat} \oplus \overline{\delta\xi}_{sys1})$, where $\overline{\delta\xi}_{sys1}$ is the systematic contribution in addition to $\bar{\xi}$. The total uncertainty is therefore given by the sum in quadrature $(\delta\bar{\xi} \oplus \overline{\delta\xi})$. The statistical uncertainty $\overline{\delta\xi}_{stat}$ is determined by performing the likelihood fit using just the statistical uncertainties in the parameters and keeping all the systematic effects fixed. It follows that the uncertainty due to systematic effects is given by $(\overline{\delta\xi}_{sys} \equiv \delta\bar{\xi} \oplus \overline{\delta\xi} \ominus \overline{\delta\xi}_{stat})$.

This is essentially a Bayesian method for the handling of systematic uncertainties. A Bayesian approach to systematic uncertainties is discussed elsewhere [60]. If $\vec{x} = \{x_1, \cdots, x_n\}$ is a vector of observables, $\vec{\mu} = \{\mu_1, \cdots, \mu_n\}$ is a vector of the true values of the observables and $\vec{h} = \{h_1, \cdots, h_n\}$ is a vector of the *influence* (systematic) variables, then the distribution of $\vec{\mu}$ given $\vec{x}$, for all possible $\vec{h}$, is given by:

$$f(\vec{\mu}|\vec{x}) \quad = \quad \frac{\int f(\vec{x}|\vec{\mu},\vec{h}) f(\vec{\mu},\vec{h}) d\vec{h}}{\int\int f(\vec{x}|\vec{\mu},\vec{h}) f(\vec{\mu},\vec{h}) d\vec{\mu} d\vec{h}}$$

Performing the likelihood fits multiple times is equivalent to the integral in the numerator, since the systematic variables are being varied over their entire range of possible values. The denominator determines the overall normalization.

Therefore, the likelihood fit is repeated 1000 times, varying each of the systematic

effects within their uncertainties as described above. This results in certain distributions of the fit parameters and their total uncertainties. The statistical uncertainties in the fit parameters can be determined by performing the likelihood fit while keeping the systematic effects fixed.

7.4.2 The $t\bar{t}$ signal

The likelihood fit returns the values of fit parameters α_i and β_i for Run 1A and 1B. Every time the likelihood fit is performed, the error matrix is calculated. In the calculation of the uncertainty in a quantity $G(x_1, \cdots, x_n)$, correlations between different x_i can be taken into account by using the error matrix, $\sigma^2_{x_i x_j}$:

$$\Delta G = \sqrt{\sum_i \sum_j \frac{\partial G}{\partial x_i} \frac{\partial G}{\partial x_j} \sigma^2_{x_i x_j}}$$

Using the expressions for the number of combinations from QCD, mistags or $t\bar{t}$ in terms of α_i and β_i, the number of combinations from each process and their uncertainties are determined. The results are summarized in table 7.6.

In the combined Run 1A and 1B data, we observe a signal of 42.4 ± 20.3 combinations over a background of 129.6 ± 20.6. Separately we observe 5.9 ± 3.9 (21.1 ± 4.5) and 36.5 ± 18.9 (108.5 ± 19.1) signal (background) combinations in Run 1A and 1B respectively. The table also shows the result of the likelihood fit to 4-jet events. As expected, they are consistent with a sum of QCD and mistags only.

The number of events with ≥ 2 b-tags is calculated from the number of double tagged combinations using conversion factors derived from Monte Carlos for QCD and $t\bar{t}$. These conversion factors are the ratios of the number of events with ≥ 2 b-tags to the number of double tagged combinations for each jet multiplicity bin of each process. The numbers of events are summarized in table 7.7. In Run 1A and 1B data combined, we observe a signal of 37.5 ± 16.9 events over a background of 119.5 ± 17.9. Separately we observe 5.9 ± 3.9 (21.1 ± 4.5) and 31.6 ± 16.4 (98.4 ± 17.3) signal (background) events in Run 1A and 1B respectively.

Run I	$N_{jet} = 4$	$N_{jet} = 5$	$N_{jet} = 6$	$N_{jet} \geq 7$	Total ($N_{jet} \geq 5$)
N_{2c}^{data}	106	109	50	13	172
N_{2c}^{QCD}	73.7±8.7	60.1±12.1	23.8±7.3	6.9±3.8	90.8±19.6
N_{2c}^{mistag}	27.8±5.2	26.5±5.1	11.6±3.9	0.8±1.5	38.9±6.4
N_{2c}^{bkgd}	101.4±10.1	86.5±12.8	35.4±8.2	7.7±3.9	129.6±20.6
$N_{2c}^{t\bar{t}}$	4.6±7.2	22.5±12.5	14.6±7.9	5.3±3.7	42.4±20.3

Table 7.6: Fit results for Run 1A and 1B. The table shows the total number of double tagged *combinations* observed in data, and the number of double tagged combinations from QCD, Mistag and $t\bar{t}$ returned by the fit. The signal region is $N_{jet} \geq 5$. For reference, the results of the fit to 4-jet events are also shown.

Run I	$N_{jet} = 4$	$N_{jet} = 5$	$N_{jet} = 6$	$N_{jet} \geq 7$	Total ($N_{jet} \geq 5$)
N_{2b}^{data}	95	102	42	13	157
N_{2b}^{QCD}	71.5±8.4	59.1±11.7	21.9±6.4	5.5±3.0	84.5±17.5
N_{2b}^{mistag}	19.4±3.6	25.7±5.4	7.2±2.5	2.2±1.5	35.0±5.8
N_{2b}^{bkgd}	90.9±9.1	82.8±12.3	29.0±6.1	7.7±3.8	119.5±17.9
$N_{2b}^{t\bar{t}}$	4.1±6.5	19.2±10.8	13.0±6.2	5.3±3.7	37.5±16.8

Table 7.7: Fit results for Run 1A and 1B. The table shows the total number of ≥ 2 b-tagged *events* observed in data, and the number of ≥ 2 b-tagged events from QCD, Mistag and $t\bar{t}$ returned by the fit. The signal region is $N_{jet} \geq 5$. For reference, the results of the fit to 4-jet events are also shown.

7.4.3 The $t\bar{t}$ production cross-section

The distribution of the $t\bar{t}$ production cross-section after 1000 likelihood fits is shown in figure 7-1. The distributions of the asymmetric uncertainties in the cross-section returned by the fit are also shown. The fit cross-section is $11.7^{+7.9}_{-7.2}$ pb. The total positive (negative) uncertainty is given by the sum in quadrature of the one standard deviation width of the cross-section distribution and the mean value of the distribution of its positive (negative) uncertainty. When the same fit is repeated after turning off all the contributions from systematic effects, the fit cross-section is $10.7^{+4.8}_{-4.6}$ pb. As mentioned earlier, this uncertainty is purely statistical. Using this relative statistical uncertainty of 44%, the total uncertainty in the combined cross-section can be broken down into its statistical and systematic components. The combined cross-section is measured to be $11.7 \pm 5.1(stat)^{+6.0}_{-5.1}(syst)$ pb from double-tagged combinations.

The individual contributions of the different sources of systematic uncertainty are determined in the following fashion. Keeping all the others fixed, each source is varied by its one standard deviation uncertainty. The total systematic uncertainty in the cross-section is determined, and the fractional contribution of each source is calculated. Table 7.8 summarizes the contributions of each source.

7.5 Kinematical Shapes for QCD and $t\bar{t}$ processes

Additional discrimination between double tagged combinations from QCD and $t\bar{t}$ can be achieved by studying their kinematical properties. The kinematical variables that are considered are the separation in $\eta - \phi$ space of the two b-tagged jets ($\Delta R_{b\bar{b}}$), their separation in azimuth ($\Delta\phi_{b\bar{b}}$), their invariant mass ($M_{b\bar{b}}$), their combined transverse momentum ($p^T_{b\bar{b}}$), their separation in η ($\Delta\eta_{b\bar{b}}$), the scalar difference in their transverse energies ($|E^T_b - E^T_{\bar{b}}|$) and the scalar sum of their transverse energies ($E^T_b + E^T_{\bar{b}}$).

In order to discriminate a process $,_i$ from another process $,_j$, where the normalized distributions of a variable α are given by $P^i(\alpha)$ and $P^j(\alpha)$ for $,_i$ and $,_j$ respectively, the most discriminating variables can be chosen by performing a binned

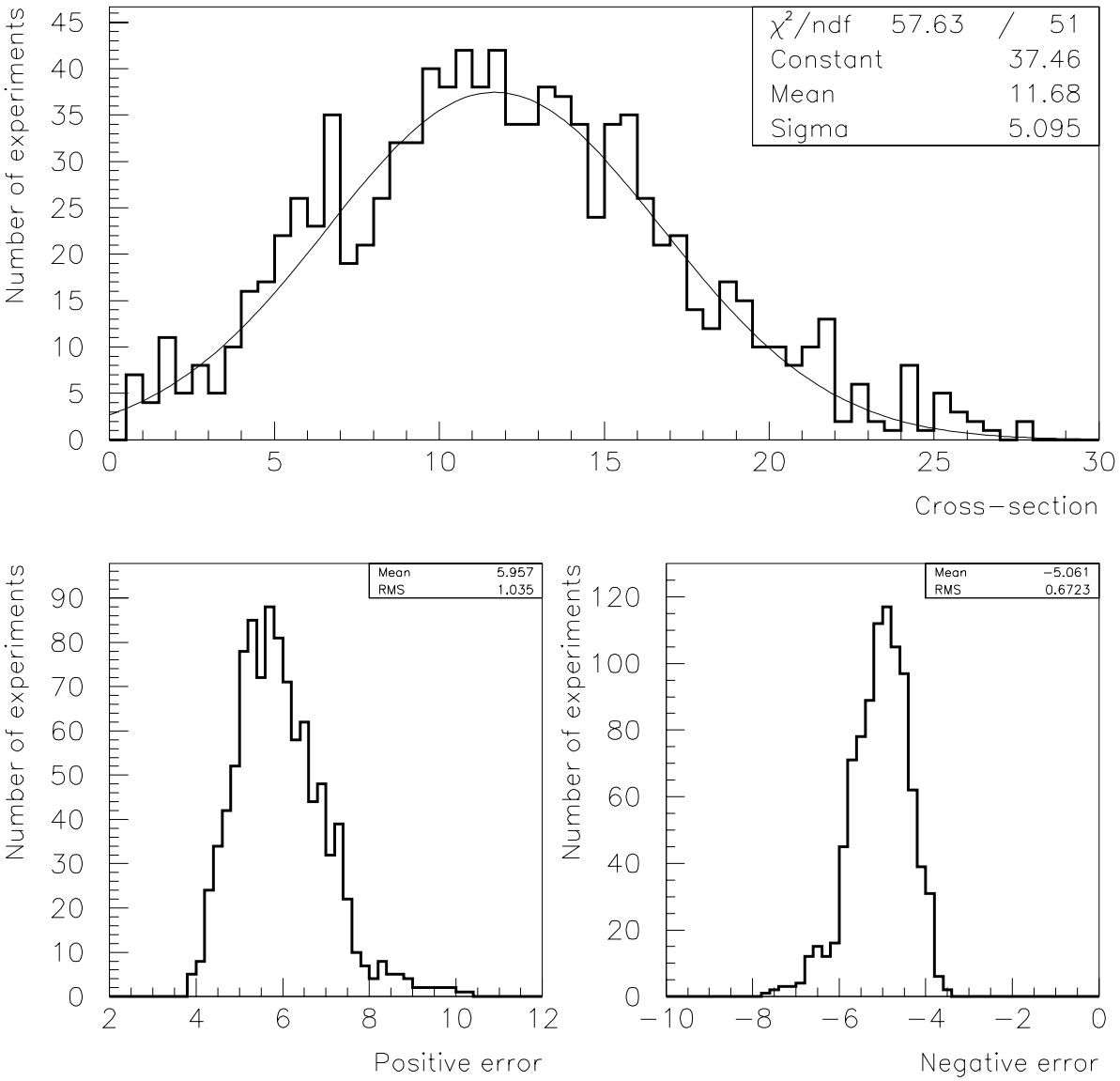

Figure 7-1: Fit results of combined 1A and 1B $t\bar{t}$ production cross-section without the inclusion of the kinematical shape information.

χ^2 comparison of $P^i(\alpha)$ and $P^j(\alpha)$. The χ^2 statistic is given by:

$$\chi^2 = \sum_{k=1}^{N_{bin}} \frac{|P_k^i(\alpha) - P_k^j(\alpha)|^2}{P_k^i(\alpha) + P_k^j(\alpha)}$$

The term $(P_k^i(\alpha) + P_k^j(\alpha))$ in the denominator is the sum of the variances of the two distributions and N_{bin} is the number of non-zero bins in the distribution of each variable. Since distributions with equal normalizations are being compared, there are $(N_{bin} - 1)$ degrees of freedom. Table 7.9 summarizes the χ^2 values per degree of freedom for comparisons between the distributions for QCD and $t\bar{t}$ events for different variables after the $\Sigma E_T \geq 300$ GeV requirement. It can be seen that in ≥ 5 jet events, the most discriminating variables (i.e. ones with the largest χ^2's) are $M_{b\bar{b}}$, $\Delta\phi_{b\bar{b}}$ and $\Delta R_{b\bar{b}}$.

The variables $\Delta\phi_{bb}$, ΔR_{bb} and M_{bb}[1] are correlated. To use these three variables simultaneously to distinguish between QCD, mistags and $t\bar{t}$, discrete probability distribution functions are constructed that take into account their correlations explicitly. These distribution functions, X_i (i =QCD, Mistag or $t\bar{t}$), are parameterized in terms of $\Delta\phi_{bb}$, ΔR_{bb} and M_{bb} and are constructed separately for each jet multiplicity bin. For example, the distribution function for $t\bar{t}$ events with n jets is given by:

$$X_{t\bar{t}}(a,b,c,n) \;\; = \;\; \frac{N_{t\bar{t}}(a,b,c,n)}{\sum_{ijk} N_{t\bar{t}}(a,b,c,n)}$$

Here, $X_{t\bar{t}}(a,b,c,n)$ is the joint probability distribution for a double tagged combination from an n-jet $t\bar{t}$ event to be in the a^{th} $\Delta\phi$, b^{th} ΔR and c^{th} M bin. $N_{t\bar{t}}(a,b,c,n)$ is the number of double tagged combinations from the $t\bar{t}$ Monte Carlo that are in that bin. The probability distributions for QCD $b\bar{b}/c\bar{c}$ and mistags, $X_{QCD}(a,b,c,n)$ and $X_{mistag}(a,b,c,n)$, are constructed similarly.

Due to finite statistics, a coarse binning is chosen so that there are no zero bins. The matrix is constructed with 2 bins in $\Delta\phi$ (0-1.2,>1.2), 2 bins in ΔR (0-1.4,>1.4) and 2 bins in M_{bb} (0-70,>70). These bins are selected to provide the maximum discrimination[2] between $t\bar{t}$ and QCD processes. Figure 7-2 shows the normalized $\Delta\phi$,

[1]Mass of two jets i and j is given by $M_{ij} = \sqrt{2E_{T_i}E_{T_j}\left[cosh(\Delta\eta_{ij}) - cos(\Delta\phi_{ij})\right]}$

[2]For two distributions, $p(x)$ and $q(x)$, over $[x_0, x_n]$ that cross at points $\alpha_1, \cdots, \alpha_{n-1}$, the function $f(x_1, \cdots, x_{n-1}) = \sum_{k=1}^{n} \left(\int_{x_{k-1}}^{x_k} [p(x) - q(x)]\, dx\right)^2$ is maximized when $\{x_i = \alpha_i\}$.

Source	Uncertainty (1A)	Uncertainty (1B)
Energy scale	8%	8%
Radiation modelling	8%	8%
Fragmentation modelling	13%	13%
QCD Normalization	18%	18%
b-tagging	58%	20%

Table 7.8: Summary of individual systematic uncertainties in the cross-section measurement from likelihood method I.

$\Sigma E_T^{corr} \geq 300$ GeV	$N_{jet} = 4$	$N_{jet} = 5$	$N_{jet} = 6$	$N_{jet} = 7$
$\chi^2(\Delta R_{b\bar{b}})$	0.17	0.20	0.27	0.42
$\chi^2(\Delta \phi_{b\bar{b}})$	0.14	0.15	0.25	0.45
$\chi^2(\Delta \eta_{b\bar{b}})$	0.07	0.05	0.04	0.10
$\chi^2(M_{b\bar{b}})$	0.16	0.22	0.36	0.70
$\chi^2(p_{b\bar{b}}^T)$	0.16	0.14	0.11	0.38
$\chi^2(\lvert E_b^T - E_{\bar{b}}^T \rvert)$	0.10	0.05	0.06	0.27
$\chi^2(E_b^T + E_{\bar{b}}^T)$	0.07	0.07	0.16	0.46

Table 7.9: χ^2 comparison of different kinematic variables for QCD and $t\bar{t}$ events. The values of χ^2 per degree of freedom are tabulated for different jet multiplicities.

ΔR and M_{bb} distributions for $t\bar{t}$ (solid) and QCD $b\bar{b}/c\bar{c}$ (hatched) for 5, 6 and $\geq$7 jet events.

7.6 Likelihood Method II

The likelihood function, including the shapes of the kinematical distributions has an additional term, L_k^{shape}, that performs a binned fit of each double tagged combination observed in the data to the distribution shapes for different processes. The likelihood function for each period of data taking is now given by:

$$
\begin{aligned}
L &= \prod_{k=5}^{\geq 7} (L_k^{shape} \cdot L_k^{QCD} \cdot L_k^{mistag} \cdot L_k^{t\bar{t}}) \cdot L_{\int \mathcal{L}dt} \\
L_k^{shape} &= \prod_{i=1}^{N_k^{data}} \left[\alpha_k (X_{QCD})_k^i + (1-\alpha_k)\beta_k (X_{mistag})_k^i + (1-\alpha_k)(1-\beta_k)(X_{t\bar{t}})_k^i \right] \\
L_k^{QCD} &= P(N_k^{QCD}; \alpha_k N_k^{data}) \\
L_k^{mistag} &= P(N_k^{mistag}; (1-\alpha_k)\beta_k N_k^{data}) \\
L_k^{t\bar{t}} &= G(\epsilon_k, \overline{\epsilon_k}, \sigma_{\overline{\epsilon_k}}) P(N_k^{data}; \epsilon_k \sigma_{t\bar{t}} \int \mathcal{L}dt + \alpha_k N_k^{data} + (1-\alpha_k)\beta_k N_k^{data})
\end{aligned}
$$

As before, N_k^{data} is the number of double tagged combinations observed in the data in events with k jets, $\alpha_k N_k^{data}$ is the number of double tagged combinations from QCD, $(1-\alpha_k)\beta_k N_k^{data}$ is the number of mistag combinations and $(1-\alpha_k)(1-\beta_k)N_k^{data}$ is the number of $t\bar{t}$ combinations. For the i^{th} combination observed in the data, the probability of it originating from QCD, $(X_{QCD})_k^i$, is determined using the $\Delta\phi$, ΔR and M_{bb} bins it belongs to. $(X_{mistag})_k^i$ and $(X_{t\bar{t}})_k^i$ are determined similarly.

7.6.1 Additional sources of systematic uncertainty

The inclusion of kinematic shapes introduces two additional sources of systematic uncertainty. First, the finite statistics of the ($\Delta\phi$, ΔR and M_{bb}) distributions of the different processes used in the fits and second, the dependence of the shapes of these distributions on different Monte Carlo generators.

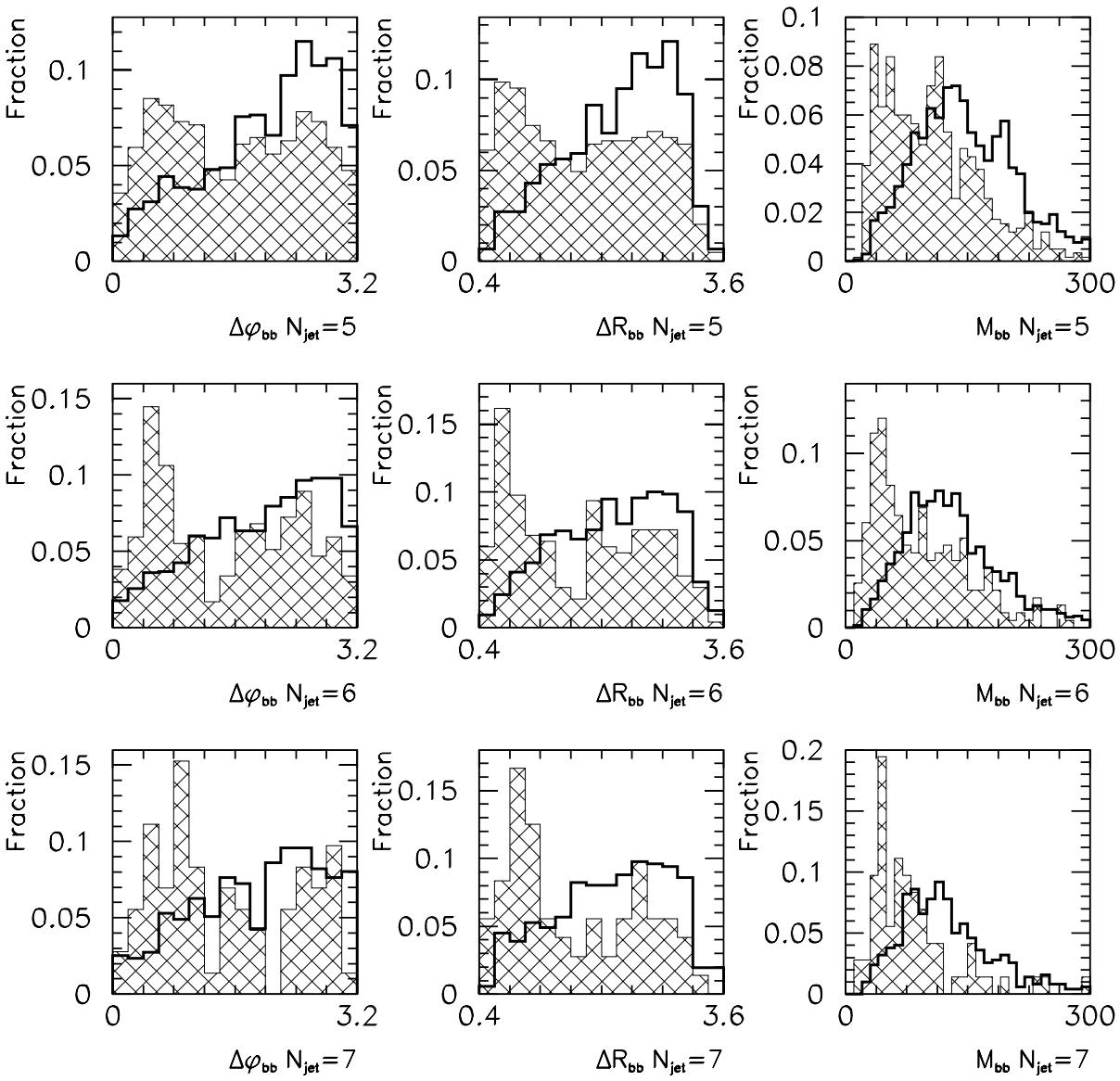

Figure 7-2: A comparison of the shapes of $\Delta\phi_{bb}$, ΔR_{bb} and M_{bb} distributions for $t\bar{t}$ (solid) and QCD $b\bar{b}/c\bar{c}$ (hatched) for 5, 6 and $\geq$7 jet events. All distributions have been normalized to unity.

Finite statistics of the Monte Carlo distributions

The effect of finite statistics of the $\Delta\phi$, ΔR and M_{bb} distributions is determined by allowing all bins of the distributions to vary with Poisson uncertainties every time the likelihood fit is performed. After repeating the likelihood fit multiple times, all the possible effects of the individual statistical fluctuations in the distributions are accounted for.

Shapes of the Monte Carlo distributions

The uncertainty from the shapes of the kinematic distributions arises mainly from the modelling of heavy flavor production in different generators. For $t\bar{t}$, the shapes of ΔR_{bb}, $\Delta\phi_{bb}$ and M_{bb} are compared for HERWIG, ISAJET and PYTHIA and found to be consistent. For QCD, such a comparison between Monte Carlo multijet events is not straightforward as the generation is very CPU intensive. Therefore, instead of generating large Monte Carlo samples, the effect of modelling is estimated using a simulation of QCD generic jet events described in chapter 5. The relative fractions of heavy flavor quark pairs from gluon splitting, flavor excitation and direct production in generic jet events is different from the fractions in multijet events. In order to check the consistency between the three Monte Carlo simulations for different production mechanisms of heavy flavor, the kinematic distributions are compared for two different cases: the two highest E_T jets and the third and fourth highest E_T jets. The two highest E_T heavy flavor jets in the $2 \rightarrow 2$ process come primarily from direct production and flavor excitation. The additional jets come primarily from gluon splitting. Figure 7-3 shows the $\Delta\phi_{bb}$, ΔR_{bb} and M_{bb} distributions for all jets, for heavy flavor jets coming from $b\bar{b}$ and for heavy flavor jets coming from $c\bar{c}$ respectively. The shapes of the distributions are found to be compatible for the different Monte Carlo generators. Figure 7-4 shows the same distributions for the third and fourth highest E_T jets. Again, the predictions of the Monte Carlo generators are seen to be consistent. Therefore, no uncertainty is assigned to this effect.

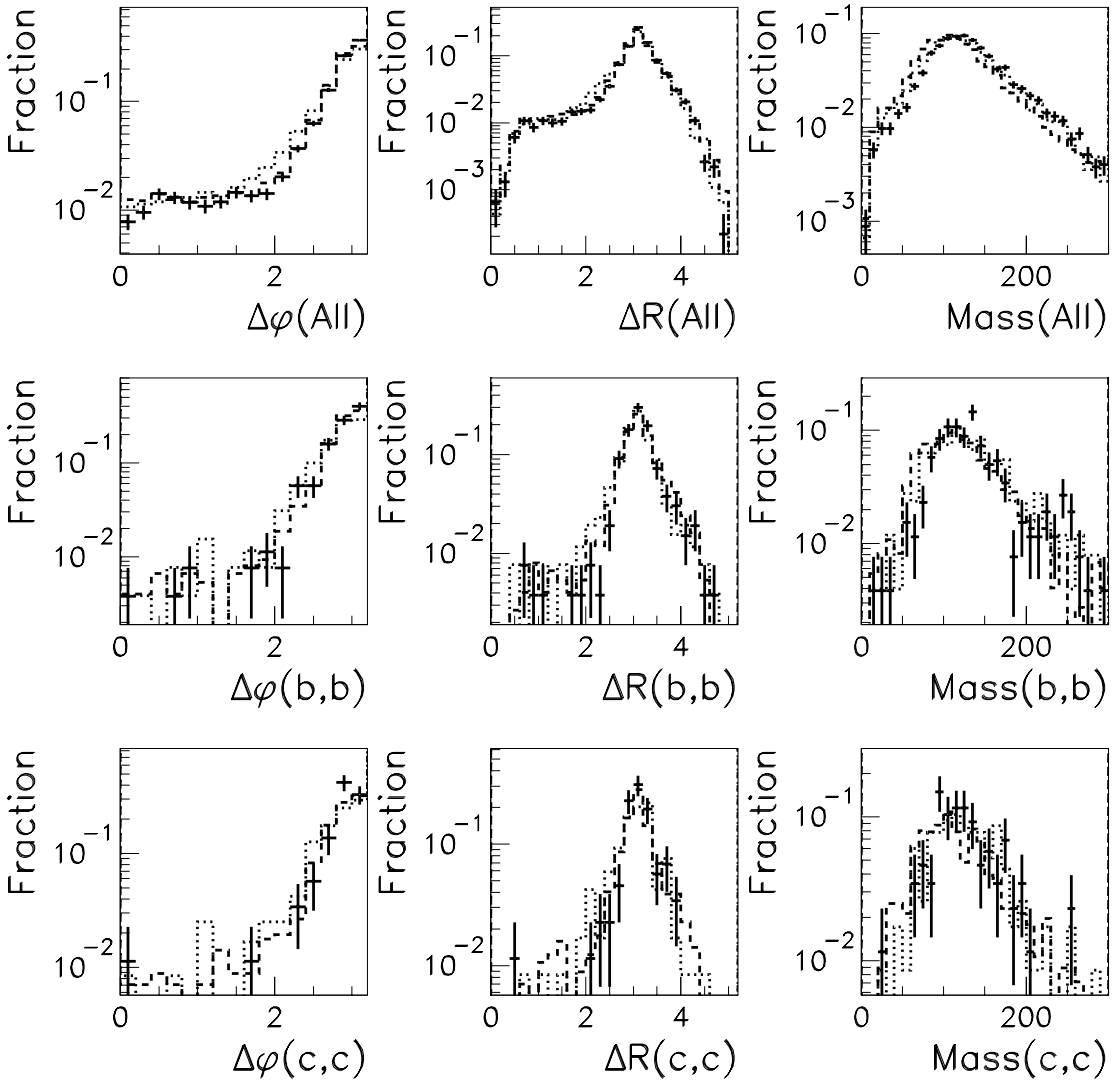

Figure 7-3: A comparison of the shapes of $\Delta\phi_{b\bar{b}}$, $\Delta R_{b\bar{b}}$ and $M_{b\bar{b}}$ distributions for the two highest E_T jets in QCD $2 \rightarrow 2$ process for HERWIG (data points), ISAJET (dashed histogram) and PYTHIA (dotted histogram). Distributions are shown for all jets, for jets from $b\bar{b}$ pair and for jets from $c\bar{c}$ pair.

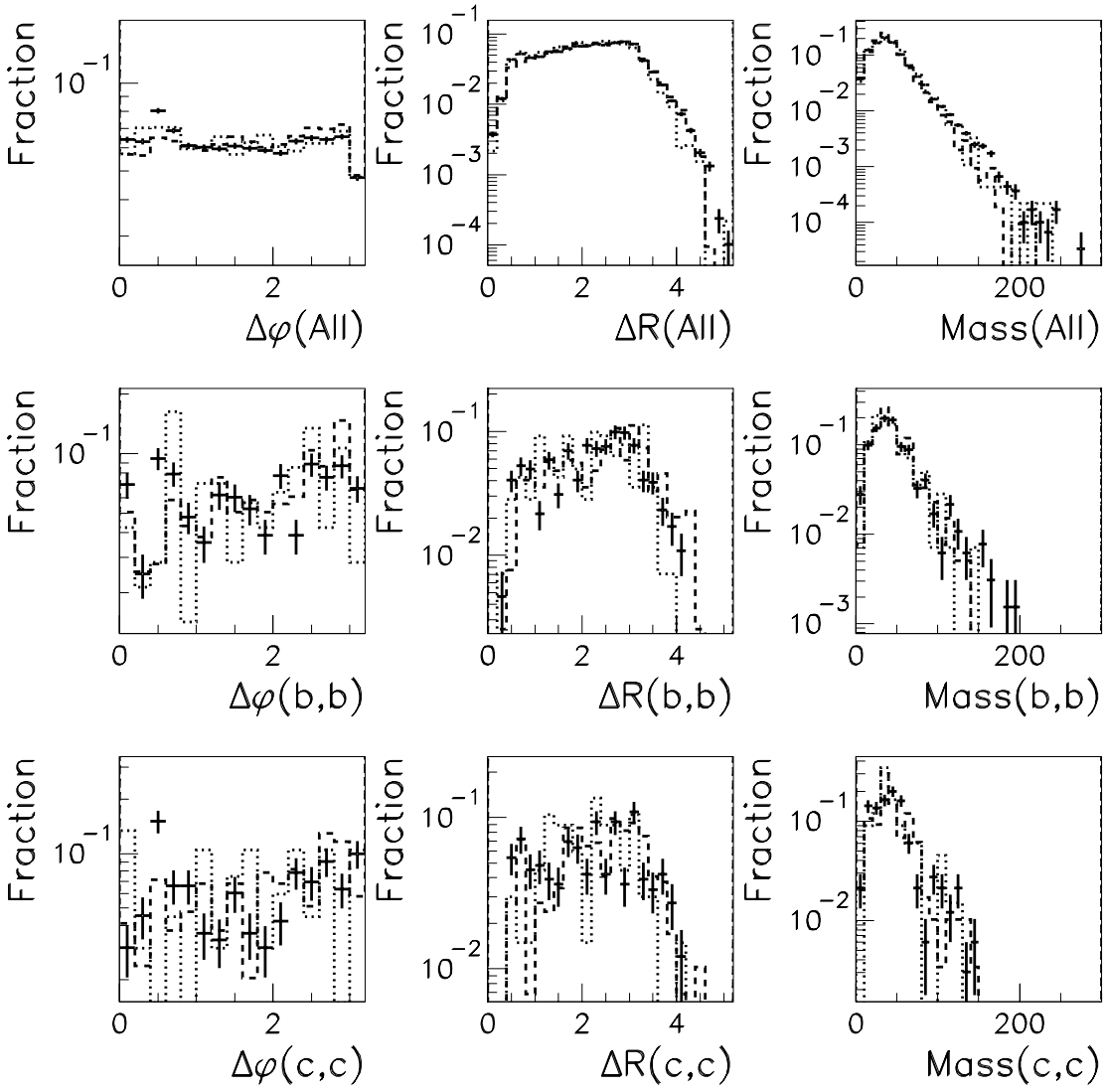

Figure 7-4: A comparison of the shapes of $\Delta\phi_{b\bar{b}}$, $\Delta R_{b\bar{b}}$ and $M_{b\bar{b}}$ distributions for the third and fourth highest E_T jets in QCD $2 \rightarrow 2$ process for HERWIG (data points), ISAJET (dashed histogram) and PYTHIA (dotted histogram.) Distributions are shown for all jets, for jets from $b\bar{b}$ pair and for jets from $c\bar{c}$ pair.

7.6.2 The $t\bar{t}$ signal

We perform the likelihood fit again using the additional information from the shapes of kinematic variables. In Run 1A and 1B data combined, we observe a signal of 42.1 ± 16.2 combinations over a background of 129.9 ± 16.6. Separately we observe 6.1 ± 3.0 (20.9 ± 3.8) and 36.1 ± 15.2 (108.9 ± 15.5) signal (background) combinations in Run 1A and 1B respectively. Again, the number of combinations is used to determine the number of ≥ 2 b-tagged events. In Run 1A and 1B data combined, we observe a signal of 37.2 ± 13.5 events over a background of 119.8 ± 14.6. Individually, we observe 6.0 ± 3.0 (21.0 ± 3.8) and 31.2 ± 13.2 (98.8 ± 14.1) signal (background) events in Run 1A and 1B respectively. The number of double tagged combinations and events from each process is summarized in tables 7.10 and 7.11 respectively. Figure 7-5 shows the observed number of double tagged combinations and the total fit background for different jet multiplicities.

7.6.3 The $t\bar{t}$ production cross-section

With the inclusion of the kinematical shapes, the fit cross-section is $12.0^{+6.7}_{-6.0}$ pb. Repetition of the same fit after turning off all systematic effects results in a cross-section of $10.6^{+4.5}_{-4.2}$ pb, or a relative average statistical uncertainty of 41%. Therefore, the combined cross-section with the inclusion of the kinematical shapes is measured to be $12.0 \pm 4.9(stat)^{+4.6}_{-3.5}(syst)$ pb. The result of 1000 fits is shown in figure 7-6. Also shown are the asymmetric uncertainties returned by the fit. Table 7.12 summarizes the relative contribution of individual systematic effects to the total uncertainty in the cross-section separately for Run 1A and 1B. The individual contributions of the different sources of systematic uncertainty are summarized in table 7.12.

7.6.4 Consistency of the data with QCD, Mistags and $t\bar{t}$

In order to check the consistency of the data with a sum of QCD, Mistags and $t\bar{t}$, the kinematical distributions of the observed double tagged combinations can be used. Figures 7-7 and 7-8 show the invariant mass (M_{bb}) of the two tagged jets for ≥ 5

Run I	$N_{jet} = 5$	$N_{jet} = 6$	$N_{jet} \geq 7$	Total ($N_{jet} \geq 5$)
N_{2c}^{data}	109	50	13	172
N_{2c}^{QCD}	63.3±10.7	23.0±6.2	5.8±2.9	92.1±16.1
N_{2c}^{mistag}	25.7±5.0	11.2±3.7	0.9±1.5	37.8±6.1
N_{2c}^{bkgd}	89.0±10.9	34.2±7.0	6.6±3.1	129.9±16.6
$N_{2c}^{t\bar{t}}$	20.0±10.5	15.8±6.8	6.4±3.0	42.1±16.2

Table 7.10: Likelihood fit results for Run 1A and 1B using the kinematical shapes. The table shows the total number of double tagged combinations observed in data, and the number of double tagged combinations from QCD, Mistag and $t\bar{t}$ returned by the fit.

Run I	$N_{jet} = 5$	$N_{jet} = 6$	$N_{jet} \geq 7$	Total ($N_{jet} \geq 5$)
N_{2b}^{data}	102	42	13	157
N_{2b}^{QCD}	60.1±10.4	21.2±5.4	4.6±2.3	85.9±14.6
N_{2b}^{mistag}	24.8±5.2	7.0±2.5	2.1±1.4	33.9±5.5
N_{2b}^{bkgd}	84.9±10.6	28.1±5.4	6.7±3.0	119.8±14.6
$N_{2b}^{t\bar{t}}$	17.1±9.2	13.9±5.4	6.3±3.0	37.2±13.5

Table 7.11: Likelihood fit results for Run 1A and 1B using the kinematical shapes. The table shows the total number of ≥ 2 b-tagged events observed in data, and the number of ≥ 2 b-tagged events from QCD, Mistag and $t\bar{t}$ returned by the fit.

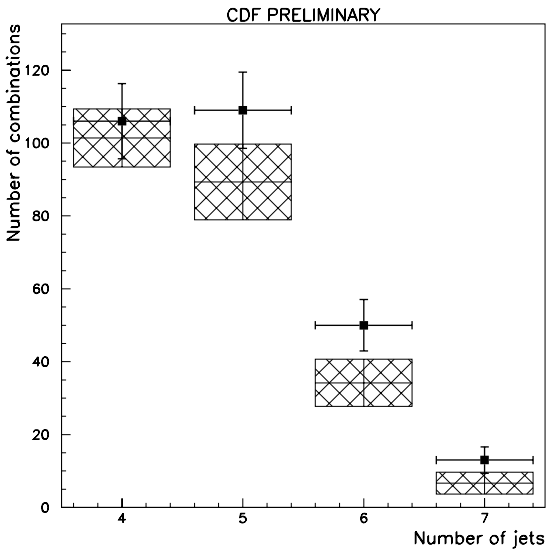

Figure 7-5: Observed number of double tagged combinations (squares) and the expected background (hatched) for different jet multiplicities.

Source	Uncertainty (1A)	Uncertainty (1B)
Template statistics	4%	4%
Energy scale	8%	8%
Radiation modelling	8%	8%
Fragmentation modelling	13%	13%
QCD Normalization	18%	18%
b-tagging	58%	20%

Table 7.12: Summary of individual systematic uncertainties in the cross-section measurement from likelihood method II.

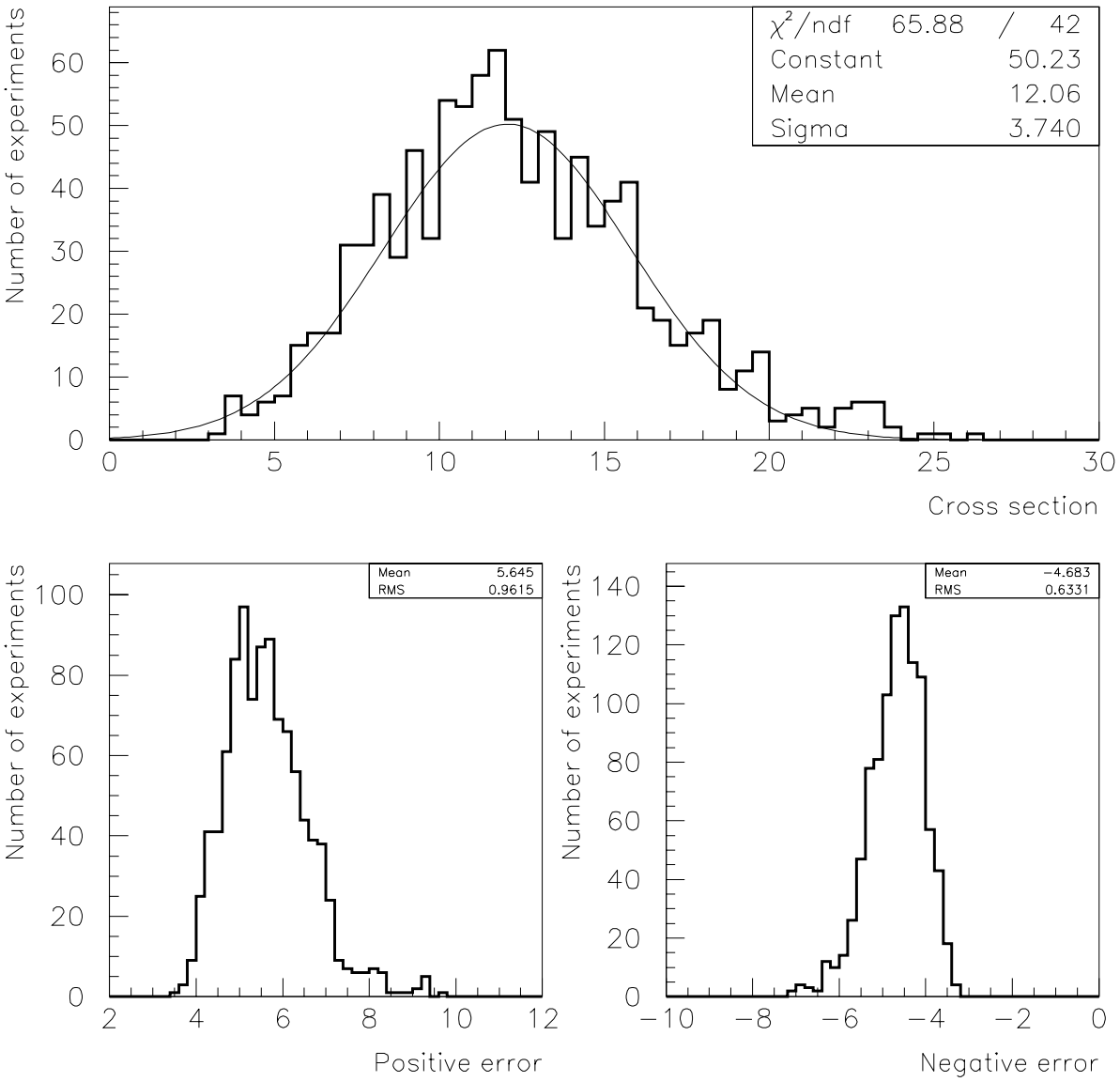

Figure 7-6: Fit results of combined 1A and 1B top production cross-section with the inclusion of the kinematical shape information.

and $\geq$ 6 jet events where the $t\bar{t}$ expectation is not negligible. The contributions from QCD, Mistags and $t\bar{t}$ have been overlayed on the data M_{bb} distribution. The M_{bb} shape of each process is determined from Monte Carlo (QCD and $t\bar{t}$) or data (Mistags) and the normalization is fixed to the value returned by the likelihood fit.

7.6.5 The significance of the measurement

To calculate the significance of the measurement, a Poisson probability, p, is calculated for the number of double tagged combinations from background (N_{bkg}) to fluctuate to the total number observed (N_{obs}) or greater.

$$p = \sum_{k=N_{obs}}^{\infty} P(k; N_{bkg})$$

A Monte Carlo method is used with the following steps. The number of background combinations is first smeared using a Gaussian distribution of mean N_{bkg} and standard deviation δN_{bkg} to yield $N_{bkg'}$. Then $N_{bkg'}$ is fluctuated using a Poisson distribution (with an expectation $N_{bkg'}$). The resulting number, N, is then compared to N_{obs}. The total Poisson probability p is given by the fraction of the total number of trials where N is greater than or equal to N_{obs}.

In the signal region, 172 double tagged combinations are observed in the data over a background of 129.8$\pm$16.0. The probability that the background fluctuates to 172 or greater is 1.9%. This is a 2.1σ effect assuming one-sided Gaussian statistics. A one-sided Gaussian distribution is used since the background can only fluctuate high to account for the observed excess.

7.6.6 A cross-check of the likelihood fit

Including the information from shapes, the fit cross-section is $12.0^{+6.7}_{-6.0}$ pb. To estimate the expected reduction in fractional uncertainty with the inclusion of the shape information, the following procedure is used.

Pseudo-data sets are generated using just the Monte Carlo samples and the mistag matrix, corresponding to $\sigma_{t\bar{t}} = 12$ pb. The total number of double tagged combinations in each set is fixed to the number observed in the data (N_{obs}) for each jet

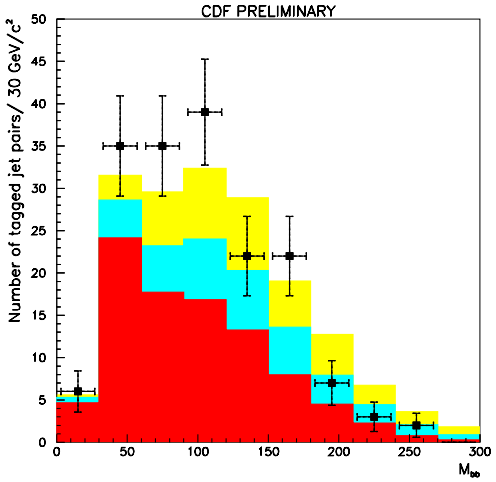

Figure 7-7: M_{bb} distribution of ≥ 5 jet data combinations with result of fit superimposed (data: squares, top: light gray, mistag: dark gray, QCD: black).

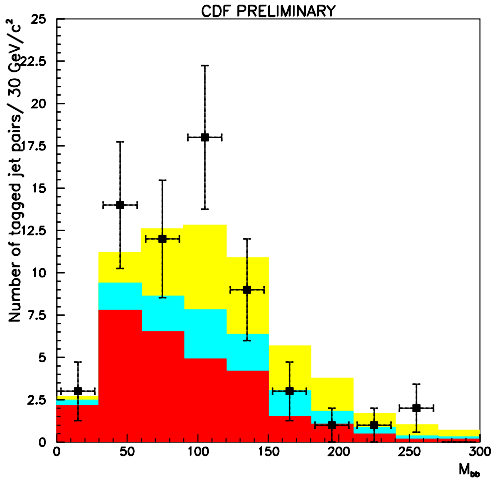

Figure 7-8: M_{bb} distribution of ≥ 6 jet data combinations with result of fit superimposed (data: squares, top: light gray, mistag: dark gray, QCD: black).

multiplicity. The expected number of $t\bar{t}$ signal (N_{top}) is determined for each jet multiplicity bin, for Run 1A and 1B, using the total acceptance, and then rounded to the nearest integer. The expectation from mistags (N_{mistag}) is normalized to the number observed. The normalization of QCD is set to ($N_{obs} - N_{top} - N_{mistag}$).

The kinematic distributions of the pseudo-data sets are generated by selecting Monte Carlo events of the correct jet multiplicity randomly from the large Monte Carlo data sets. The distributions of the mistags are generated in a similar fashion using the negative tagging rate matrix described in chapter 5. We use 100 pseudo-data sets and fit each of them 100 times to determine their total statistical and systematic uncertainties. Table 7.13 summarizes the resulting cross-sections, without and with using the additional information from the shapes of kinematical distributions.

Category	Cross-section (pb)
No Shapes	$11.8^{+7.2}_{-6.6}$
Shapes	$12.1^{+6.2}_{-5.6}$

Table 7.13: Results of the fit for 100 pseudo-data sets for $\sigma_{t\bar{t}} = 12$ pb.

In the data, the inclusion of the shapes of kinematical distributions changes the cross-section from 11.7 ± 7.6 (65% uncertainty) to 12.0 ± 6.4 (53% uncertainty). This is an improvement of 12% in the relative uncertainty in the cross-section. From our pseudo-data sets, we expect a 10% reduction in the fractional uncertainty from 59% to 49% which is consistent with the reduction observed in the data.

Chapter 8

Conclusions

We have searched for the production and fully hadronic decay of $t\bar{t}$ pairs. In Run 1A and 1B data we observe 157 events with ≥ 5 jets including ≥ 2 b-tagged jets and a total transverse energy greater than 300 GeV. Using these events we isolate a $t\bar{t}$ signal and measure the $t\bar{t}$ production cross-section. The analysis uses a likelihood fit technique in two different ways. In the first method, a likelihood fit is used to combine the cross-section measurements in individual jet multiplicity bins (Method A) and in the second, additional kinematical variables are used to distinguish between QCD and $t\bar{t}$ (Method B). The final results of this analysis are summarized in table 8.1 which shows the number of events with ≥ 2 b-tagged jets from background and $t\bar{t}$ in Run 1 data for the two likelihood fit methods. The measured $t\bar{t}$ production cross sections are also shown.

$\int \mathcal{L}dt = 109.4 \pm 7.2$ pb^{-1}	N_{bkg}	$N_{t\bar{t}}$	$\sigma_{t\bar{t}}$ (pb)
Method A	119.5 ± 17.9	37.5 ± 16.9	$11.7 \pm 5.1(stat)^{+6.0}_{-5.1}(syst)$
Method B	119.8 ± 14.6	37.2 ± 13.5	$12.0 \pm 4.9(stat)^{+4.6}_{-3.5}(syst)$

Table 8.1: A summary of the final results of the analysis. The number of ≥ 2 b-tagged events from background and $t\bar{t}$ in Run 1 data are shown. The measured $t\bar{t}$ production cross-section is also shown.

8.1 CDF's $t\bar{t}$ production cross-section measurement in the fully hadronic decay mode

As mentioned in chapter 2, two parallel but complementary analyses were followed at CDF to search for the fully hadronic decay of $t\bar{t}$ pairs. Both analyses start from the selection sample defined in chapter 4 and require that the events have a total transverse energy greater than 300 GeV and at least one b-tagged jet. From this point the two analyses diverge. The analysis described in this thesis (Analysis I) requires the presence of additional b-tagged jets in events while the other (Analysis II) imposes additional kinematical requirements on the events to reduce the QCD background. The details of Analysis II have been described in chapter 2. The two analyses may be combined to obtain an improved measurement.

In order to combine the results of the two analyses, the correlations between them have to be taken into account. These correlations arise because of an overlap in both the total acceptance and the sample selection of the two analyses. Therefore, in the combination of the two analyses, an appropriate likelihood function is used to take these correlations into account.

The overlap in the total acceptance is treated by factorizing the total acceptance for the two analyses into four uncorrelated terms. The value of each term is determined for a top quark mass of 175 GeV/c^2. The statistical and systematic uncertainties in these terms are taken to be Gaussian distributed in the likelihood function. These terms are:

- The efficiency for passing the common selection requirements for the two analyses, ϵ_C. These requirements are $N_{jet} \geq 5$ and $\Sigma E_T \geq 300$ GeV. ϵ_C is determined to be $26.3 \pm 4.5\%$.

- The efficiency for observing at least one b-tag in a $t\bar{t}$ event, ϵ_b. The tagging efficiencies for Runs 1A and 1B and are $36.0 \pm 10.4\%$ and $43.5 \pm 4.4\%$ respectively.

- The efficiency for observing additional b tags in a $t\bar{t}$ event, ϵ_1 (The requirements of Analysis I). The value of ϵ_1 for Run 1A and 1B is $19.3 \pm 11.2\%$ and $28.1 \pm 5.6\%$

respectively.

- The efficiency for passing the additional kinematical requirements of Analysis II, ϵ_2, is determined to be $40.5 \pm 3.6\%$.

The total acceptances for Analyses I and II, $\epsilon_{\rm I}^{tot}$ and $\epsilon_{\rm II}^{tot}$ can be written in terms of these uncorrelated terms. Note that $\epsilon_{\rm I}^{tot}$ and $\epsilon_{\rm II}^{tot}$ are for *events* that pass the selection criteria of each individual analysis.

$$\begin{aligned} \epsilon_{\rm I}^{tot} &= \epsilon_C \cdot \epsilon_b \cdot \epsilon_1 \\ \epsilon_{\rm II}^{tot} &= \epsilon_C \cdot \epsilon_b \cdot \epsilon_2 \end{aligned}$$

The overlap in the sample selection between the two analyses is taken into account by using a bi-variate Gaussian term in the likelihood function that includes the correlation in the selection of the two data samples. If x_i (i =I,II) is the number of signal events in each sample (i.e. selected by each analysis), μ_i is the average of the number of signal events over all samples and σ_i is its uncertainty, then the bi-variate Gaussian $\mathcal{G}(x_1, x_2, \mu_1, \mu_2, \sigma_1, \sigma_2, \rho)$ is given by:

$$\mathcal{G} = \frac{1}{2\pi\sigma_1\sigma_2\sqrt{1-\rho^2}} \cdot \exp\left\{\frac{-1}{2(1-\rho^2)}\left[\frac{(x_1-\mu_1)^2}{\sigma_1^2} - \frac{2\rho(x_1-\mu_1)(x_2-\mu_2)}{\sigma_1\sigma_2} + \frac{(x_2-\mu_2)^2}{\sigma_2^2}\right]\right\}$$

The correlation coefficient $\rho \equiv \frac{\overline{(x_1-\mu_1)(x_2-\mu_2)}}{\sigma_1\sigma_2}$ is calculated using a sample of 10000 $t\bar{t}$ Monte Carlo events passing the common requirements of the two analyses. The sample is divided into 100 sub-samples of 100 events each and the number of events in each sub-sample is allowed to fluctuate with its Poisson uncertainties. By explicitly determining x_i, μ_i and σ_i, the correlation coefficient is calculated to be $\rho = 0.34 \pm 0.13$.

In order to determine the combined value of the $t\bar{t}$ production cross-section in the fully hadronic mode, separate likelihood terms are used for Run 1A and Run 1B data since their b-tagging efficiencies are different. Using a Gaussian distribution $G(x; \bar{x}, \sigma_x)$ with a mean $\bar{x}$ and uncertainty σ_x, the likelihood term for each period of data taking, L_α (α =1A or 1B), is given by:

$$\begin{aligned} L_\alpha = {} & G(\int \mathcal{L}dt; \overline{\int \mathcal{L}dt}, \sigma_{\int \mathcal{L}dt}) \cdot G(\epsilon_C; \overline{\epsilon_C}, \sigma_{\epsilon_C}) \cdot G(\epsilon_b; \overline{\epsilon_b}, \sigma_{\epsilon_b}) \cdot G(\epsilon_1; \overline{\epsilon_1}, \sigma_{\epsilon_1}) \cdot G(\epsilon_2; \overline{\epsilon_2}, \sigma_{\epsilon_2}) \cdot \\ & \mathcal{G}(\epsilon_b \cdot \epsilon_C \cdot \epsilon_1 \cdot \sigma_{t\bar{t}} \cdot \int \mathcal{L}dt, n_1, \sigma_1, \epsilon_b \cdot \epsilon_C \cdot \epsilon_2 \cdot \sigma_{t\bar{t}} \cdot \int \mathcal{L}dt, n_2, \sigma_1, \rho) \end{aligned}$$

The combined likelihood function L is given by:

$$L = L_{1A} \cdot L_{1B}$$

Here n_1 and n_2 are the number of $t\bar{t}$ events identified by Analysis I and II respectively. For Analysis I, the number of $t\bar{t}$ events from the likelihood fit without using the ΔR, $\Delta\phi$ and M distributions of the tagged jets (Method A) are used. This is a conservative approach in order to avoid any Monte Carlo dependent systematic effects, since the Monte Carlo dependency of the shapes of the distributions has not been checked directly for QCD multijet events. The number of signal events in Analysis I, n_1, is 5.9 ± 3.9 and 31.6 ± 16.4 for Run 1A and 1B respectively. Similarly, the number of signal events in Analysis II, n_2, is 10.4 ± 6.0 and 34.7 ± 16.1 for Run 1A and 1B respectively.

By maximizing the likelihood function, the combined $t\bar{t}$ production cross-section in the fully hadronic mode is determined to be $10.1 \pm 1.9(stat)^{+4.1}_{-3.1}(syst)$ pb. Varying ρ within its uncertainty changes the cross-section and its uncertainty by 0.1 pb. The $t\bar{t}$ cross-sections measured in different decay channels are shown in figure 8-1. The vertical band indicates the theoretical $O(\alpha^3)$ calculation of 5.3 ± 0.3 pb [22, 23, 24]. The combined $t\bar{t}$ production cross-section at CDF using all the decay modes is also shown [28]. The cross-section in the fully hadronic mode is consistent with the cross-sections measured in the other channels.

8.2 Future improvements

CDF is looking forward to Run II, with an upgraded detector and higher instantaneous luminosities. An expected integrated luminosity of 2 fb^{-1}, and the enhanced acceptance and capabilities of the new Silicon Vertex Detector will further the study of $t\bar{t}$ decays, including the fully hadronic mode. The planned upgrades in the CDF detector, and the new possibilities for doing top quark physics have been detailed elsewhere [61]. Some of the future improvements to the cross-section measurement of this thesis are detailed below.

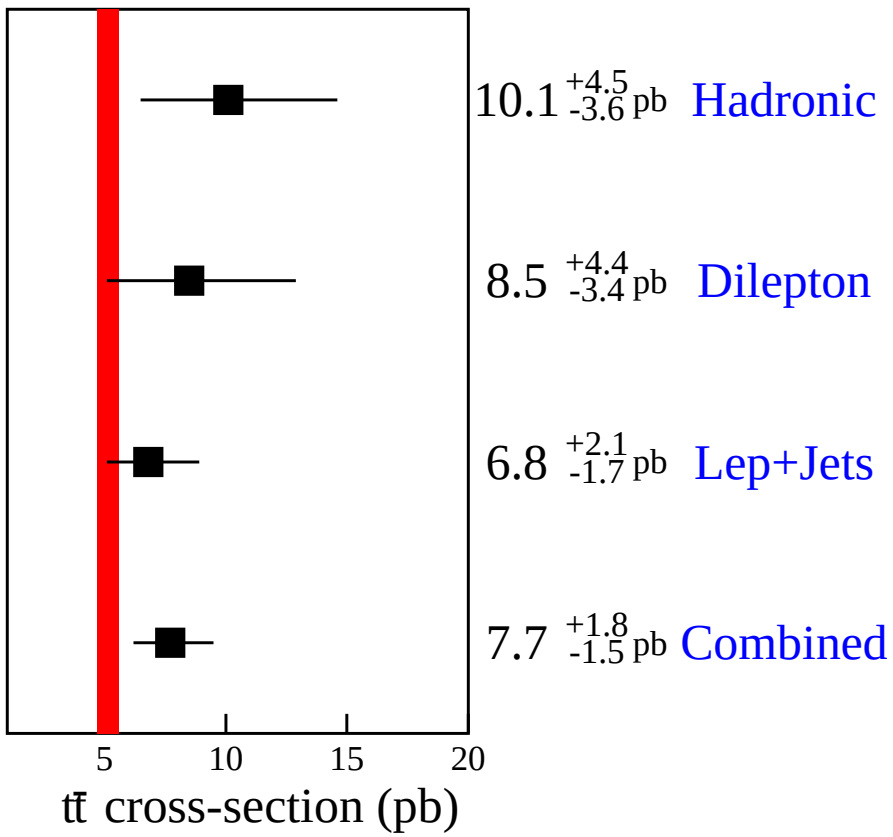

Figure 8-1: A summary of the $t\bar{t}$ production cross-sections measured at CDF from different decay modes. The combined cross-section using all the decay modes is also shown.

Systematic uncertainties

A study of the different systematic effects will reduce the total systematic uncertainty in the cross-section measurement. Currently, the dominant source of systematic uncertainty is from the requirement of ≥ 2 b-tags in an event. A study of the Monte Carlo to data scale factors can enable us to reduce the uncertainty from this source. Other sources of systematic uncertainty include the effect of radiation and fragmentation modelling. These uncertainties can be reduced by a detailed study of different Monte Carlos, and by a comparison of the Monte Carlo predictions with the data. With about 2 fb^{-1} of data anticipated in Run II, it would be possible to do a meaningful comparison of the amount of gluon radiation in the data, and that present in different Monte Carlo programs. Another large source of systematic uncertainty comes from the determination of the normalization of QCD. It is discussed in a separate section below.

QCD $b\bar{b}/c\bar{c}$ background

A complete understanding of the QCD heavy flavor background is essential for reducing the uncertainty in its normalization. There are two main issues here that would benefit from further studies with larger data sets. First, it should be possible to determine the QCD normalization directly using the data, without any reliance on a Monte Carlo. As suggested in chapter 5, a tagging rate method that takes into account the kinematics of correlated heavy flavor production can probably be used. Second, the systematic uncertainties from the theoretical modelling of QCD multijet production can be investigated further using a dedicated generation of Monte Carlo QCD multijet samples using different generators. It would then be possible to estimate the systematic uncertainty in the shapes of different kinematical variables for QCD multijets directly.

Combination of the two analyses

It will be instructive to integrate the two analyses (Analysis I and II) into one, possibly imposing stringent kinematical requirements in addition to demanding ≥ 2 b-tags in an event. Given the higher b-tagging efficiencies and statistics expected in Run II, an optimized analysis can provide a relatively clean sample of $t\bar{t}$ pairs. Though it is unlikely that a top quark mass measurement in the fully hadronic decay mode will be competitive with the one in $\ell + jets$ decay mode, the relative uncertainty can be reduced by using a cleaner sample.

A new multijet trigger

A new multijet trigger can be designed based upon the planned capability of identifying b jet candidates at the trigger level [61]. A possible trigger could require ≥ 4 clusters passing a minimum transverse energy requirement, and the presence of at least one candidate b quark jet. Such a multijet trigger could also be useful to study $W/Z + jets$ and WH/ZH production with all the bosons decaying into fully hadronic final states. It may be possible to study the decays $Z \rightarrow b\bar{b}$ and $H \rightarrow b\bar{b}$ with the application of suitable kinematical requirements.

Effect of multiple interactions

As mentioned earlier, a detailed study of the effect of multiple interactions in the multijet data sample has not been performed, though the studies performed for this thesis show that the effect is small both for the kinematical and b-tagging requirements. Multiple interactions would have a much bigger effect in this channel during Run II, due to higher luminosities. The proposed upgrade for the Silicon Vertex Detector will also provide z information, allowing a precise determination, and hence the separation of the position of different primary vertices in an event.

Appendix A

The b-tagging algorithm

The b-tagging algorithm consists of the following steps:

- Tracks are associated to a jet if they are within a cone of $\Delta R = 0.4$ of a jet with $E_T \geq 15$ GeV, and selected on the basis of certain loose track quality requirements.
- An attempt is made to fit ≥ 3 tracks into a secondary vertex (Pass 1).
- If no secondary vertex is found then track quality requirements are tightened and ≥ 2 tracks are used to find a secondary vertex (Pass 2).
- If a secondary vertex is found in Pass 1 or 2, the jet is flagged as *tagged*.

Figure A-1 shows the flow chart detailing the secondary vertex finding algorithm. The development and optimization of the algorithm is described elsewhere [32].

A.1 Track quality requirements for b-tagging

For all tracks within $\Delta R = 0.4$ of a jet with $E_T \geq 15$ GeV, the track quality requirements imposed for Pass 1 and 2 are detailed below:

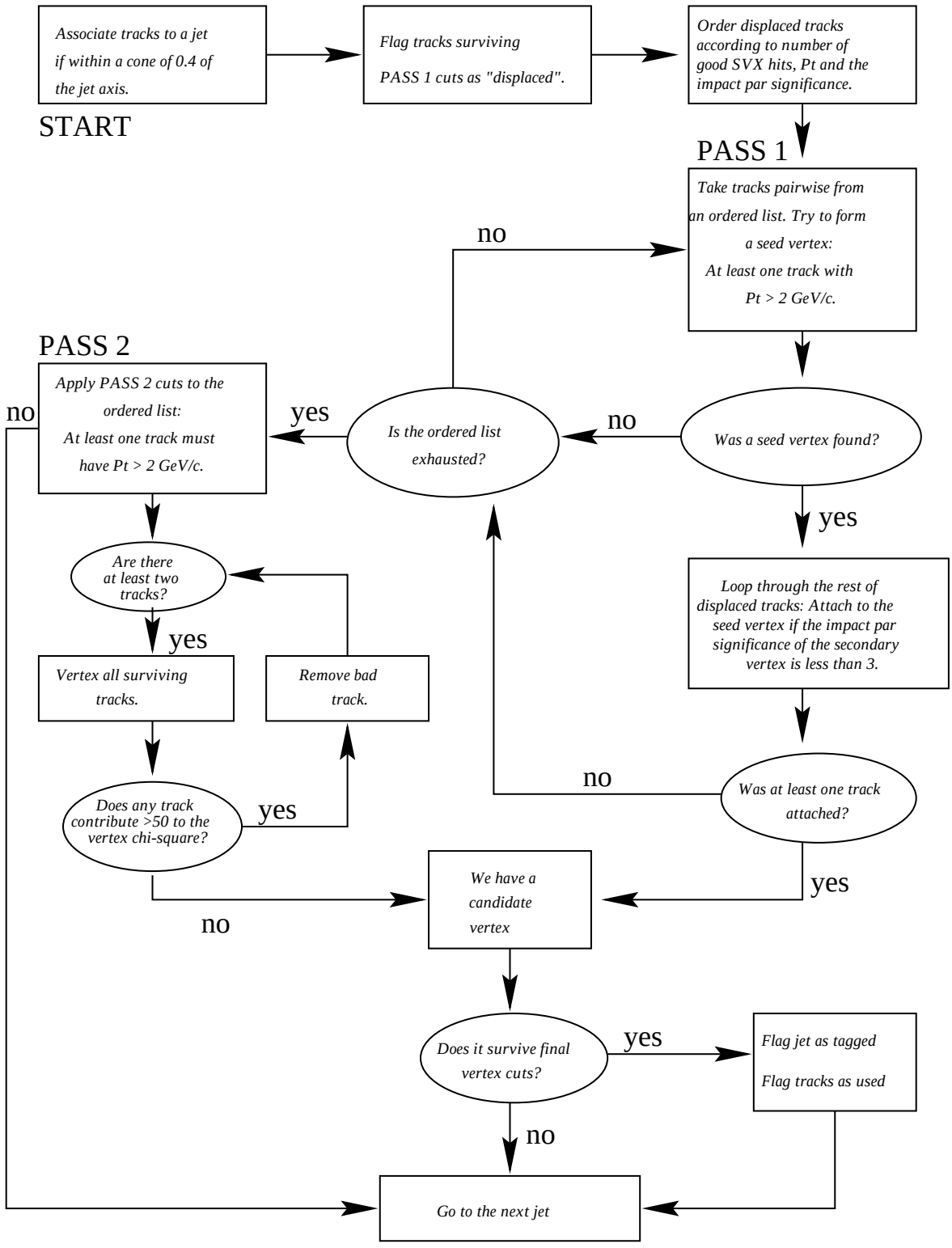

Figure A-1: *Flow chart of the b-tagging algorithm.*

A.1.1 Pass 1 requirements

- Track impact parameter $|d_0| < 0.15$ cm to remove tracks consistent with photon conversions ($\gamma \rightarrow e^+e^-$) and decays of K_s mesons or Λ baryons originating from the primary vertex. This requirement removes 3.1% of tracks prior to tagging and is approximately 99% efficient for tracks from b decay [51].
- Track impact parameter significance $\frac{d_0}{\sigma_{d_0}} > 2.5$
- Chi-square per degree of freedom of the secondary vertex fit, $\chi^2_r < 6$.
- Pass CTC requirements, as detailed below in a separate section.
- To ensure that all the tracks come from the same primary vertex: $|z_{track} - z_{primary\ vertex}| < 5$ cm.

For tracks with hits in 3 or more layers of the SVX detector, the minimum transverse momentum required is 0.5 GeV/c. In addition, at least one hit in the SVX is required to be *good*. A good hit in the SVX contains no noisy or dead strips in the detector, is ≤ 3 strips long and has no contribution from any neighboring hits. Requiring a good hit reduces ambiguities in track reconstruction that arise from having different possible tracks that can pass through overlapping hits. It also reduces the possibility of reconstructing tracks with one hit coming from the noise in a faulty strip. For tracks with hits in two layers of the SVX detector the requirements are more stringent. The minimum transverse momentum required is 1.5 GeV/c. Moreover, both hits are required to be good, and either in the inner-most two layers of the SVX or in the outer-most two layers. Having hits in two consecutive layers reduces the possibility of assiging a wrong hit to a track. Tracks with hits in layers 2 and 3 of the SVX are not considered to minimize the effects of multiple scattering.

In addition, all tracks that are part of a K_s, Λ (as described in a separate section below) or another candidate secondary vertex are rejected.

A.1.2 Pass 2 requirements

If no secondary vertex is found during Pass 1, then stricter track requirements are imposed and a secondary vertex is searched for using 2 or more tracks. For all tracks that survive the Pass 1 requirements, the following requirements are required in addition for Pass 2:

- Impact parameter significance of the track $\frac{d_0}{\sigma_{d_0}} > 3.0$
- Track transverse momentum $P_t > 1.0$ GeV/c

Only tracks with 3 or more hits in the SVX are allowed. For tracks with 4 hits, at least one hit is required to be good. For tracks with 3 hits, at least two hits are required to be good.

A.1.3 CTC requirements

All tracks are required to be 3D. As explained in chapter 3, these are tracks with hits in the axial and stereo superlayers of the CTC. They must have hits in ≥ 2 axial layers, with ≥ 4 hits in each layer. They must also have hits in ≥ 2 stereo layers with ≥ 2 hits in each layer. Requiring 3D tracks ensures that their track parameters are well measured, and therefore the uncertainties in the reconstructed secondary vertex are small.

A.1.4 K_s and Λ removal

A track is considered to be a part of a K_s or a Λ vertex if it forms a vertex with an oppositely charged track[1] that passes the CTC requirements. Both tracks are required to have $\frac{d_0}{\sigma_{d_0}} > 2.5$. In addition, the vertex is required to satisfy the following requirements:

- Using vertex-constrained momenta, the vertex mass must be within 10 MeV/c^2 of the K_s and 6 MeV/c^2 of the Λ mass. Track momentum resolution determines the mass requirement.

[1] $K_s \rightarrow \pi^+\pi^-$, $\Lambda \rightarrow p\pi^-$

- The displacement of the vertex projected along its axis must be greater than 10σ where σ is the uncertainty in the displacement of the vertex.
- The displacement of the vertex projected perpendicular to its axis must be less than 3σ where σ is defined identically as above.

A.2 Final secondary vertex requirements

Once a candidate secondary vertex is found with ≥ 2 tracks, it is required to have:

- Secondary vertex fit $\chi^2 \leq 50$
- Two dimensional decay distance $|L_{xy}| \leq 2.5$ cm. This restricts the secondary vertices to a region inside the radius of the inner layer of the SVX.
- The significance of the decay distance $\frac{|L_{xy}|}{\sigma_{L_{xy}}} \geq 3$
- $|c\tau| \leq 1.0$ cm.
- $|M_{vertex} - M_{K_s}| \geq 20$ MeV/c^2, where M_{vertex} and M_{K_s} are the masses of the secondary vertex and K_s respectively. This requirement is in addition to the requirments imposed for K_s and Λ removal.

Candidate secondary vertices passing the above mentioned criteria with a positive (negative) L_{xy} are referred to as positive (negative) tags.

Appendix B

Effect of track finding degradation

The effect of track degradation is two-fold. First, the number of taggable jets in an event is reduced and second, the tagging rate per taggable jet is also reduced. Due to a reduction in the number of tracks, fewer jets pass the $N^0_{trk} \geq 2$ requirement of being taggable. This also results in a reduction in the number of tracks that pass the Pass 1 and Pass 2 requirements of the b-tagging algorithm, leading to a lower tagging rate per taggable jet.

B.1 Effect on the number of taggable jets

To investigate the first effect, the number of taggable jets for each jet multiplicity is compared before and after the degradation procedure for different b tag requirements. An event with k jets can have upto k taggable jets in it. A change in the number of taggable jets can be seen by taking the ratio of the distributions of the number of taggable jets after and before the track degradation for each jet multiplicity. If there is no change in the number of taggable jets, then the ratios should be 1. The ratios are shown in figure B-2 as a function of the number of taggable jets in an event for different jet multiplicities and b-tagging requirements. The ratios are < 1 in k and $k-1$ taggable jets bins, and >1 for the lower taggable jet multiplicity bins. A depletion of k-jet events with k or $k-1$ taggable jets, and an increase in the number of events with $k-2$ or fewer taggable jets clearly indicates a reduction in the

number of taggable jets per event. It is also seen that for events with 2 b tags, the number of taggable jets after track degradation is $\sim 70\%$ of the number before track degradation. The effect is larger for events with ≥ 3 b tags. Since every event with 3 b tags has 3 double tagged combinations, the reduction in the number of double tagged combinations due to track degradation is greater than 30%.

B.2 Effect on the tagging rates

The second effect is investigated by comparing tagging rates per taggable jet before and after track degradation. Figure B-3 shows the rates for events with 1 and 2 b tags. It is seen that the tagging rates per taggable jets are reduced by $\sim 10\%$.

The cumulative effect of the reduction in the number of taggable jets and the decrease in the tagging rates per taggable jet is that the number of double tagged combinations after degradation is $70\% \times 90\% \sim 60\%$ of the number before the degradation.

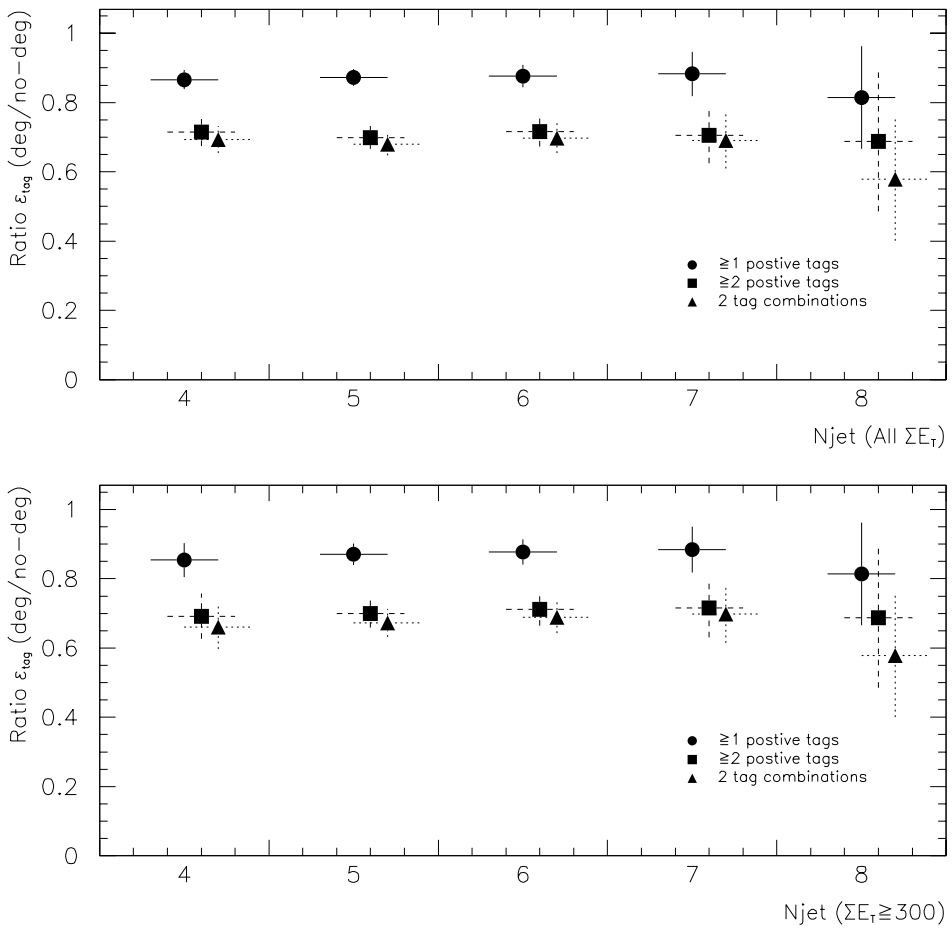

Figure B-1: *The ratio of the number of tagged events and combinations observed in the $t\bar{t}$ Monte Carlo after and before track degradation. The upper plot shows the ratio for different jet multiplicities before the ΣE_T requirement. The lower plot shows the ratio after the ΣE_T requirement.*

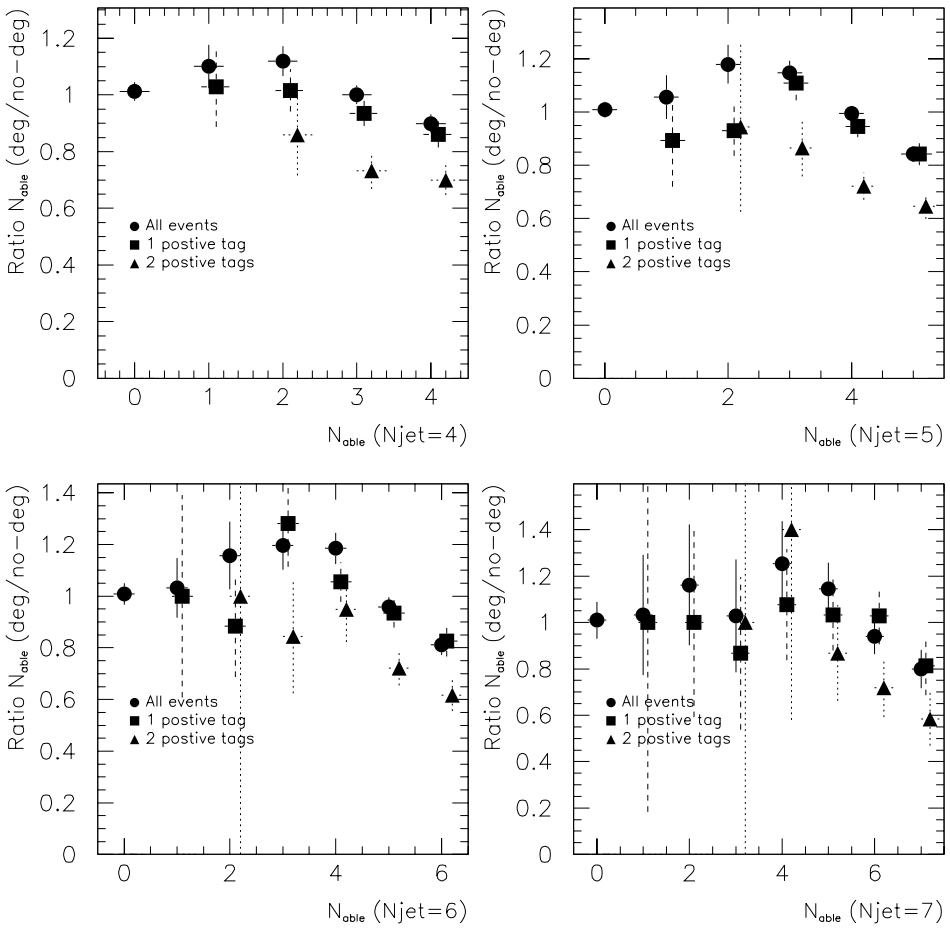

Figure B-2: *The ratio of the number of taggable jets observed in the $t\bar{t}$ Monte Carlo after and before track degradation.*

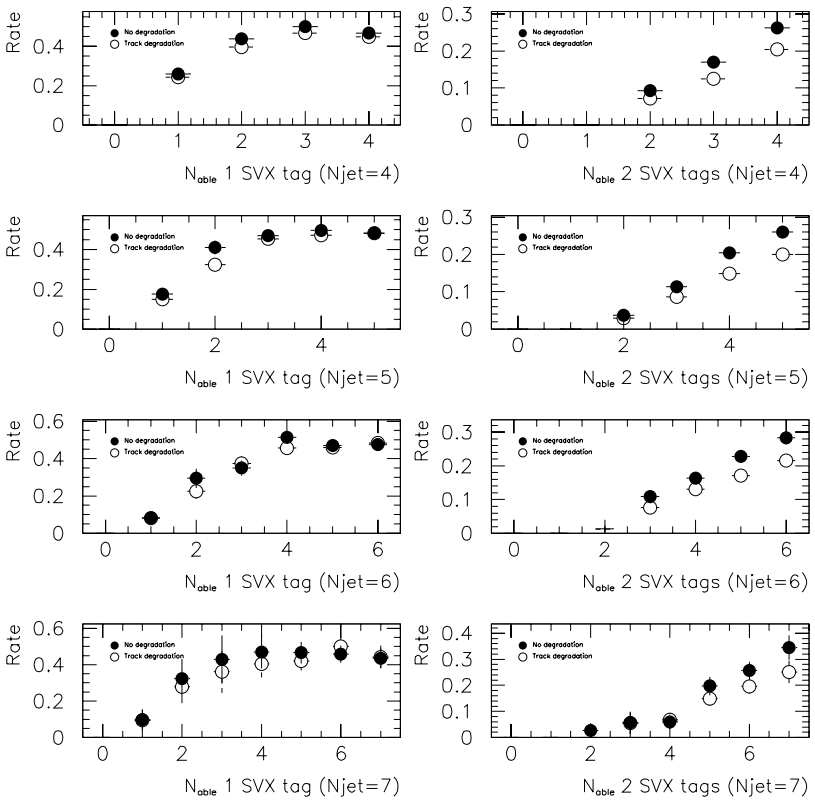

Figure B-3: *Tagging rate per taggable jet in the $t\bar{t}$ Monte Carlo after and before track degradation, for different jet multiplicities. The tagging rates are compared for events with one and two tagged jets.*

Bibliography

[1] S. Glashow, Nucl. Phys. **22**, 579 (1961).
S. Weinberg, Phys. Rev. Lett. **19**, 1264 (1967).
A. Salam, *Elementarty Particle Theory*, ed. N. Svartholm (Almquist and Wiksells, Stockholm, 1969), p. 367.

[2] T. Muta, **Foundations of Perturbative QCD** (World Scientific, Singapore, 1987);
G. Sterman, *Introduction to Perturbative QCD* 1991 TASI lectures, Stony Brook preprint ITP-SB 91-55;
H. Fritzsch, M. Gell-Mann and H. Leutwyler, Phys. Lett. **B47**, 365 (1973);
D. J. Gross and F. Wilczek, Phys. Rev. **D8**, 3633 (1973);
S. Weinberg, Phys. Rev. Lett. **31**, 494 (1973);
F. J. Yndurain, **Quantum Chromodynamics: An Introduction to the Theory of Quarks and Gluons** (Springer, New York, 1083);
L. D. Fadeev and A. A. Slavnov, **Gauge Fields: An Introduction to Quantum Theory**

[3] F. Abe et al., Phys. Rev. Lett. **74**, 2626 (1995)

[4] S. Abachi et al., Phys. Rev. Lett. **74**, 2632 (1995)

[5] I. J. R. Aitchison, A. J. G. Hey, **Gauge Theories in Particle Physics**, (Hilger, Bristol 1982);
F. Halzen, A. D. Martin, **Quarks and Leptons**, (Wiley, New York 1984);

C. Itzykson and J. Zuber, **Quantum Field Theory**, (McGraw-Hill, 1980);
V. D. Barger and R. J. N. Phillips, **Collider Physics**, (Addison-Wesley, 1987)

[6] Particle Data Group, Phys. Rev. **D54**, 1 (1996).

[7] S. Weinberg, **Gravitation and Cosmology**, (Wiley, 1972).

[8] J. H. Christenson et al., Phys. Rev. Lett. **13**, 138 (1964).

[9] E. D. Bloom et al., Phys. Rev. Lett. **23**, 930 (1969);
M. Breidenbach et al., Phys. Rev. Lett. **23**, 935 (1969);
A. Bodek et al., Phys. Rev. **D20**, 1471 (1979)

[10] A. X. El-Khadra, presented at 1993 Lattice Conference, OHSTPY-HEP-T-93-020.

[11] M. L. Perl et al., Phys. Rev. Lett. **35**, 1489 (1975)

[12] S. W. Herb et al., Phys. Rev. Lett. **39**, 252 (1977)

[13] Ch. Berger et al., Phys. Lett. **B76**, 243 (1978);
J. K. Bienlein et al., Phys. Lett. **B78**, 360 (1978);
C. W. Darden et al., Phys. Lett. **B76**, 246 (1978)

[14] R. N. Cahn, G. Goldhaber, **Experimental Foundations of Particle Physics** (Cambridge, 1989)

[15] M. Kobayashi and M. Maskawa, Prog. Theor. Phys., **49**, 652 (1973)

[16] G. L. Kane and M. E. Peskin, Nucl. Phys. **B195**, 29 (1982)

[17] S. L. Glashow, J. Illiopoulos and L. Maiani, Phys. Rev. **D2**, 1285 (1970)

[18] C. Matteuzzi et al., Phys. Lett. **B129**, 141 (1983)

[19] F. Abe et al., Proceedings of the 17^{th} International Symposium on Lepton Photon Interactions (LP95), Beijing, China, 1995.

[20] C. Campagnari and M. Franklin, *The discovery of the top quark*, To be published in Reviews of Modern Physics;
P. K. Sinervo, Talk given at 1995 Lake Louise Winter Institute on Quarks and Colliders, Lake Louise, Canada, 19-25 Feb 1995. In *Lake Louise 1995, Quarks and colliders* p.316-351

[21] L. Ibanez and C. Lopez, Phys. Rev. Lett. **126**, 54 (1983);
J. Ellis et al., Phys. Lett. **B125**, 275 (1983);
L. Alvarez-Gaume et al., Nucl. Phys. **B221**, 495 (1983)

[22] E. Laenen et al., Phys. Lett. **B321**, 254 (1994)

[23] E. Berger and H. Contopanagos, Phys. Rev. **D54**, 3085 (1996)

[24] S. Catani et al., CERN-TH/96-86,hep-ph/9604351

[25] T. Stelzer and S. Willenbrock, Phys. Rev. **B357**, 125 (1995);
M. Smith and S. Willenbrock, hep-ph/9604223;
D. O. Carlson and C. P. Yuan, *Probing new physics from the single top production*, hep-ph/9509208.

[26] L. Orr, Phys. Rev. **D44**, 88 (1991)

[27] J. Benlloch et al., Phys. Rev. **D48**, 5226 (1993)

[28] F. Abe et al., *To be submitted to PRL*

[29] F. Abe et al., *To be submitted to PRL*

[30] M. Kruse, Ph.D. Thesis, Purdue University, 1996.

[31] D. Kestenbaum, Ph.D. Thesis, Harvard University, 1996.

[32] D. Glenzinski, Ph.D. Thesis, Johns Hopkins University, 1995.

[33] P. Bhat, *New results on the top quark from DØ*, Talk given at Fermilab, Joint Theoretical and Experimental Physics Seminar, Feb. 21, 1997.

[34] F. Abe et al., *Submitted to PRL*, Fermilab pre-print Pub-97/075-E.

[35] P. Azzi, Ph.D. Thesis, University of Padova, 1996

[36] F. Paige and S. D. Protopopescu, Brookhaven National Laboratory Preprint BNL-38034, 1986.

[37] G. Marchesini and B. R. Webber, Nucl. Phys. **B238**, 1 (1984);
G. Marchesini and B. R. Webber, Nucl. Phys. **B310**, 461 (1988)

[38] T. Sjöstrand and M. Bengtsson, Comp. Phys. Comm. **43**, 367, 1987.

[39] Frixione et al., Phys. Lett. **B351**, 555 (1995);
N. Kidionakis and J. Smith, Phys. Rev. **D51**, 6092 (1995)

[40] F. Abe et al., Nucl. Inst. and Meth. Phys. Res., **271A**,387 (1988);
Fermilab-Pub-94/024-E, submitted to Nucl. Instrum. Methods Phys. Res.

[41] S. van der Meer, *Stochastic Damping of Betatron Oscillations in the ISR*, CERN/ISR-PO/72-31 (1994);
F. Sacherer, *Stochastic Cooling Theory*, CERN-ISR-TH/78-11 (1981).

[42] D. Amidei et al., Nucl. Inst. and Meth. Phys. Res., **350**,73 (1994)
P. Azzi et al., Nucl. Inst. and Meth. Phys. Res., **360**,137 (1995)

[43] F. Abe et al., Phys. Rev. **D45**, 1448 (1992)

[44] F. Abe et al., Phys. Rev. **D44**, 601 (1991)
F. Abe et al., Phys. Rev. Lett. **70**, 713 (1993)

[45] M. Shapiro et al., A user's guide to QFL, **CDF** Internal Note CDF/ANAL/MONTECARLO/PUBLIC/1810 (1992);
A. Caner, *CDFSIM + QFL Simulation of the CDF Detector*, **CDF** Internal Note CDF/ANAL/MONTECARLO/PUBLIC/2177 (1993)

[46] W. Badgett et al., *Level 2 Trigger simulation for the 1992-1993 run.*, **CDF** Internal Note CDF/DOC/TRIGGER/PUBLIC/2017 (1993)

[47] C. Campagnari, *Normalization of Run 1B μ+jets Data*, **CDF** Internal Note CDF/ANAL/TOP/CDFR/2821 (1994);
J. F. Troconiz and J. A. Valls, *Search for Invariant Mass Resonances in the Multijet Data Sample*, **CDF** Internal Note CDF/PHYS/EXOTIC/PUBLIC/3711 (1996)

[48] F. Abe et al., Phys. Rev. **D45**, 1448 (1992) F. Abe et al., Phys. Rev. **D46**, 4857 (1992)

[49] R. Field and R. Feynmann, Nucl. Phys. **B136**, 1 (1978)

[50] F. Abe et al., Phys. Rev. Lett. **71**, 2296 (1993)

[51] F. Abe et al., Phys. Rev. **D50**, 2966 (1994);
F. Abe et al., Phys. Rev. Lett. **73**, 225 (1994)

[52] C. Miao and W. Yao, *SECVTX tagging study with track-finding degradation*, **CDF** Internal Note CDF/ANAL/TRACKING/CDFR/3542 (1996)

[53] J. Lewis and P. Avery, *CLEOMC: The CDF Interface to the CLEO Monte Carlo (QQ)*, **CDF** Internal Note CDF/DOC/MONTECARLO/PUBLIC/2724 (1994)

[54] F. A. Berends et al., Nucl. Phys. **B357**, 32 (1991)

[55] F. Abe et al., Phys. Rev. Lett. **77**, 453 (1996)

[56] P. Azzi et al., *Evaluation of the W/Z+jets background for the top search in the all-hadronic decay mode*, **CDF** Internal Note CDF/DOC/TOP/CDFR/3428 (1995)

[57] F. Abe et al., Phys. Rev. Lett. **70**, 4042 (1993)

[58] J. Ohnemus et al., Phys. Rev. **D43** (1991), 3626;
J. Ohnemus, Phys. Rev. **D44** (1991), 1403;
J. Ohnemus, Phys. Rev. **D44** (1991), 3477

[59] MINUIT, CERN Program Library Long Writeup D506, version 92.1 (1992)

[60] G. D'Agostini, *Probability and Measurement Uncertainty in Physics, a Bayesian Primer*, DESY 95-242, (1995).

[61] The CDF II collaboration, *The CDF II detector, Technical Design Report*, (1996).